7-14-2020

Pressure Monitoring for Subsurface Leakage Characterization

Mojtaba Mosaheb
Louisiana State University at Baton Rouge

PRESSURE MONITORING FOR SUBSURFACE LEAKAGE CHARACTERIZATION

A Dissertation

Submitted to the Graduate Faculty of the
Louisiana State University and
Agricultural and Mechanical College
in partial fulfillment of the
requirements for the degree of
Doctor of Philosophy

in

The Craft and Hawkins Department of Petroleum Engineering

by
Mojtaba Mosaheb
B.S., Sharif University of Technology, 2012
M.S., Azad University, 2014
December 2020

ACKNOWLEDGMENTS

This work would not have been possible without the financial support of Craft and Hawkins Department of Petroleum Engineering, US Department of Energy, and Louisiana Board of Regents. First and foremost, I would like to express the deepest appreciation to my committee chair, Dr. Mehdi Zeidouni who has taught me more than I could ever give credit for here.

I am grateful to all of my dissertation committee members, Dr. Richard Hughes, Juan Lorenzo Karsten Thompson, Paulo Waltrich, and Clinton Willson for providing me extensive personal and professional guidance and taught me a great deal about both scientific research and life in general.

I want to thank all of my colleagues Yilin Mao, Refaat Hashish, Dayna Rodriguez, Oscar Molina, Nam Tran, and Kewei Shi. Finally, my appreciation goes to my parents for their unconditional love and support.

TABLE OF CONTENTS

ACKNOWLEDGMENTS ii

LIST OF FIGURES …. v

ABSTRACT ……..... viii

CHAPTER 1. INTRODUCTION 1

CHAPTER 2. LEAKY WELL 6
2.1. Introduction 6
2.2. Methodology 7
2.3. Focused well leakage 8
2.4. Identification of diffuse caprock leakage 13
2.5. Identification of fault leakage 14
2.6. Well leakage example problem 16
2.7. Increasing the radius of investigation in pressure testing 25
2.8. Summary 37

CHAPTER 3. LEAKY FAULT 39
3.1. Introduction 39
3.2. Fault leakage to a high permeability zone 42
3.3. Anisotropic fault leakage 58
3.4. Fault leakage extension to multiple shallower formations 78
3.5. Summary 92

CHAPTER 4. LEAKY CAPROCK 94
4.1. Introduction 94
4.2. Methodology 96
4.3. Mathematical modeling 97
4.4. Results and discussion 101
4.5. Optimal duty cycle to maximize value of information in periodic test 107
4.6. Summary 109

CHAPTER 5. CONCLUSIONS AND RECOMMENDATIONS 111
5.1. Conclusions 111
5.2. Recommendations 113

APPENDIX 1. GEOMETRICAL CALCULATIONS OF LOCATING THE LEAKY WELL 117

APPENDIX 2. MATHEMATICAL SOLUTION OF FAULT LEAKAGE TO THE HIGH-PERMEABILITY ZONE 119

APPENDIX 3. ANALYTICAL SOLUTION OF ANISOTROPIC FAULT LEAKAGE 123

REFERENCES …… 127

VITA …… 136

LIST OF FIGURES

2.1. Schematic representation of the two-layer system with leaky well. 8

2.2. Schematic representation of the wells in a horizontal plane 12

2.3. Geometry of leakage pathways in the two-layer system 14

2.4. Schematic representation of fault leakage 15

2.5. Pressure changes of the observation wells, and the corresponding MPR and MPR derivative in log-log scale 17

2.6. Semi-log plot of MPR ……..……..…….. 18

2.7. Leakage rate through the leaky well 19

2.8. Estimated location of the leaky well (red solid circle) compared to the actual location (blue solid circle) 20

2.9. Pressure response of AZ at r=2.25 m normalized by the leakage rate. 22

2.10. MPR derivative of leaky caprock system. 23

2.11. MPR and the corresponding derivative for leaky fault system. 24

2.12. Effect of fault horizontal conductivity through the fault plane (α_y) on the MPR of the two observation points in the AZ. 25

2.13. Rate normalized pressure and derivative for constant bottom-hole pressure 30

2.14. Rate normalized pressure and derivative for linear bottom-hole pressure 30

2.15. Rate normalized pressure and derivative for logarithmic bottom-hole pressure 31

2.16. Rate normalized pressure and derivative for sinusoidal bottom-hole pressure (ω=1) 32

2.17. Rate normalized pressure and derivative for sinusoidal bottom-hole pressure (ω=2) 32

2.18. Rate normalized pressure and derivative for sinusoidal bottom-hole pressure (ω=0.5) 33

2.19. Rate normalized derivative for quadratic bottom-hole pressure (b=c=1) 34

2.20. Quadratic bottom-hole pressure change 35

2.21. Rate normalized pressure derivative for quadratic bottom-hole pressure (b=c=0.0001) 35

2.22. Rate normalized pressure derivative for 3rd order polynomiaol bottom-hole pressure (b=c=0.0001) 36

2.23. Bottom-hole pressure and well flow rate for the example problem 37

2.24. RNP for example problem 37

3.1. Schematic representation of the physical model 43

3.2. Validation of the spatial pressure distribution in the injection zone after 10 days 47

3.3. Validation of temporal variation of well pressure and (logarithmic) pressure derivative with respect to time using numerical simulation 48

3.4. Type curves of the leaky fault system considering T_D =1 and η_D =1 50

3.5. Effect of T_D and η_D on the type curves 51

3.6. Characterization procedure of the leaky fault system 53

3.7. Pressure and pressure derivative for example 1 54

3.8. Pressure and derivative response for a sealing fault, considering $\alpha = \alpha_u = 0$. 55

3.9. Estimating α and α_u with the base type curves for example 1 55

3.10. Pressure and derivative data for example 2 57

3.11. Estimation of α and α_u with the base type curves for example 2 57

3.12. (a) Schematic representation of the physical model, (b) Directions of intra-fault and fault-reservoirs hydraulic connections on x-z coordinate 60

3.13. Comparison of the analytical (dots) versus numerical (dotted lines) pressure distribution in the injection zone at different times. 66

3.14. Injection-zone pressure derivative validation. 67

3.15. Effect of α_x on pressure derivative 68

3.16. Effect of α_y on pressure derivative 69

3.17. Effect of α_z on pressure derivative 70

3.18. Type curves for anisotropic fault characterization applying pressure derivative of the injection well 71

3.19. Type curves for faults that are sealing upward and across the fault 72

3.20. Type curves for Partially-sealing faults 73

3.21. Type curves for Leaky faults 74

3.22. (a) Effect of dimensionless fault width, leakage interval ratio, thickness ratios, and on pressure derivative of the active well 76

3.23. Effect of up-fault conductivity on the leakage rate 77

3.24. Type curve matching for leaky fault characterization. 78

3.25. Schematic of fault leakage in the multilayer system 79

3.26. Pressure derivative of the injection well for different number of layers 88

3.27. Pressure response of the shallower formations in a five-layer system 90

3.28. Pressure drawdown of the production well 91

3.29. Pressure derivative of the production well 92

4.1. Schematic representation of the physical model 96

4.2. (a) Injection rate and above zone pressure response (b) Above-zone pressure Amplitude for analytical solution against numerical simulation 103

4.3. Above zone pressure response for example problem 104

4.4. Estimation of caprock diffusivity using the amplitude of above zone pressure response ... 105

4.5. Effect of 50% error in the above zone diffusivity ratio on estimating the caprock diffusivity ratio 106

4.6. Effect of 50% error in z_w on estimating the caprock diffusivity ratio 106

ABSTRACT

Undesirable leakage from underground sedimentary formations is a matter of considerable concern due to implications for water resources contamination and greenhouse gas emissions. Leakage in underground formations can remain undetected for a long period. Pressure monitoring is a dynamic method that can be used for leakage detection and characterization. The pressure signals are affected by the hydraulic characteristics of the reservoir media and leakage pathways. Consequently, the pressure data can be interpreted to obtain information about the hydraulic characteristics of the system. Pressure interpretation is useful for early leakage detection, because the pressure signals travel fast in reservoir media. In this study, analytical methods are developed to investigate pressure variations in the systems of leaky well, leaky fault, and leaky caprock. Leakage characterization methods are presented based on the pressure interpretation.

CHAPTER 1. INTRODUCTION

Undesirable leakage from underground sedimentary formations is a matter of considerable concern due to implications for water resources contamination and greenhouse gas emissions (Benson & Orr, 2008; Birkholzer, Zhou, & Tsang, 2009a; Blackford et al., 2009; IPCC, 2005; Keating et al., 2013; Lu, Partin, Hovorka, & Wong, 2010; Pacala, 2003; Siirila, Navarre-Sitchler, Maxwell, & McCray, 2012). Leakage in underground formations can remain undetected for a long period. This work aims to provide an identification method for early detection of leakage from injection zone to overlying formations.

Deep saline aquifers are used for underground disposal/storage of fluids. Leakage of the injected fluids from the injection formation may adversely affect underground environment, especially underground fresh water resources. The contamination can be a consequence of native fluid leakage as well as injected fluids (Damen, Faaij, & Turkenburg, 2006; Little & Jackson, 2010). For instance, leakage of brine during CO_2 injection into saline aquifers can affect the shallow resources of fresh water. CO_2 can contaminate fresh water resources and may impact pH of the native fluids (e.g. brine) and can result in dissolution and movement of minerals (de Orte, Sarmiento, Basallote, Rodríguez-Romero, & Riba, 2014; Harvey et al., 2012).

The existence of the naturally occurring potential leaky structures may not be a major problem during the natural accumulation of fluid in the reservoirs. However, the overpressure caused by injection operations would enhance the leakage risk (Rutqvist, Birkholzer, Cappa, & Tsang, 2007). Moreover, injection pressurization may be associated with induced seismicity that can be felt by the general population, and may cause damages (Ellsworth, 2013; Keranen, Savage, Abers, & Cochran, 2013). Induced seismicity can also damage the sealing capacity of existing

potential leakage pathways including wells, faults, and caprock (Cappa & Rutqvist, 2011; Wiprut & Zoback, 2000).

Plugged and Abandoned (P&A) wells are examples of leakage pathways that may be conduit for fluid migration from confined permeable formations (Ebigbo, Class, & Helmig, 2007; Jordan & Carey, 2016; Watson & Bachu, 2009). Abandoned wells should be plugged according to standard regulations to prevent undesirable hydrodynamic connection between the sequential layers intersected by the well. Cementing materials used during the P&A process normally have very low permeability. However, the permeability can be changed by cement degradation over a long time. Further, the interfaces of cement, rock matrix and casing can be the weak points of leakage for a plugged well (Bachu & Bennion, 2009; Wojtanowicz, 2016). CO_2 can make decomposition reaction with cement after flowing inside the cement matrix (Scherer & Huet, 2009). In addition, the low pH brine caused by CO_2 dissolution can corrode the sealing cement of abandoned wells. The acidified brine may affect the cement especially if the acid remains in contact with cement for several years (Scherer et al., 2015; Toews, Shroll, Wai, & Smart, 1995). Completion failure of the injection well can also be a reason for well leakage.

Leaky caprocks and leaky faults are two other possible leakage pathways that can cause significant hydraulic connection between confined sedimentary formations (Annunziatellis et al., 2008; Barton, Zoback, & Moos, 1995; Chen et al., 2013; Evans, Forster, & Goddard, 1997; Hermanrud & Bols, 2002; Leith, Kaarstad, Connan, Pierron, & Caillet, 1993; R. Sibson, 1977). A fault is a planar interface that can be permeable across and along the fault plane with different permeabilities in different directions. A fault generally consists of a low permeability core surrounded by high permeability damaged zones. The permeability of the damaged zone is controlled by the fractures induced during fault displacement (Agosta, Prasad, & Aydin, 2007;

Billi, Salvini, & Storti, 2003; Bruhn, Parry, Yonkee, & Thompson, 1994; Caine, Evans, & Forster, 1996; Caine & Forster, 1999; Chester, Evans, & Biegel, 1993; Rawling, Goodwin, & Wilson, 2001). In addition to leaky fault and well, leakage can occur through a permeable region in a seal/low-permeability caprock layer. The induced stress caused by overpressure can damage the caprock seal especially during the injection (Hermanrud & Bols, 2002; Ingram & Urai, 1999; Selvadurai, 2012; R. H. Sibson, 2003).

As the speed of the pressure propagation is much higher than the leaky fluids, pressure monitoring has been considered as an early-detection method for undesirable leakage in underground storage (Sun & Nicot, 2012; Wiese, Zimmer, Nowak, Pellizzari, & Pilz, 2013). For leaky fault systems, Rahman, Miller, and Mattar (2003) presented an analytical solution for the fault leakage in a single layer reservoir considering distinct horizontal flow along the fault plane as well as cross-fault flow. Shan, Javandel, and Witherspoon (1995) introduced an analytical model to account for vertical leakage through a fault to an upper permeable zone. However, they ignored the pressure discontinuity across the fault. Zeidouni (2012) presented analytical solutions of two-layer and multi-layer systems, which demonstrated the pressure discontinuity across the fault during the vertical leakage. Zeidouni (2016) fully accounted for the lateral resistance of the fault in all layers of the multi-layer system. Several other studies have investigated the pressure variations of the fault leakage systems (Anderson, 2006; Chabora & Benson, 2009; Jha & Juanes, 2014; Matthäi, Aydin, Pollard, & Stephen, 1998; Ochoa-González, Carreón-Freyre, Cerca, & López-Martínez, 2015).

In this study, we propose pressure interpretation methods for early detection of leakage from the injection zone to adjacent formations. In these methods, we identify specific types of leaky pathway by interpreting the pressure signals and estimate the leakage rate and location and

characteristics of those specific leaky pathways. Our approach to design characterization methods is analytical modeling of the corresponding physical models. Analytical modeling has advantages over the numerical approach. Numerical approaches are computationally more expensive than analytical methods. In addition, all the values of system properties are required for a single run of numerical simulation while the analytical solutions can investigate the systems with unknown parameter, especially with dimensionless groups. Therefore, the analytical approaches are useful for inverse modeling to estimate the unknown characteristics of the reservoir during the characterization methods.

The estimated characteristics can be useful to do the reservoir studies and management considering the leakage, and evaluate the effect of leakage on the operations regarding the storage aquifers. It can also be useful to assess the environmental effects of leakage to adjacent formations and control the consequent contaminations to water resources and atmosphere and make decisions to reduce these damages.

In chapter two, we propose analytical approach for spatial and temporal characterization of well leakage and its identification from leaky fault and leaky caprock. The characterization method is based on the above-zone pressure interpretation to distinguish the specific flow regimes. Leaky well is identified according to the late-time pressure response while fault and caprock leakage are identified by the early-time response. Since the early-time responses may not be detected from a far distance, the concept of radius of investigation is important for the early-time responses. The late-time response may not be useful to distinguish leaky well from fault leakage. We propose a method to decrease the arrival time of the pressure response from a linear source.

In chapter three, we develop three analytical approaches for fault leakage characterization based on the injection zone pressure interpretation. In the first model, the fault conducts fluids to

a high permeability zone. In the second model, we consider the anisotropic permeability in the fault zone and the above-zone resistance to flow. In the third model, we evaluate the vertical extension of fault leakage to multilayer system of shallower formation.

In chapter four, we propose periodic pressure method to evaluate inter-reservoir flow through a weakness in the sealing layer. Since the periodic tests maintain the early-time behavior during the test, the periodic pressure responses are useful for caprock characterization. Next, we propose a method to enhance the value of information in a periodic test.

CHAPTER 2. LEAKY WELL

Above-zone (AZ) pressure has been recently investigated for inferring leakage pathway characteristics in leakage events from subsurface injection operations. The recorded pressure in the AZ should be purely related to leakage and therefore it can be safely inverted to deduce leakage characteristics. It is crucial to evaluate fluid leakage through abandoned wells to plan for further measurements of leakage prevention. However, the recorded AZ leakage signal may not be related to leaky well(s). Therefore, identification and spatial investigation of well leakage is required for leakage evaluation. In this chapter, we propose a pressure interpretation method for early detection of leaky pathways, applying two observation points in the AZ. We distinguish leaky well, fault and caprock based on their corresponding flow regime identification. We show that the pressure difference of the two observation wells can be applied as a proxy for unknown leakage rate, which is crucial for leakage identification as well as characterization.

2.1. Introduction

Several analytical models were introduced to quantify leakage through different types of pathways. Javandel, Tsang, Witherspoon, and Morganwalp (1988) developed an analytical solution to model pressure response to a leaky well in a multi-layer system. They considered an observation well in the injection layer and assumed pressure of the upper layer is constant throughout. Avci (1994) developed an analytical solution for well leakage to an upper layer considering the upper layer's resistance to flow. Cihan, Zhou, and Birkholzer (2011) developed a multilayer analytical solution for leaky wells. Zeidouni and Vilarrasa (2016) introduced a real time solution for pressure perturbation due to a leaky well in a two-layer system separated by a confining layer. They proposed a method to locate the leaky well by considering three observation wells in the AZ. Zeidouni (2014) presented an analytical solution for well leakage in a laterally

bounded multilayer system. Analytical models were also developed to examine the other leaky pathways. Leakage through a low-permeability caprock is modeled as diffuse leakage (Cheng & Morohunfola, 1993; Cihan et al., 2011). Leaky faults are modeled as planar discontinuities in the reservoir (Anderson, 2006; Shan et al., 1995; Zeidouni, 2012, 2016).

A primary step for leakage characterization is identification of the major leakage pathways and evaluation of their leakage potential. In this chapter, we first present a characterization procedure for leaky well system based on the AZ pressure. Location and leakage coefficient of the leaky well and the leakage rate are estimated considering two observation wells in the AZ. Next, we extend the leakage identification to distinguish the leaky caprock, leaky fault and leaky well according to the pressure response. The identification method is based on the diagnostic plots of the specific flow regimes. The identification and characterization procedures are applied to example problems for demonstration.

2.2. Methodology

Fig. 2.1 shows schematic of the leaky well physical model. The two-layer system is the same for the leaky fault and leaky caprock. In leaky fault system, the leaky well is replaced with the leaky fault. For the leaky caprock, there is a permeable region in the caprock layer instead of leaky well (Fig. 2.1). The leaky pathway connects the AZ to the injection zone while these zones are otherwise separated by the confining layer (caprock). In this study, the leakage problem is thought of as injection into the single-layer AZ through the leaky pathway. In order to identify the leakage by this approach, we need to apply deconvolution on the AZ pressure because the leakage rate is time variable. The main challenge is that the leakage rate is unknown and needs to be determined. Therefore, we need to know how we can apply deconvolution on the AZ pressure data with respect to the leakage rate, while the leakage rate is unknown. We introduce a proxy for

leakage rate, which can be applied instead of leakage rate for pressure deconvolution. Applying the deconvolution method, we propose a pressure interpretation method for leakage characterization and estimation of time variable leakage rate.

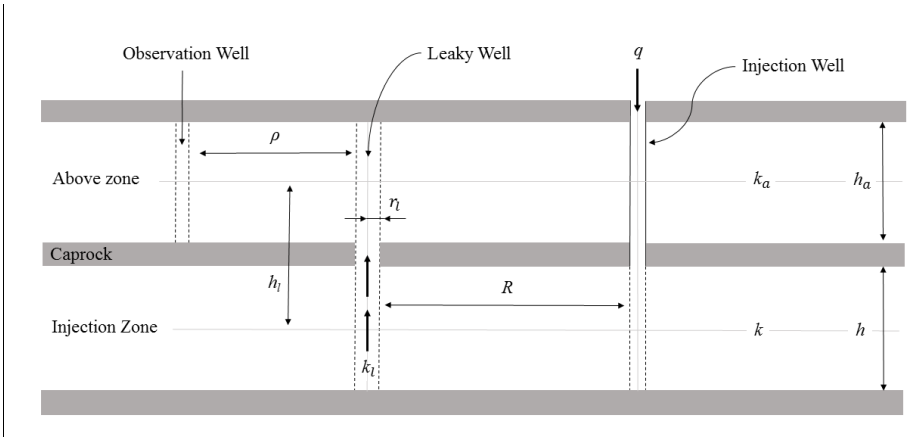

Fig. 2.1. Schematic representation of the two-layer system with leaky well.

This schematic applies for fault leakage system with the replacement of the leaky well with leaky fault. For leaky caprock system, the leaky well is removed and a weakness in the caprock should be considered.

2.3. Focused well leakage

In this section, we present a characterization method for the leaky well system. We consider the caprock as sealing and the only possible leakage pathway is the leaky well. The injection well is fully perforated in the injection zone and the injected fluid is considered identical to the initial fluid in the two layers. μ and B are viscosity and formation volume factor of the fluid and q is the injection rate. The observation well is located in the AZ at distance ρ from the leaky well. Permeability of the leaky well and radii of the injection well and leaky well are denoted by k_l, r_w, and r_l, respectively. h_l is leakage interval and R is the distance between the injection and leaky wells. k, k_a, h, and h_a are permeability and thickness of the injection and above zones. Subscript a denotes the AZ. Permeability is constant, homogeneous, and isotropic for each layer. Porosity (ϕ)

and compressibility (c_t) of the two layers are identical, constant, and homogeneous. Both layers are considered infinite acting in horizontal directions. The initial pressure is uniform in the both injection and above zones. Zeidouni and Vilarrasa (2016) presented a real time analytical solution for the leaky well system (Equation 2.1).

$$\Delta p_a(t,\rho) = \frac{q\mu B}{4\pi(kh + k_a h_a)}\left(-\gamma - \ln\left(\frac{R^2}{4\eta t}\right)\right) - \frac{q_l(t)\mu B}{4\pi k_a h_a}\left(\kappa + \ln\left(\frac{\eta\rho^2}{{r_w}^2\eta_a}\right)\right) \tag{2.1}$$

where:

$$\kappa = \frac{2k_a h_a}{\alpha(kh + k_a h_a)} + \ln\left(\left(\frac{r_w}{r_l}\right)^2\left(\frac{\eta_a}{\eta}\right)^{\left(\frac{k_a h_a}{kh + k_a h_a}\right)}\right) \tag{2.2}$$

Δp_a is pressure change of the AZ, $q_l(t)$ is leakage rate as a function of time, α is leakage coefficient of the leaky well, and κ is a constant that can represent the conductivity of the leaky well. η and η_a are the diffusivity coefficient of the injection and above zones.

$$\alpha = \frac{{r_l}^2 k_l}{2khh_l} \qquad \eta = \frac{k}{\mu\phi c_t} \qquad \eta_a = \frac{k_a}{\mu\phi_a c_{ta}} \tag{2.3}$$

The pressure difference of two arbitrary points in the AZ (Δp_{a1} and Δp_{a2}) based on this analytical solution is given by:

$$\Delta p_{a1}(t,\rho_1) - \Delta p_{a2}(t,\rho_2) = \frac{\mu B}{2\pi k_a h_a}\ln\left(\frac{\rho_2}{\rho_1}\right) q_l(t) \tag{2.4}$$

where ρ_1 and ρ_2 are the distances between the leaky well and that arbitrary points. Equation (2.4) shows that the pressure difference of the two arbitrary points in the AZ (ΔP_{a1} - ΔP_{a2}) is proportional to leakage rate at any given time (Equation 2.5).

$$\left(\Delta p_{a1}(t,\rho_1) - \Delta p_{a2}(t,\rho_2)\right) \propto q_l(t) \tag{2.5}$$

Winestock and Colpitts (1965) proposed a simple deconvolution method for radial transient flow while the flow rate variations are smooth. In their method, the pressure is normalized by the

time variable rate. We applied this deconvolution method to derive the pressure changes of the AZ normalized by the leakage rate. Equation (6) is the line source solution for the above zone pressure applying the Winestock and Colpitts (1965) pressure normalization method. The leaky well is considered as a line source in the above zone. The above zone pressure is normalized with respect to the leakage rate in Equation (2.6).

$$\frac{\Delta p_{aj}(t)}{q_l} = \frac{\mu B}{4\pi k_a h_a}\left(\ln\left(\frac{4\eta_a t}{\rho_j^{\,2}}\right) - \gamma\right) \tag{2.6}$$

where *j* denotes the observation points 1 or 2. γ is Euler constant that is equal to 0.5772. Comparing Equations (2.5) and (2.6), we conclude that the pressure difference (ΔP_{a1} -ΔP_{a2}) can be applied as a proxy of unknown leakage rate in the deconvolution method to interpret the AZ pressure. We can normalize the AZ pressure with respect to the difference of pressures measured at two observation wells in the AZ. Combining Equations (2.4) and (2.6), we obtain Equation (2.7):

$$\Delta P_{a1}(t)\Big/\left(\Delta P_{a1}(t) - \Delta P_{a2}(t)\right) = \left(\ln(t) - \ln\left(\frac{e^{\gamma}\rho_1^{\,2}}{4\eta_a}\right)\right)\Bigg/\left(2\ln\left(\frac{\rho_2}{\rho_1}\right)\right) \tag{2.7}$$

We refer to the left hand side of Equation (2.7) as the modified pressure ratio (*MPR*). The unknown leakage rate does not appear in Equation (2.7). The pressure variations of a single point in the AZ cannot be used to identify the radial flow regime, because the leakage rate is time variable. However, *MPR* represents deconvolved pressure and therefore can be applied for flow regime identification. In leaky well system, radial flow caused by well leakage in the AZ can be identified by zero-slope line on logarithmic derivative of *MPR* versus time on log-log plot. After identification of the well leakage, we work on the characterization method. Equation (7) illustrates that the semi-log plot of *MPR* versus time is a straight-line (Equation 2.8).

$$MPR = m\ln(t) + b \tag{2.8}$$

where *m* and *b* are slope and intercept of the straight line. Therefore, we can use the observation wells' pressure data to find ρ_1 and ρ_2 by the straight-line fit of *MPR* versus time on the semi-log plot (Equations (2.9)-(2.10)).

$$\rho_1 = 2\sqrt{\eta_a e^{-(b/m)-\gamma}} \tag{2.9}$$

$$\rho_2 = \rho_1 e^{0.5/m} \tag{2.10}$$

We derive Equation (2.11) from Equation (2.4) to calculate the leakage rate (q_l) using the observed pressure changes and the estimated distances.

$$q_l = \frac{2\pi k_a h_a (\Delta P_{a1} - \Delta P_{a2})}{\mu B \ln\left(\frac{\rho_2}{\rho_1}\right)} \tag{2.11}$$

Next, we apply ρ_1 and ρ_2 to locate the leaky well. The two observation wells and the leaky well can be assumed as three corners of a triangle (triangle ABC in Fig. 2.2). The distance between the two observation wells is known and the lengths of the two other sides of the triangle are ρ_1 and ρ_2. In order to locate the leaky well, we also need to find the angles. According to the basics of the trigonometry, a triangle can be completely identified if the lengths of its three sides are known. Therefore, the leaky well can be located. The geometric process is based on the general relationship between the sides and angles of the triangles. For instance, in triangle ABC (Fig. 2.2):

$$\frac{AB}{\sin(\theta_3)} = \frac{BC}{\sin(\theta_1)} = \frac{AC}{\sin(\theta_2 + \theta_4)} \tag{2.12}$$

Equation (2.12) can be adapted for all triangles. The complete geometric procedure of locating the leaky well is explained in details in the Appendix 1. During this procedure, the distance of injection and leaky well (*R*) is also calculated, which is required to estimate the leakage coefficient of the leaky well. The geometrical approach is designed so that at least one of the three points (injection well and two leaky wells) is off the line connecting the other two points. *C'* is the mirror-image

point of the leaky well, which is at same distances from the observation wells as *C*. However, the distance from the injection well to the mirror-image point (*R'*) is generally unequal to the distance from injection well to the leaky well ($R \neq R'$), because the injection well and the two observation wells are not located on a single straight-line. Therefore, the pressure changes of the observation wells would be different if the mirror-image point was the location of the leaky well. Using Equation (2.1), we can compare the pressure results of these two points (*C* and *C'*) and eliminate the second possible location. In addition, the leaky well may be located by comparing the calculated distances with those for nearby P&A wells in the field. Nevertheless, this geometrical approach is required, especially when there are several wells at the relatively identical distances in different directions, or if the information about the history of well trajectories for the entire field is not available.

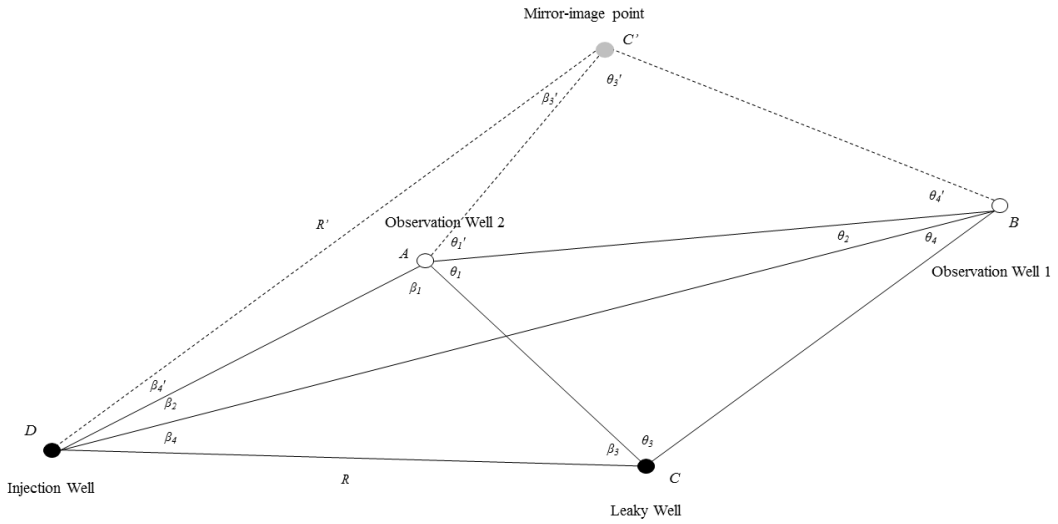

Fig. 2.2. Schematic representation of the wells in a horizontal plane

In order to estimate the leakage coefficient of the leaky well (α), we need to expand the single layer (AZ) approach to both layers, because α represents the effective permeability of the leaky well. It can be investigated only by consideration of the hydraulic connection of the two

layers. We apply the real time analytical solution of Zeidouni and Vilarrasa (2016) given by Equations (1)-(3) to estimate α.

We can directly calculate κ at each time by Equation (1) using estimated distances and leakage rate. The plot of κ versus time results in a horizontal line that would be the value of κ. Next, we calculate leaky well permeability (k_l) and leakage coefficient (α) using Equations (2.2)-(2.3).

Identification of leaky well from leaky caprock and leaky fault

As mentioned earlier, pressure change in the AZ is not necessarily related to focused leakage through a well. A local/regional weakness in the caprock and leaky fault are other possibilities that can lead to leakage and pressure changes in the AZ. If the observed pressure signals from the AZ are related to the other possible pathways, the pressure interpretation results are meaningless. Therefore, characterization of well leakage should be preceded by identification procedure to determine that leakage is actually caused by a focused wellbore leakage. Given the nature of flow for diffuse leakage and fault leakage events, we extend the pressure interpretation method to identify diffuse leakage and fault leakage from focused leakage.

2.4. Identification of diffuse caprock leakage

Fluids are often injected at lower temperature than the host injection zone in the subsurface. Injection of cooler fluids would make a cold region around the wellbore in the reservoir as well as caprock, which may lead to caprock damage (Vilarrasa, Olivella, Carrera, & Rutqvist, 2014). As a result, leakage may occur through a high-permeability region in the caprock close to the wellbore (Fig. 2.3). The leaky well causes radial flow in the AZ that can be recognized by the zero-slope logarithmic derivative curve (referred to as derivative hereafter). The caprock leakage would ultimately show radial flow at late time. However, the early time behavior of caprock leakage is

different from the well leakage. The early time flow regime caused by a permeable point in the caprock would be spherical flow (-1/2 slope line at pressure derivative curve), because the pressure pulses travel in three dimensions from a point source. However, the permeable region in the caprock layer provide regional leakage, which leads to spherical stabilization (-3/2 slope line). Similar to well leakage section, we need an alternative for unknown leakage rate to normalize the AZ pressure response. We extend the application of the pressure difference of the two observation points as a proxy for diffuse leakage rate. In identification section, we show that the AZ pressure derivative would reach the -3/2 slope line at early time, after deconvolution with respect to the time variable leakage rate.

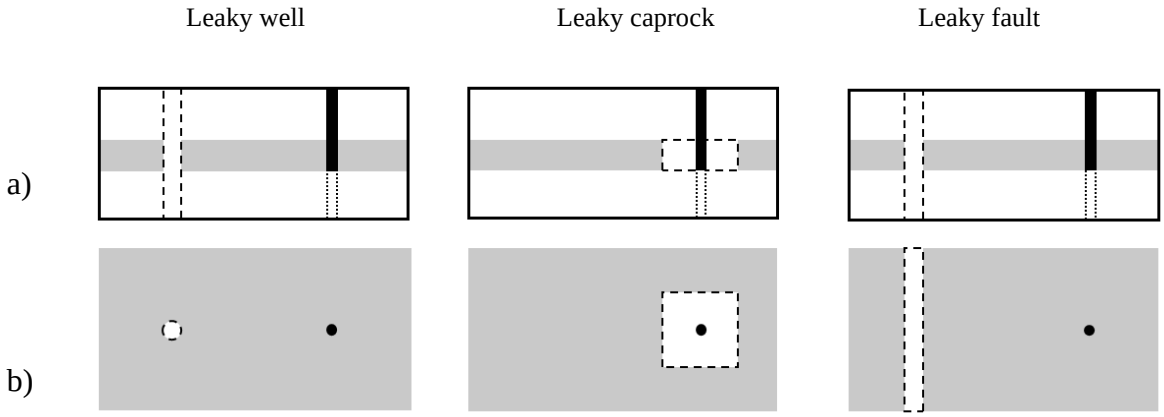

Fig. 2.3. Geometry of leakage pathways in the two-layer system shown in (a) side view, and (b) top view. The dashed lines show leaky pathways and the gray color shows the caprock layer. The injection well is shown by black non-perforated section in the AZ and caprock and the dotted lines that show perforated section in the injection zone.

2.5. Identification of fault leakage

In this section, we extend the identification technique to fault leakage. Leaky fault is a planar structure that conducts fluid through the planar interface (horizontally and vertically). Fig. 2.4 exhibits the schematic of fluid flow into the fault, inside the fault, and into the AZ. Fluid flow inside the fault would occur in three directions (x, y, and z) and fault permeability may be different

in the three directions (see k_{fx}, k_{fy}, and k_{fz} in Fig. 2.4). A leaky fault consists of a low permeability core zone bounded by fractured damaged zone. The core zone is made of ground materials, because it has been the slippage location of the faulted system. Due to the low permeability of the core zone, fault permeability in perpendicular direction to the fault plane (k_{fx}) may be less than the reservoir permeability. However, fault permeability could be significantly high parallel to the fault plane (k_{fy} and k_{fz}), due to the high permeability of the damaged zone. The planar interface and permeability anisotropy of the fault may result in linear flow regimes in the AZ. Later we show that, we can identify fault leakage based on the flow regime identification with the *MPR*.

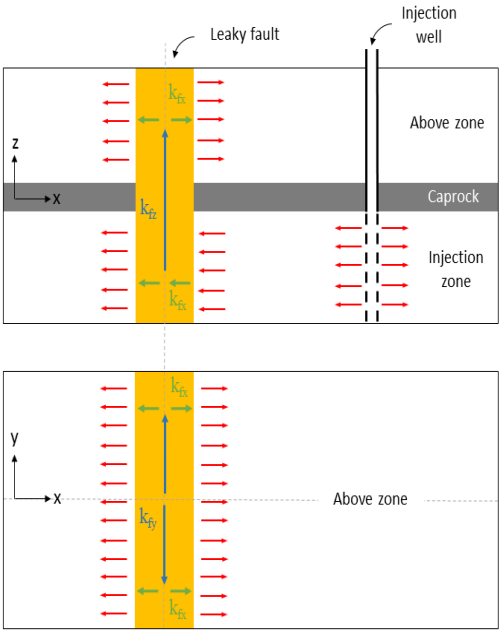

Fig. 2.4. Schematic representation of fault leakage from side view (x-z plane) and AZ top view (y-x plane). Fault leakage shows linear flow geometry in the AZ indicated by red flow lines at the fault.

Results and discussion

In this section, we apply the leakage identification and characterization techniques discussed above. We provide an example problem for AZ pressure interpretation applying the well leakage characterization procedure. Next, examples for leakage identification of leaky caprock and leaky fault form the leaky well are presented.

2.6. Well leakage example problem

In this part, we interpret the AZ pressure data for focused leakage characterization. Fig. 2.5 illustrates the synthetic pressure data of two observation points in the AZ of a two-layer system similar to the system shown in Fig. 2.1. The pressure data are obtained using a commercial numerical simulation software (CMG, 2015). There are three layers (Injection zone, caprock, and above zone) discretized to 300000 grid blocks. The maximum size of the grid blocks is 10000 meter and local grid refinement has been done around the wells. The minimum size of the grid blocks is 0.25 meter. The porosity, permeability, total compressibility, fluid viscosity, and thickness of both zones (injection and above zones) are 0.1, 10^{-13} m^2, 10^{-10} Pa^{-1}, 0.0005 Pa.s, and 100 m, respectively. The radius of injection well is 0.1 m and injection rate is 0.05 m^3s^{-1}. The corresponding MPR and the logarithmic derivative are shown in Fig. 1.5. The zero slope on the derivative curve corresponds to the radial flow regime in the AZ. Table 2.1 lists the input parameters for this example problem. The distance between the two observation wells is 110 m and distances between observation wells and the injection well are 99 m and 100 m.

Table 2.1. Properties of the example leaky well system

Parameter	Value	Parameter	Value
k_l (m^2)	10^{-9}	c_t (1/Pa)	10^{-10}
R (m)	50	ϕ	0.1
h_l (m)	200	k (m^2)	10^{-13}
r_l (m)	0.3	h (m)	100
μ (Pa.s)	0.0005	q (m^3/s)	0.05
c_{ta} (1/Pa)	10^{-10}	r_w (m)	0.1
ϕ_a	0.1	ρ_1 (m)	50
k_a (m^2)	5×10^{-14}	ρ_2 (m)	100
h_a (m)	100	α	0.0225

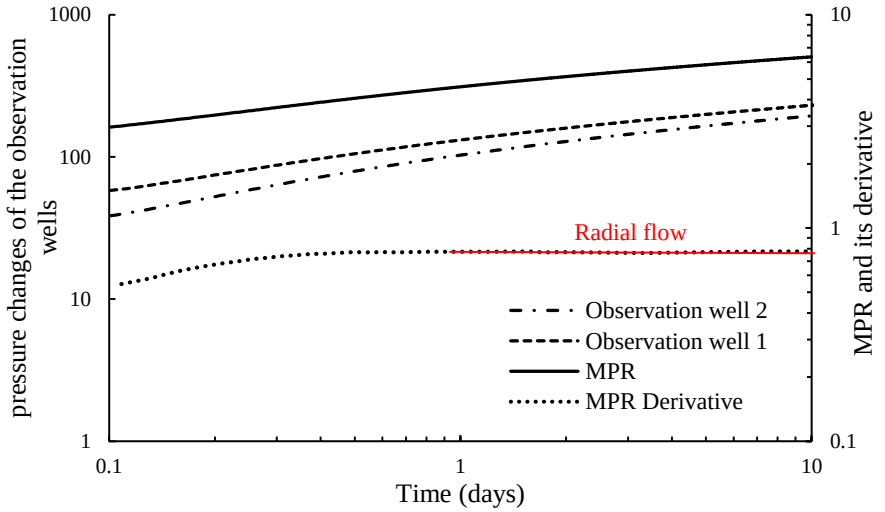

Fig. 2.5. Pressure changes of the observation wells, and the corresponding MPR and MPR derivative in log-log scale

In order to characterize the leaky well, we apply the semi-log straight-line method for radial flow characterization. We plot the *MPR* versus time on a semi-log plot (Fig. 2.6). The fitted line and the corresponding equation are shown in Fig. 2.6.

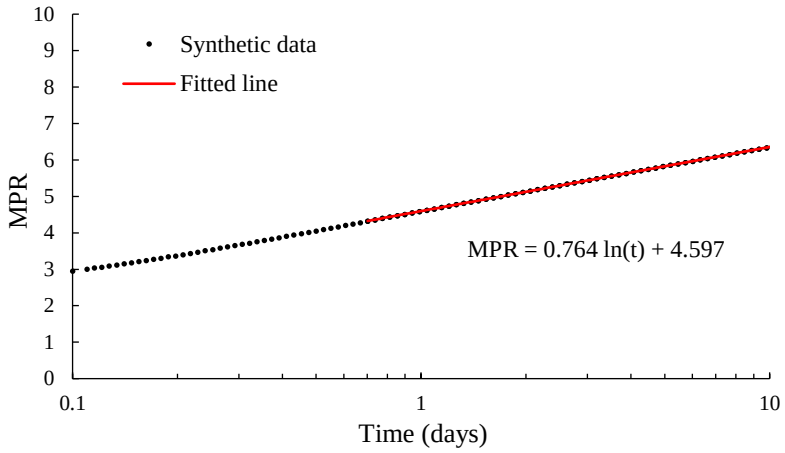

Fig. 2.6. Semi-log plot of MPR. The radial flow is characterized by straight-line method

Next, we can calculate the distances between the leaky well and the observation wells using Equations (2.9)-(2.10) applying slope and intercept of the fitted line (m = 0.764 and b = 4.597) in Fig. 2.6 which gives:

$\rho_1 = 48.6\,\text{m}$, $\rho_2 = 93.6\,\text{m}$

Next, the leakage rate is calculated versus time using Equation (2.11). The estimated distances of the observation wells show almost four to seven percent error from the actual values. In spite of this error, the calculated leakage rate is very close to the actual rate because the solution is very sensitive to leakage rate (Fig. 2.7).

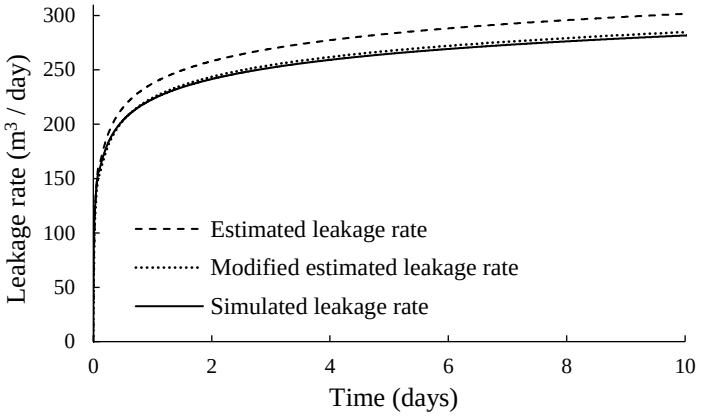

Fig. 2.7. Leakage rate through the leaky well (Estimated leakage rate is calculated with estimated location of the leaky well and the modified estimated leakage rate is calculated with the actual location of the leaky well)

Next, we locate the leaky well by the geometric procedure explained in the Appendix 1. Following the procedure we can calculate the angles shown in Fig. 2.2: θ_1=27.62, β_1=28.39, θ_2=56.88, θ_4=4.98, β_4=48.35

Angle β_4 shows the deviation of the leaky well from the injection well (Fig. 2.2). Next, we estimate the distance R between the injection well and the leaky well:

$R = 49.38$ m

The estimated location of the leaky well is shown in Fig. 2.8a. However, there is a second possible point (mirror-image point) with respect to the observation wells and calculated ρ_1 and ρ_2 (the gray point at Fig. 2.8a). The distance from the injection well to the mirror-image point can be calculated with the similar geometric procedure.

$R' = 127.2$ m

The mirror-image point is located at different distance from the injection well ($R' \neq R$). Therefore, it can be eliminated by comparing the actual above zone pressure response with the case that the leakage is occurring through the mirror-image point. We make this case by applying the estimated

parameters to Equation (2.1). The calculated distance between injection and leaky well (R) is 49.38 m, which shows almost two percent error (The actual value is 50 m). Fig. 2.8 shows the estimated location of the leaky well compared to the actual location.

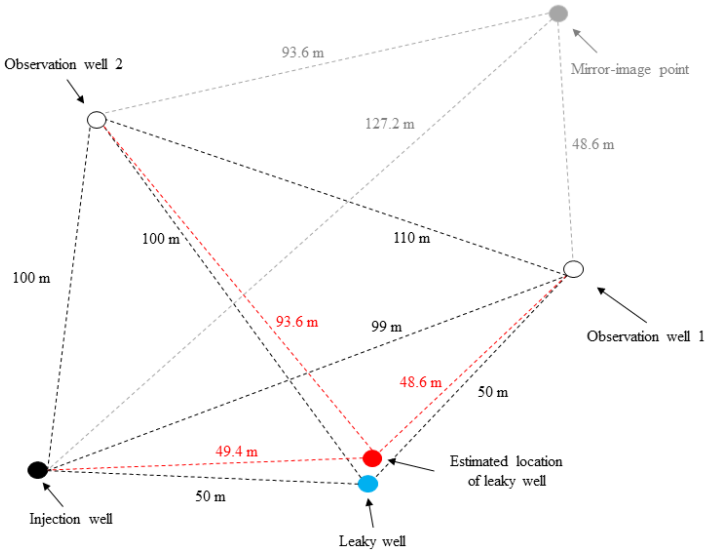

Fig. 2.8. Estimated location of the leaky well (red solid circle) compared to the actual location (blue solid circle). The mirror-image point is shown by the gray solid circle.

Although the estimated leakage rate is close to the actual value, we can still modify it to achieve higher accuracy. We can compare the estimated location of the leaky well with the locations of the existing abandoned wells in the field. If we find the leaking abandoned well, we can apply the actual location of the leaky well to modify the estimated leakage rate. In this example, we use R=50 m instead of 49.4 m as well as ρ_1=50 m and ρ_2=100 m (instead of ρ_1=48.6 m and ρ_2=93.6 m) to calculate q_l. Fig. 2.7 illustrates that the modified estimated leakage rate is closer to the actual leakage rate than the initially estimated leakage rate.

After locating the leaky well, we can estimate the hydraulic characteristics of the leaky well. The estimated κ constant is 27.3. The calculated leakage coefficient is α=0.0217 by r_l=0.3 m, which shows almost four percent error from the actual value (α=0.0225).

2.6.1. Identification from diffuse leakage

In this section, we show an example of AZ pressure response corresponding to caprock leakage to distinguish focused well leakage from diffuse caprock leakage. The spherical stabilization behavior of diffuse leakage at early time can be used to differentiate it from well leakage response, which is associated with radial flow. All the properties of the injection and above zones are identical to those given in the leaky well characterization example (Table 2.1). A high-permeability weakness of 4×4 m^2 is introduced in the caprock centered at the location of the injection well. The porosity and permeability of this region are 0.05 and 10^{-12} m^2, respectively. Numerical simulation results show that the simulated normalized pressure in the permeable region of the caprock layer is constant (results not shown here for brevity). Therefore, the permeable region of the caprock acts as a constant pressure boundary and causes spherical stabilization in the AZ. Fig. 2.9 illustrates the simulated pressure (CMG, 2015) in the AZ, which is normalized by the leakage rate. The derivative slope is -3/2 corresponding to the spherical stabilization of diffuse leakage. The number of grid blocks are 300000. The maximum size of the grid blocks is 10000 meter and local grid refinement has been done around the well. The minimum size of the grid blocks is 0.1 meter.

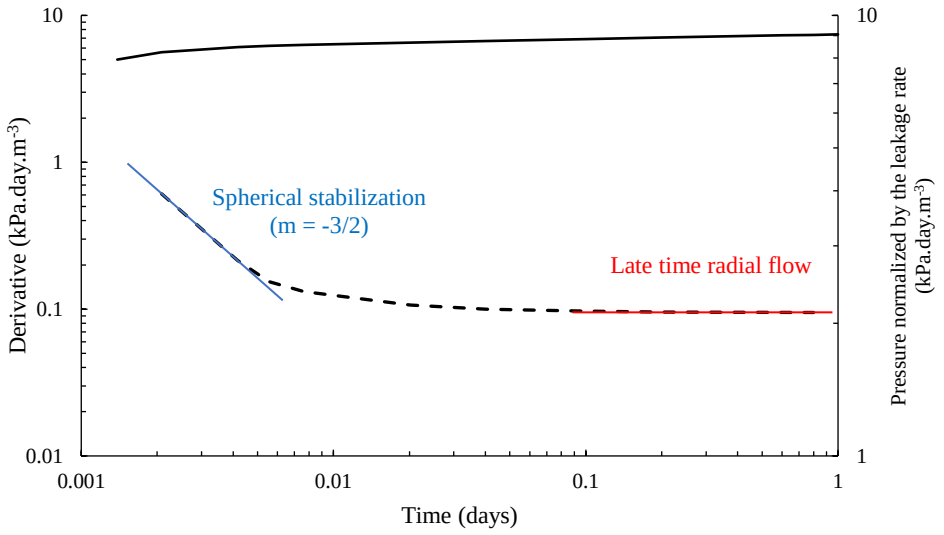

Fig. 2.9. Pressure response of AZ at r=2.25 m normalized by the leakage rate. The -3/2 slope line on the derivative curve shows the spherical stabilization during the early time of diffuse leakage.

Two observation points are considered in the AZ: the first one is at the location of the injection well and the second one is located at 10-m distance from that the injection well. Fig. 1.10 shows the MPR derivative of two observation points in the leaky caprock system. The negative slope of the derivative curve corresponding to the non-radial flow is the sign of diffuse leakage. If there was no upper boundary in the AZ (i.e. AZ thickness was infinite), spherical stabilization would have been fully established showing a -3/2 slope on the derivative plot. However, given the finite thickness of the AZ, the spherical stabilization may be terminated before being felt by the farther observation point. Therefore, a negative slope will be observed with magnitude less than 3/2 (Fig. 2.10).

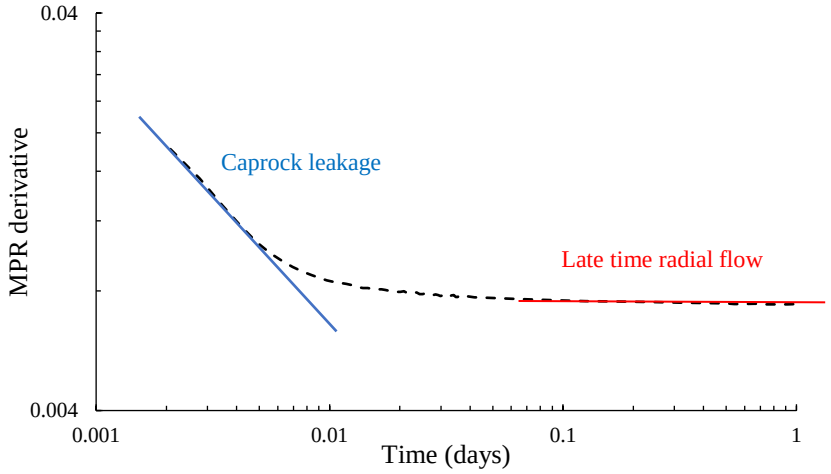

Fig. 2.10. MPR derivative of leaky caprock system. The negative slope line illustrates the diffuse leakage.

2.6.2. Fault leakage identification

In this section, we provide an example for identification of leaky fault using the deconvolution method. We simulated the two-layer fault system similar to Fig. 2.1 and replaced the leaky well with a vertically leaking fault. The properties of the fault system are identical to the properties that we used for leaky well and leaky caprock system (Table 2.1). Leaky fault acts as a discontinuity in the system with different permeabilities in three directions. $k_{fx}=10^{-18}$ m^2, $k_{fy}=10^{-9}$ m^2, and $k_{fz}=10^{-11}$ m^2 are fault permeabilities in x, y, and z directions (see Fig. 2.4). Fig. 2.11 shows the *MPR* of the simulated pressure data of two observation points and the corresponding derivative. The 1/2 slope line of the derivative curve in Fig. 2.11 indicates the linear flow caused by the leaky fault. The distances of the two observation points are 50 m and 100 m from the leaky fault.

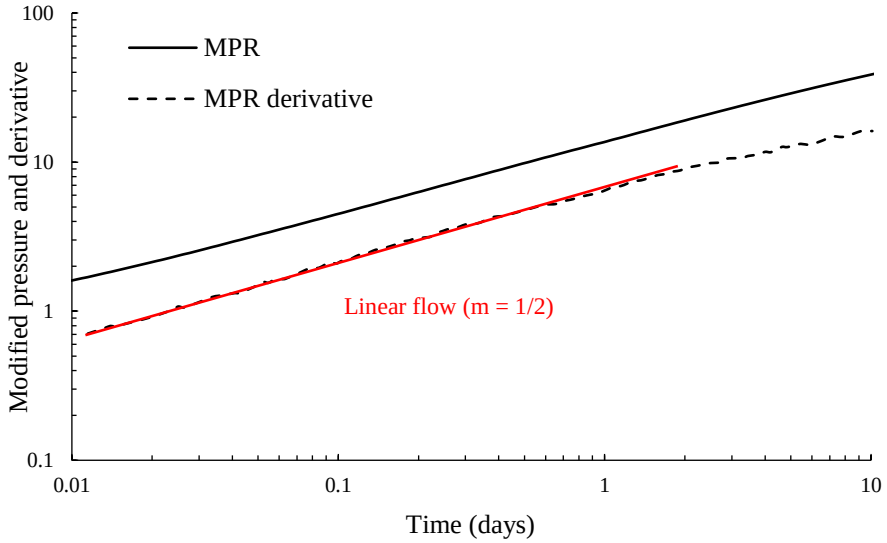

Fig. 2.11. MPR and the corresponding derivative for leaky fault system. The one-half slope line shows the linear flow of fault leakage.

Next, we investigate the minimum fault conductivity required to reach the linear flow during fault leakage to the AZ. We define fault conductivity in y-direction (see Fig. 2.4) as below:

$$\alpha_y = \frac{k_{fy} w_f}{kR} \tag{2.13}$$

where w_f is the fault width and R is distance from the injection well to the fault. Therefore, α_y is equal to 40 in Fig. 2.12. We simulated the fault system with different values of α_y. Fig. 2.12 illustrates that the linear flow of the fault leakage would occur when α_y is 40. The derivative line slope is between zero and one-half for smaller values of α_y.

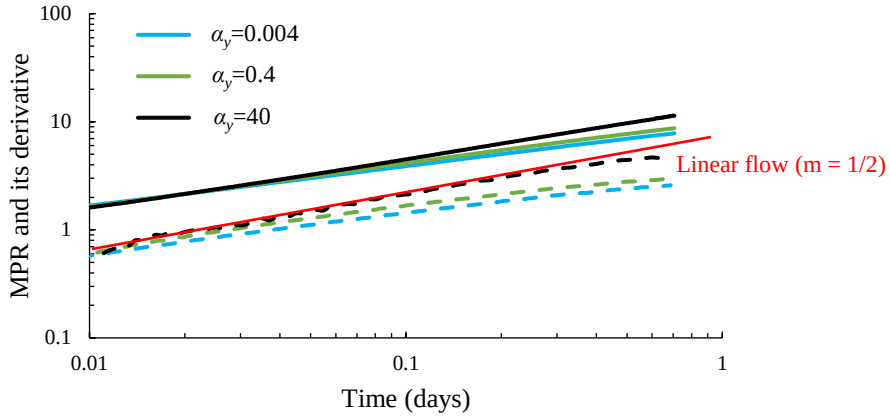

Fig. 2.12. Effect of fault horizontal conductivity through the fault plane (α_y) on the MPR of the two observation points in the AZ. The solid line is the MPR and the slotted line is its derivative (k_{fx}=10^{-18} m^2 and k_{fz}=10^{-11} m^2). Other system properties are identical to Table 2.1.

2.7. Increasing the radius of investigation in pressure testing

Radius of investigation (ROI) is a basic concept in pressure transient analysis, which is applicable to estimate distance to a specific structure in the reservoir (e. g. a fault), drainage area, hydrocarbon in place, and examine multi-fractured horizontal wells. The concept of ROI is consistent for radial flow regime. However, there is not a reliable method to explain ROI for linear flow, yet. In this section, we present an approach to increase the ROI for a linear source. We aim to significantly reduce the duration of test for a linear source. This approach will be useful for distinguishing fault leakage from well leakage from large distances. The linear flow regime of fault leakage happens at early time. If the observation points are not close enough to the linear source, the early-time linear signature of fault leakage would end before being reached to the observation wells. Another important application of linear flow is multi-fractured horizontal wells. Due to the low permeability of the shale reservoirs, the linear flow regime last for a long time. Increasing the ROI can significantly reduce the duration of pressure testing for reservoir characterization.

We provide the solutions for a constant rate and constant pressure linear source. Next, we apply different conditions for the linear source by convolution method to increase ROI.

2.7.1. Constant Rate

Diffusivity equation:

$$\frac{\partial^2 \Delta p(y,t)}{\partial y^2} = \frac{1}{\eta}\frac{\partial \Delta p(y,t)}{\partial t} \tag{2.14}$$

Initial condition and boundary conditions:

$$\Delta p(y,0) = 0\,, \quad \frac{\partial \Delta p(y_w,t)}{\partial y} = -\frac{q\mu B}{khx_f}\,, \quad \frac{\partial \Delta p(y_e,t)}{\partial y} = 0 \tag{2.15}$$

Dimensionless variables:

$$p_D = \frac{kh\Delta p}{qB\mu}\,, \quad t_D = \frac{\eta t}{{x_f}^2}\,, \quad y_D = \frac{y}{x_f} \tag{2.16}$$

Dimensionless form of the equation:

$$\frac{\partial^2 p_D(y_D,t_D)}{\partial {y_D}^2} = \frac{\partial p_D(y_D,t_D)}{\partial t_D} \tag{2.17}$$

$$\begin{aligned} &p_D(y_D,0) = 0 \\ &\frac{\partial p_D(y_{wD},t_D)}{\partial y_D} = -1 \\ &\frac{\partial p_D(y_{eD},t_D)}{\partial y_D} = 0 \end{aligned} \tag{2.18}$$

Next, we apply Laplace transform to time:

$$\begin{aligned} &\frac{\partial^2 \bar{p}_D(y_D,s)}{\partial {y_D}^2} = s\bar{p}_D(y_D,s) \\ &\frac{\partial \bar{p}_D(y_{wD},t_D)}{\partial y_D} = -\frac{1}{s} \\ &\frac{\partial \bar{p}_D(y_{eD},s)}{\partial y_D} = 0 \end{aligned} \tag{2.19}$$

Solution:

$$\bar{p}_D(y_D,s) = C_1 e^{-y_D\sqrt{s}} + C_2 e^{y_D\sqrt{s}} \tag{2.20}$$

Next, we apply boundary conditions:

$$\begin{aligned} -\sqrt{s}C_1 e^{-y_{wD}\sqrt{s}} + \sqrt{s}C_2 e^{y_{wD}\sqrt{s}} &= -\frac{1}{s} \\ -\sqrt{s}C_1 e^{-y_{eD}\sqrt{s}} + \sqrt{s}C_2 e^{y_{eD}\sqrt{s}} &= 0 \end{aligned} \tag{2.21}$$

Solution:

$$\bar{p}_{Du}(y_D,s) = \frac{\cosh\left((y_{eD}-y_D)\sqrt{s}\right)}{s\sqrt{s}\sinh\left((y_{eD}-y_{wD})\sqrt{s}\right)} \tag{2.22}$$

2.7.2. Constant Pressure

Diffusivity equation:

$$\frac{\partial^2 p_D(y_D,t_D)}{\partial {y_D}^2} = \frac{\partial p_D(y_D,t_D)}{\partial t_D} \tag{2.23}$$

$$\begin{aligned} &p_D(y_D,0) = 0 \\ &p_D(t_D,y_{wD}) = 1 \\ &\frac{\partial p_D(y_{eD},t_D)}{\partial y_D} = 0 \end{aligned} \tag{2.24}$$

Next, we apply Laplace transform to time:

$$\begin{aligned} &\frac{\partial^2 \bar{p}_D(y_D,s)}{\partial {y_D}^2} = s\bar{p}_D(y_D,s) \\ &\bar{p}_D(t_D,y_{wD}) = \frac{1}{s} \\ &\frac{\partial \bar{p}_D(y_{eD},s)}{\partial y_D} = 0 \end{aligned} \tag{2.25}$$

Solution:

$$\bar{p}_D(y_D,s) = C_1 e^{-y_D\sqrt{s}} + C_2 e^{y_D\sqrt{s}} \tag{2.26}$$

Next, we apply boundary conditions:

$$C_1 e^{-y_{wD}\sqrt{s}} + C_2 e^{y_{wD}\sqrt{s}} = \frac{1}{s}$$
$$-\sqrt{s}C_1 e^{-y_{eD}\sqrt{s}} + \sqrt{s}C_2 e^{y_{eD}\sqrt{s}} = 0 \tag{2.27}$$

$$\bar{p}_D(y_D, s) = \frac{1}{s}\frac{e^{y_{eD}\sqrt{s}}e^{-y_D\sqrt{s}} + e^{-y_{eD}\sqrt{s}}e^{y_D\sqrt{s}}}{e^{y_{eD}\sqrt{s}}e^{-y_{wD}\sqrt{s}} + e^{-y_{eD}\sqrt{s}}e^{y_{wD}\sqrt{s}}} \tag{2.28}$$

Solution:

$$\bar{p}_{Dp}(y_D, s) = \frac{e^{2y_{eD}\sqrt{s}+y_{wD}\sqrt{s}}e^{-y_D\sqrt{s}} + e^{y_{wD}\sqrt{s}}e^{y_D\sqrt{s}}}{s\left(e^{2\sqrt{s}y_{eD}} + e^{2\sqrt{s}y_{wD}}\right)} \tag{2.29}$$

$$\bar{p}_{Dp}(y_D, s) = \frac{\mathrm{Cosh}\left((y_{eD} - y_D)\sqrt{s}\right)}{s\,\mathrm{Cosh}\left((y_{eD} - y_{wD})\sqrt{s}\right)} \tag{2.30}$$

2.7.3. Using Duhamel's theorem to relate constant-rate and constant-pressure solutions

From superposition:

p_{Du} can be estimated using this equation to examine whether the constant rate solution was correct. Based on the constant rate solution:

$$\bar{p}_{wD} = \frac{\cosh\left((y_{eD} - y_{wD})\sqrt{s}\right)}{s\sqrt{s}\sinh\left((y_{eD} - y_{wD})\sqrt{s}\right)} \tag{2.31}$$

Therefore:

$$\bar{p}_D = \frac{\mathrm{Cosh}\left((y_{eD} - y_D)\sqrt{s}\right)}{s\sqrt{s}\sinh\left((y_{eD} - y_{wD})\sqrt{s}\right)} \tag{2.32}$$

This equation (as expected) is the same as the constant rate solution showing that solution was correct. We derive the constant pressure solution from the following convolution.

$$\bar{p}_D = s\bar{q}_{wD}\bar{p}_{Du} \tag{2.33}$$

We calculate the well flow rate for constant pressure well:

$$\bar{q}_{wD} = \left.\frac{d\bar{p}_D}{dy_D}\right|_{y_{wD}} = \frac{\mathrm{Sinh}\left((y_{eD}-y_{wD})\sqrt{s}\right)}{\sqrt{s}\,\mathrm{Cosh}\left((y_{eD}-y_{wD})\sqrt{s}\right)} \tag{2.34}$$

We can apply q_{wD} to obtain constant pressure solution from $\bar{p}_D = s\bar{q}_{wD}\bar{p}_{Du}$:

$$\bar{p}_D = s\frac{\mathrm{Sinh}\left((y_{eD}-y_{wD})\sqrt{s}\right)}{\sqrt{s}\,\mathrm{Cosh}\left((y_{eD}-y_{wD})\sqrt{s}\right)}\frac{\mathrm{Cosh}\left((y_{eD}-y_D)\sqrt{s}\right)}{s\sqrt{s}\mathrm{Sinh}\left((y_{eD}-y_{wD})\sqrt{s}\right)} = \frac{\mathrm{Cosh}\left((y_{eD}-y_D)\sqrt{s}\right)}{s\,\mathrm{Cosh}\left((y_{eD}-y_{wD})\sqrt{s}\right)} \tag{2.35}$$

This equation is the same as the constant pressure solution as expected.

2.7.4. Increasing ROI for various injection functions

In this section, we compare different wellbore conditions to investigate the arrival times of the pressure signals to the boundary of the closed system. We apply the equation $\bar{p}_D = s\bar{p}_{wD}\bar{p}_{Dp}$ to obtain rate normalized pressure (RNP). Figure below shows the RNP (solid line) and its derivative (slotted line) for the constant bottom-hole pressure condition. The arrival time is about t_D=0.01.

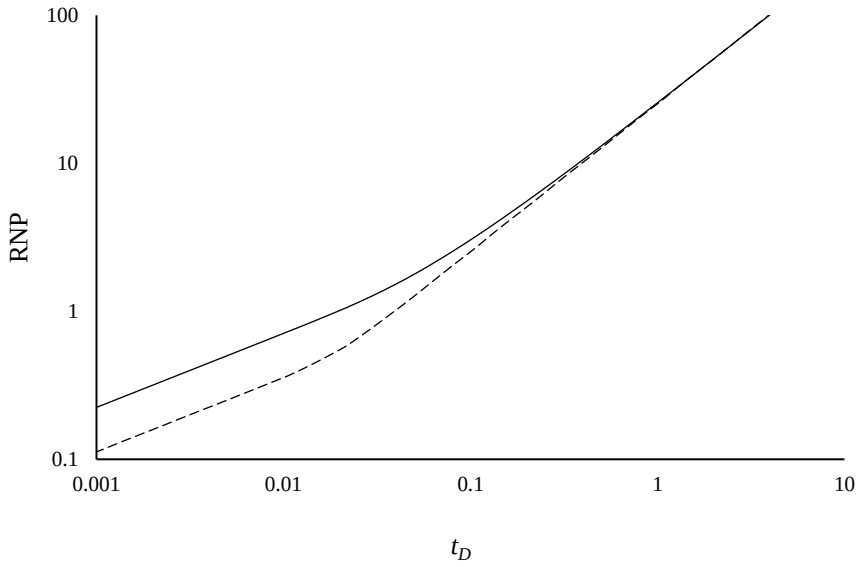

Fig. 2.13. Rate normalized pressure and derivative for constant bottom-hole pressure

Figure below shows that the arrival time is about t_D=0.01 for linear bottom-hole pressure condition.

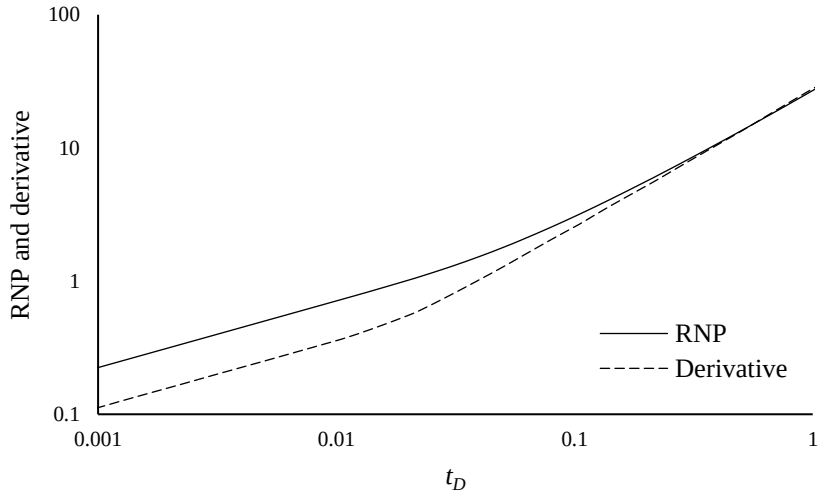

Fig. 2.14 Rate normalized pressure and derivative for linear bottom-hole pressure

Next, we examine the logarithmic bottom-hole pressure condition and the arrival time is still about t_D=0.01.

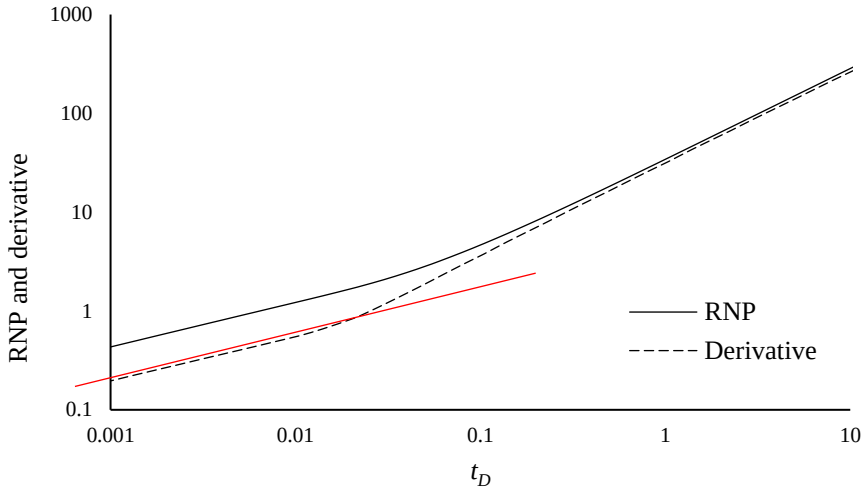

Fig. 2.15. Rate normalized pressure and derivative for logarithmic bottom-hole pressure

We aim to find a well pressure condition that increase the radius of investigation (ROI). Therefore, the arrival time should be shorter in the favorite condition. Next, we investigate the sinusoidal bottom-hole pressure (sin(ωt)). Figure 2.16 shows RNP of sinusoidal pressure for ω=1.

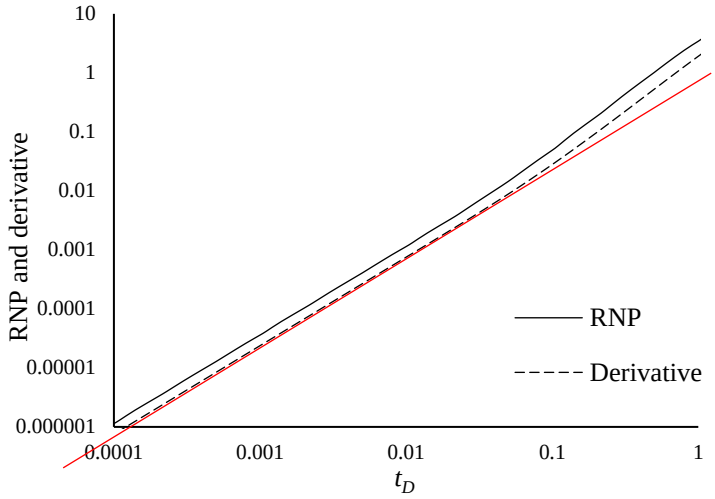

Fig. 2.16. Rate normalized pressure and derivative for sinusoidal bottom-hole pressure (ω=1)

Figure 2.17 shows RNP of sinusoidal pressure for ω=2.

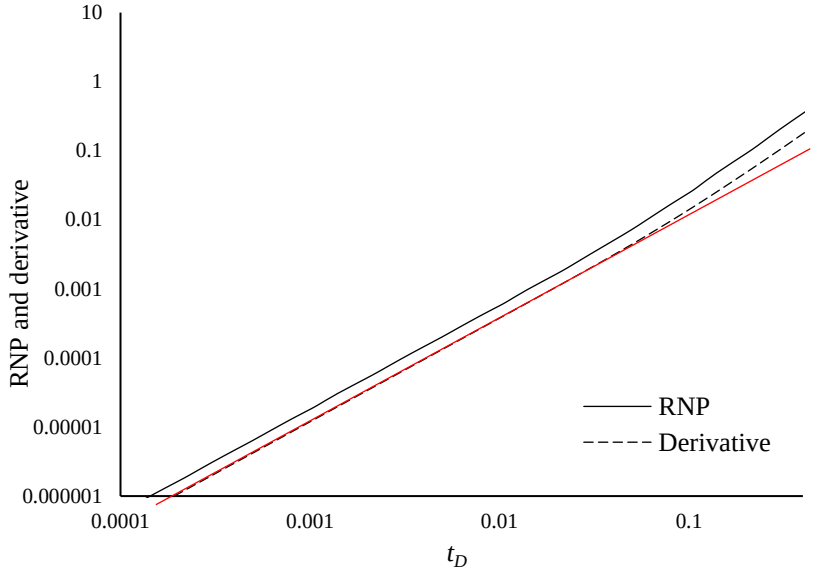

Fig. 2.17. Rate normalized pressure and derivative for sinusoidal bottom-hole pressure (ω=2)

Fig. 2.18 shows RNP of sinusoidal pressure for ω=0.5. Results show that the arrival time for sinusoidal bottom-hole pressure is about t_D=0.01.

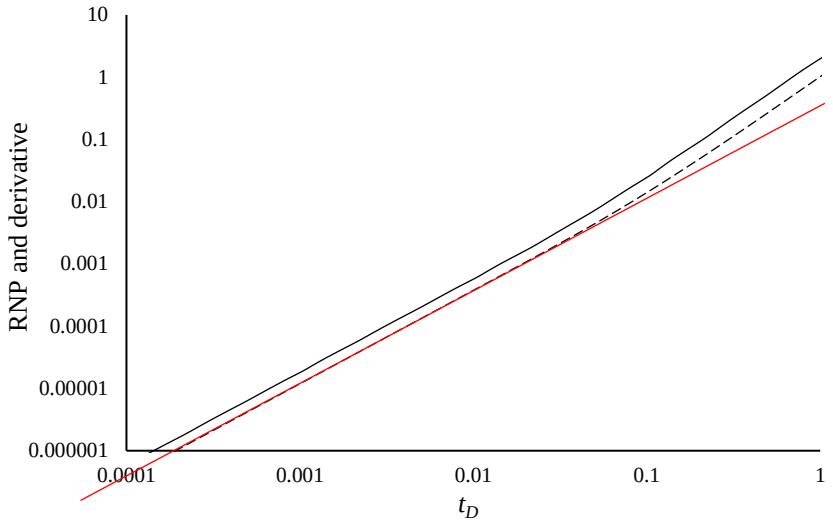

Fig. 2.18. Rate normalized pressure and derivative for sinusoidal bottom-hole pressure (ω=0.5)

Next, we investigate the quadratic function for bottom-hole pressure variations (p_{wD}=a.t_D^2+b.t_D+c). Figure below shows RNP derivative for the quadratic pressure (b=1, c=1). Figure below shows that the arrival time is significantly shorter for larger values of a.

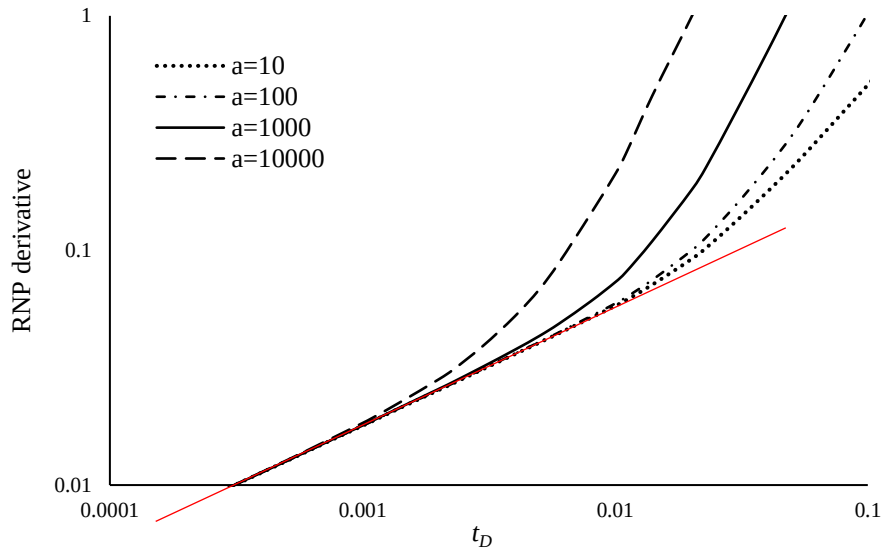

Fig. 2.19. Rate normalized derivative for quadratic bottom-hole pressure (b=c=1)

Next, we modify the coefficients of function $p_{wD}(t_D)=a.t_D^2+b.t_D+c$ to adjust them to field scale. The reservoir permeability, porosity, and thickness are 0.001 mD, 0.1, and 200 ft. Fluid viscosity is 2 cp, formation volume factor is 1.2 bbl/STB, and total compressibility is 6.89e-6 psi^{-1}. Figure below shows the bottom-hole pressure variations for $b=c=0.0001$.

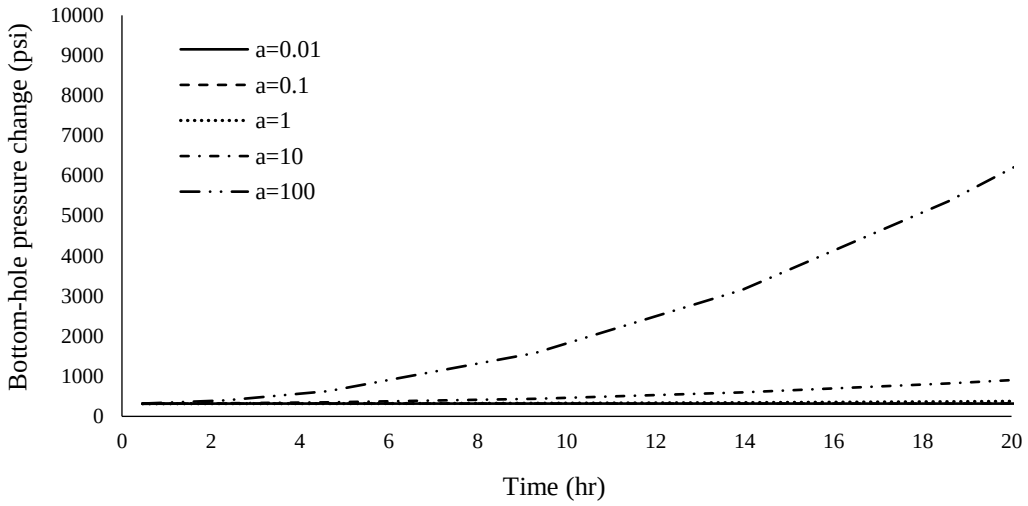

Fig. 2.20. Quadratic bottom-hole pressure change

Fig. 2.21 shows the RNP derivative for the quadratic bottom-hole pressure shown in above figure. The boundary dominated flow is stablished in less than 10 hrs for a=1. While the above figure shows that the bottom-hole pressure variations is less than 1000 psi for a=1 after 10 hrs.

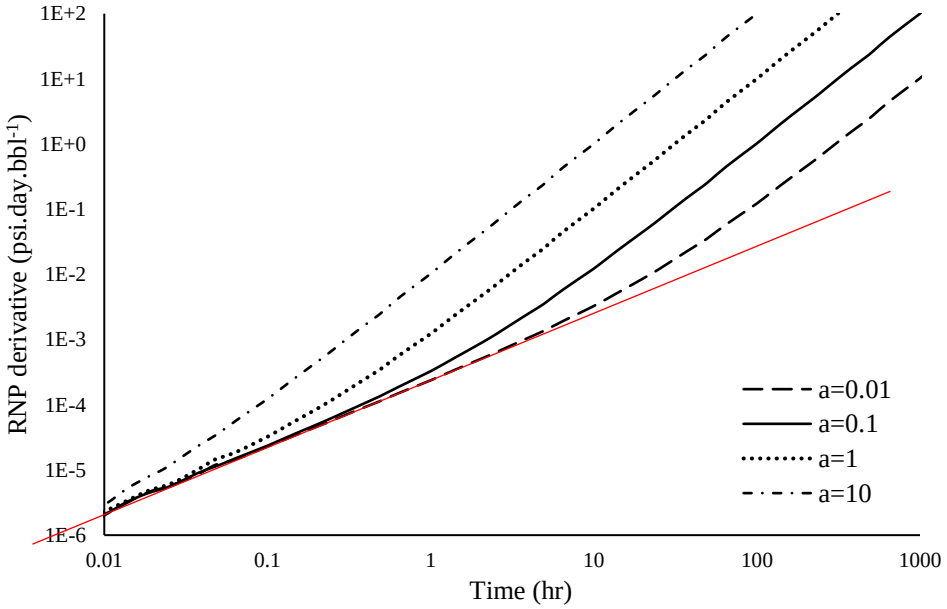

Fig. 2.21. Rate normalized pressure derivative for quadratic bottom-hole pressure (b=c=0.0001)

Next, we compare the quadratic pressure variations with the higher order function. Fig. 2.22 shows the RNP derivative for 3rd order polynomial function ($p_{wD}(t_D)$=a.t_D^3+ b.t_D^2+c.t_D+d), respectively. Figure 2.22 shows that the variations of a for 3rd order function ($p_{wD}(t_D)$=a.t_D^3+ b.t_D^2+c.t_D+d) can reduce the arrival time but not as much as the quadratic function (Fig. 21). The blue curve in figure below shows that the arrival time is significantly reduced by increasing b coefficient (the coefficient of t_D^2). Therefore, the best function to reduce the arrival time is the quadratic function.

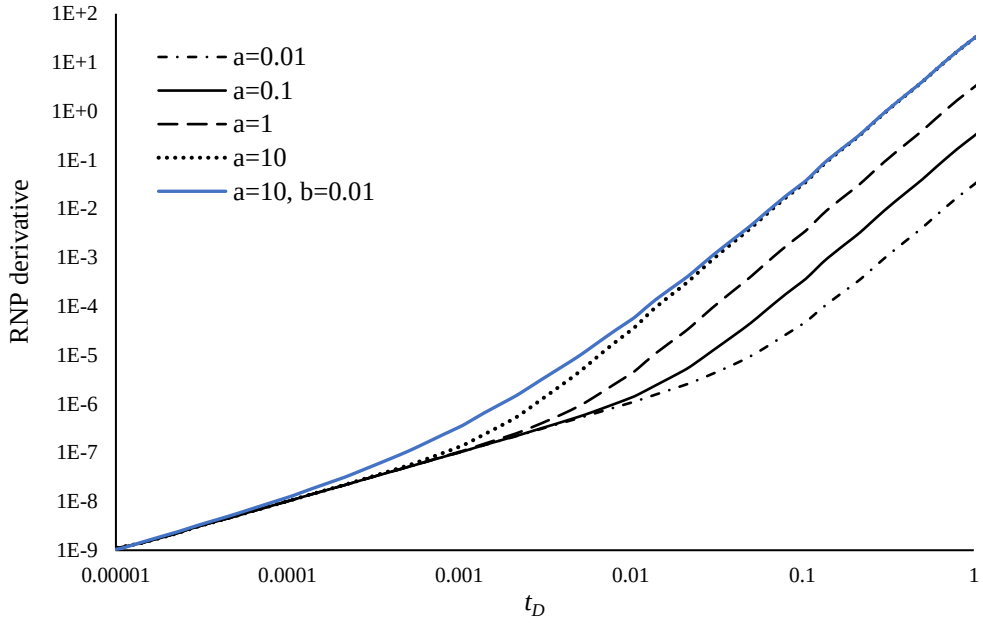

Fig. 2.22. Rate normalized pressure derivative for 3rd order polynomial bottom-hole pressure (b=c=0.0001)

Next, we design a test with quadratic pressure variations with a=100, b=0.0001, and c=0.0001. Fig. 2.23 shows the pressure variations and flow rate of this case after 20 hrs of test. Figure below shows the bottom-pressure and production rate. The reservoir initial pressure is 10000 psi.

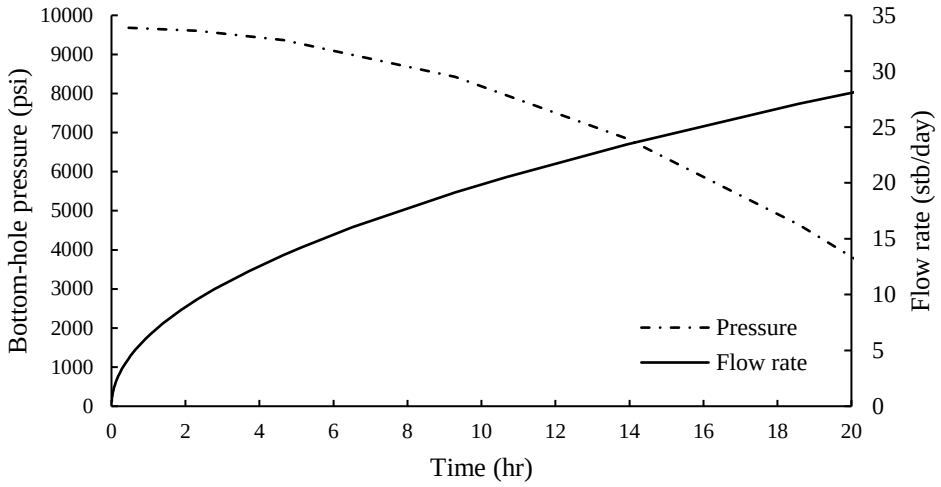

Fig 2.23. Bottom-hole pressure and well flow rate for the example problem

Fig. 2.24 shows that the arrival time is less than 0.1 hour.

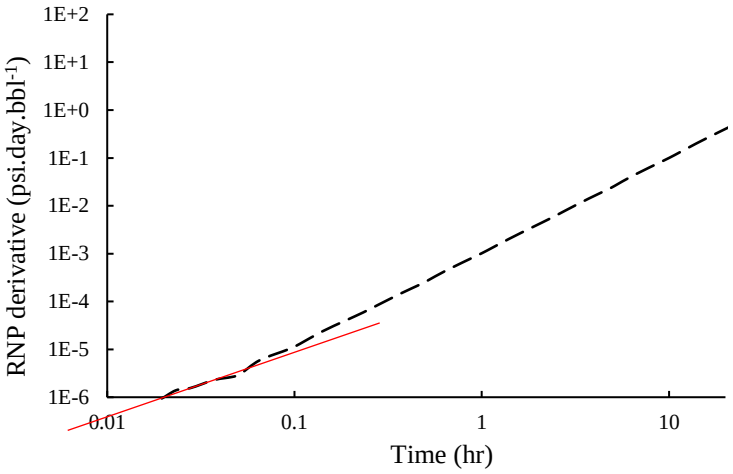

Fig. 2.24. RNP for example problem

2.8. Summary

In this chapter, we proposed a characterization method for the focused leakage through a leaky well applying the pressure changes of two observation points in the AZ. Identification of focused well leakage, caprock, and fault leakage is performed based on the diagnostic log-log plot of pressure derivative versus time. Because of time variability of leakage rate, pressure response

deconvolution is required to enable using the pressure derivative for leakage identification. We applied deconvolution to the AZ pressure with respect to the leakage rate. We applied the pressure difference of the two observation points as a proxy of unknown leakage rate to design the deconvolution process. The consequent derivative curve for diffuse leakage shows spherical stabilization (-3/2 slope derivative line) while that for focused well leakage shows radial flow characterized by zero-slope derivative. The spherical stabilization may not be fully established because the pressure pulse reaches to the top boundary before reaching to the farther observation point. In such a case, the derivative slope line would show a negative slope lower than 3/2 in magnitude. Next, we extended the identification process to fault leakage. Results show that the leaky fault causes linear flow with one-half slope line. The one-half slope line would occur if the along-fault conductivity (α_y) is sufficiently high. The derivative slope would be between zero and one-half for smaller values of α_y. For leaky well characterization, we estimated the location of the leaky well with semi-log straight-line method. Results show that the estimated location is close to the actual location of the leaky well. Next, we calculated leakage rate and leakage coefficient of the leaky well, which are in good agreement with the actual values. The identification and characterization procedures in this study are fast and straightforward without the need for optimization procedures that can be computationally expensive. We showed that the quadratic pressure variations can significantly increase the radius of investigation from a linear source. This fact reduces the arrival time for identification of the linear source.

CHAPTER 3. LEAKY FAULT

A fault is a potential pathway for fluid leakage, which can contaminate underground water resources. This chapter aims to develop an analytical method for fault leakage characterization both laterally and vertically using pressure transient analysis. In this chapter we develop analytical models to assess the pressure transient perturbations corresponding to production/injection from/into a reservoir with a leaky fault. Displacement of layers during the fault displacement may cause alteration of the reservoir properties across the fault. This alteration is accounted for by considering different properties on the two sides of the fault. The reservoir is divided into two regions separated by the fault, which are in hydraulic communication with one another and with the overlying/underlying permeable layers.

3.1. Introduction

A fault can cause a discontinuity in formation permeability distorting the fluid flow, and may act as a conduit to both lateral and vertical fluid flow. Fault zone permeability may be enhanced or reduced depending on the forces that cause the displacement of the layers and slip location through the fault plane (R. Sibson, 1977). Faults are generally composed of a core zone surrounded by a damaged zone. The permeability of the core zone is commonly low because this is the location of the slip that the original rock is ground. Compared to the core zone, the surrounding damaged zone's permeability may be enhanced due to possible fractures (Caine et al., 1996; R. Sibson, 1977). Analogous to the lateral permeability, the vertical permeability of a fault may be enhanced and the fault may be a vertical flow conduit (Maslia & Prowell, 1990). As an example, Bense and Person (2006) investigated the sealing and conductance behaviors of the Baton Rouge Fault in southern Louisiana and showed that the permeability of the fault is enhanced through the fault plane. They also found that the fault permeability is considerably low

perpendicular to the fault plane. The existence of faults in underground formations can cause inter-formational fluid migration, particularly affecting water resources (Huntoon & Lundy, 1979). Stoessell and Prochaska (2005) showed that brine from deep saline aquifers migrated upward along the Baton Rouge Fault by several hundreds of meters.

In this chapter, we investigate lateral and vertical characterization of leaky faults based on the pressure transient analysis (PTA). PTA is an applicable technique to characterize the hydraulic characteristics of the reservoirs, which is based on mathematical modeling of fluid flow in porous media. Many works have been done about pressure interpretation for leakage characterization. The main goal of this study is to present type curves for fault characterization and demonstrate how they can be used to uniquely determine the fault lateral and vertical conductivities. Analytical modelling of vertically and laterally leaking fault can be complex due to large number of variables related to properties of the fault, reservoir, and overlying/underlying zones connected to the reservoir by the fault. In obtaining the analytical solution, we build on an existing analytical solution by Zeidouni (2012). We also account for possible layer juxtaposition across the fault by assigning different reservoir properties to each side of the fault.

Analytical models are especially useful because of their independence of time and space discretization, capability for quick implementation, providing an explicit relationship between the system properties/measurements, and less complex models requiring fewer input of data. Several mathematical methods were used to present analytical solutions for fluid flow in a system including a fault as a discontinuity. Integral transforms (Bixel, Larkin, & Vanpoollen, 1963), Laplace-Fourier transformation (Ambastha, McLeroy, & Grader, 1989), and Green's function (Raghavan, 2010) are examples of the mathematical solution methods. Analytical approaches to modeling a faulted system are reviewed in the following.

Bixel et al. (1963) investigated the transient pressure behavior of a well located near a fault and proposed an analytical solution based on the integral transforms. Stewart and Gupta (1984) investigated interference testing in a reservoir including a non-sealing fault and introduced drawdown type curves using numerical simulation approach. The pressure discontinuity across the fault was shown by Yaxley (1987). He obtained an analytical solution for pressure transient behavior of a vertical non-sealing barrier. In his solution, the pressure interferences between wells separated by the fault were investigated for a reservoir with infinitely long dimensions and a constant-rate well. He presented type curves to calculate the conductivity of the fault from interference test, which may require long testing time. He suggested that a solution for drawdown at the active well can be useful to find the conductivity of the fault. The reservoir properties on both sides of the fault were assumed identical. Ambastha et al. (1989) assumed different reservoir properties at two sides of the fault and derived analytical solutions for pressure-transient behavior of a constant-rate well. They demonstrated that the results of the interference tests are influenced by the property contrasts of the composite system and the location of the observation well. Rahman et al. (2003) presented an analytical solution to the transient flow problem of a well located near a finite conductivity fault in a two-zone reservoir. The solution accounts for the transient flow within the fault. They concluded that the effect of transient flow in the fault can be negligible.

Modeling of the vertical leakage through the fault to shallower zones has received attention more recently. Shan et al. (1995) incorporated the effect of vertical fluid leakage to an upper permeable zone and suggested an analytical model of vertical flow through the fault. However, they ignored the pressure discontinuity through the fault in the injection layer. Zeidouni (2012) presented analytical solutions of two-layer and multi-layer systems, which demonstrated the pressure discontinuity through the fault in presence of vertical leakage. Zeidouni (2016) extended

the multi-layer solution for a leaky fault by fully accounting for the lateral resistance of the fault in all layers. Many other works have been done to address fluid leakage from a target zone (Birkholzer, Zhou, & Tsang, 2009b; Ebigbo et al., 2007; Mosaheb & Zeidouni, 2017a, 2017b; Pruess, 2005; Shakiba & Hosseini, 2016; Zeidouni & Pooladi-Darvish, 2012).

In this chapter, we develop two analytical methods for fault leakage characterization. First, we ignore the flow resistant of the above formation. In second model, we consider the resistance of the above formation as well as the anisotropic flow inside the fault zone.

3.2. Fault leakage to a high permeability zone

In the following, we first present the physical system followed by corresponding analytical model. The analytical solution is verified against numerical simulation results. The analytical solution is cast in the form of type curves to be used in fault characterization. Due to the large number of dimensionless groups obtained by the analytical solution, the system cannot be fully characterized using the type curves alone. Therefore, we present a computational optimization method in combination with type curves to fully characterize the reservoir-fault system. Our approach is based on estimating the dimensionless parameters that describe the hydraulic properties of the fault and the altered region on the other side of the fault. Finally, we apply our proposed method to two example problems to characterize leaky faults.

3.2.1. Analytical model

For the physical system to be modeled, the target zone is separated into two regions (region 1 and region 2) by a vertical planar fault. Region 1 is on the side of the fault where the active well is located and region 2 is on the opposite side of the fault (Fig. 3.1). Because of possible displacement of the layers on the two sides of the fault plane, the thickness and reservoir properties of region 2 may be different from those of region 1. The reservoir properties are homogeneous and

isotropic at each region. The *y*-axis is horizontal and perpendicular to the *x*-axis. The active well is assumed to be a line source/sink and is perforated over the whole thickness of the reservoir at $x=a$ and $y=0$ in the target zone. The reservoir is initially saturated with a single-phase fluid and the injected fluid is the same as the initial fluid. Both the upper zone and the target zone are infinite at both sides of the *x* and *y* axes. The fault plane is perpendicular to the *x*-axis, and it is located at $x=0$. The fault allows flow communications between region 1, region 2, and the upper zone. The horizontal and vertical permeabilities of the fault are considered constant.

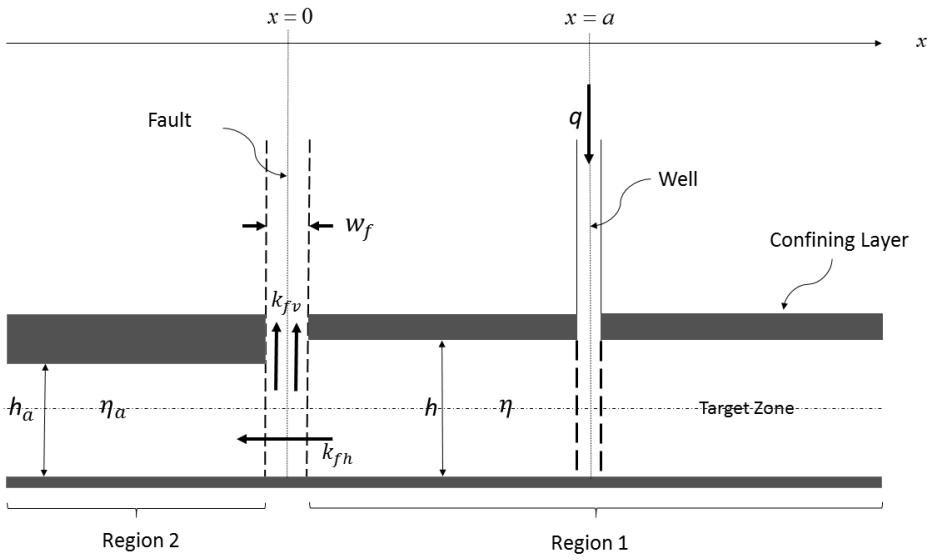

Fig. 3.1. Schematic representation of the physical model

The diffusivity equations for regions 1 and 2 make a system of two linear differential equations. The pressure change of the upper zones is negligible because the flow capacity of that zone is assumed to be large. Equations (3.1)-(3.10) represent diffusivity equations of regions 1 and 2 and the corresponding initial and boundary conditions:

Region 1:

$$\frac{\partial^2 \Delta p_1}{\partial x^2} + \frac{\partial^2 \Delta p_1}{\partial y^2} + \frac{q\mu}{kh}\delta(x-a)\delta(y) = \frac{1}{\eta}\frac{\partial \Delta p_1}{\partial t} \tag{3.1}$$

$$\Delta p_1(x, y, 0) = 0 \tag{3.2}$$

$$\Delta p_1(x, \pm\infty, t) = 0 \tag{3.3}$$

$$\Delta p_1(+\infty, y, t) = 0 \tag{3.4}$$

$$\frac{kh}{\mu}\frac{\partial \Delta p_1(0, y, t)}{\partial x} = \frac{k_{fh}h}{\mu w_f}(\Delta p_1(0, y, t) - \Delta p_2(0, y, t)) + \frac{k_{fv}w_f}{2\mu L}(\Delta p_1(0, y, t)) \tag{3.5}$$

Region 2:

$$\frac{\partial^2 \Delta p_2}{\partial x^2} + \frac{\partial^2 \Delta p_2}{\partial y^2} = \frac{1}{\eta_a}\frac{\partial \Delta p_2}{\partial t} \tag{3.6}$$

$$\Delta p_2(x, y, 0) = 0 \tag{3.7}$$

$$\Delta p_2(x, \pm\infty, t) = 0 \tag{3.8}$$

$$\Delta p_2(-\infty, y, t) = 0 \tag{3.9}$$

$$\frac{k_a h_a}{\mu}\frac{\partial \Delta p_2(0, y, t)}{\partial x} + \frac{k_{fv}w_f}{2\mu L}(\Delta p_2(0, y, t)) = \frac{k_{fh}h}{\mu w_f}(\Delta p_1(0, y, t) - \Delta p_2(0, y, t)) \tag{3.10}$$

where L is half thickness of the above zone. The system of partial differential equations and the corresponding initial and boundary conditions (Equations 3.1-3.10) are simplified to a system of ordinary differential equations using a combination of Laplace and Fourier transforms. Equations (3.11)-(3.12) state the sequence of applying Laplace and Fourier transforms to time and space domains:

$$\overline{\Delta p}(x, y, s) = \mathcal{L}\left[\Delta p(x, y, t)\right] = \int_0^\infty \Delta p(x, y, t) e^{-st} dt \tag{3.11}$$

$$\overline{\overline{\Delta p}}(x, \omega, s) = \mathcal{F}\left[\overline{\Delta p}(x, y, s)\right] = \int_{-\infty}^{+\infty} \overline{\Delta p}(x, y, s) e^{i.\omega.y} dy \tag{3.12}$$

where s and ω are Laplace and Fourier transform dummy variables, respectively. Equations (3.13)-(3.14) provide the final solution of the pressure distribution at region 1 and region 2, respectively in dimensionless form (the solution details are given in Appendix 2). The Laplace-Fourier domain is shown by = on the pressure change (Equation (3.12)) and dimensionless pressure (Equations 3.13-3.14).

$$\bar{\bar{p}}_{D1} = \frac{1}{2sA_1}\left(e^{-A_1|x_D-1|} + \frac{A_1\alpha - A_1\alpha_u - 2\alpha\alpha_u - {\alpha_u}^2 + A_1A_2T_D - A_2T_D\alpha - A_2T_D\alpha_u)}{A_1\alpha + A_1\alpha_u + 2\alpha\alpha_u + 2\alpha_u + A_1A_2T_D + A_2T_D\alpha + A_2T_D\alpha_u} e^{-A_1(x_D+1)} \right) \tag{3.13}$$

$$\bar{\bar{p}}_{D2} = \frac{\alpha}{s} \times \left(\frac{1}{A_1\alpha + A_1\alpha_u + 2\alpha\alpha_u + 2\alpha_u + A_1A_2T_D + A_2T_D\alpha + A_2T_D\alpha_u} e^{(-A_1+A_2x_D)} \right) \tag{3.14}$$

where:

$$p_{D1} = \frac{kh}{q\mu}\Delta p_1 \ , \quad p_{D2} = \frac{kh}{q\mu}\Delta p_2 \ , \ t_D = \frac{\eta t}{a^2} \ , \ x_D = \frac{x}{a} \ , \ y_D = \frac{y}{a} \tag{3.15}$$

$$\alpha = \left(\frac{k_{fh}(h+h_a)}{2w_f} \right) \Big/ \left(\frac{kh}{a} \right), \quad \alpha_u = \left(\frac{k_{fv}w_f}{2L} \right) \Big/ \left(\frac{kh}{a} \right) \tag{3.16}$$

$$T_D = \frac{k_a h_a}{kh} \ , \ \eta_D = \frac{\eta_a}{\eta} \tag{3.17}$$

$$A_1^{\ 2} = \omega^2 + s \ , \ A_2^{\ 2} = \omega^2 + \frac{s}{\eta_D} \tag{3.18}$$

w_f, k_{fv}, and k_{fh} are the fault width, fault vertical permeability, and fault horizontal permeability, respectively (Fig. 3.1). α and α_u are dimensionless horizontal and vertical conductivities of the fault and t_D is dimensionless time. T_D and η_D are flow capacity and diffusivity ratios, respectively. The solution must be inverted from the Laplace-Fourier domain to time-space domain. Analytical inversion of the solution to a closed-form solution in the time-space domain is difficult. Therefore, numerical Laplace and Fourier inversion methods are used to obtain the solution in time-space

domain. Stehfest algorithm (Stehfest, 1970) is used for Laplace inversion and the Inverse Discrete Fourier Transform (IDFT) is used for Fourier inversion.

3.2.2. Verification of the analytical model

The analytical solution is verified by comparison of spatial and temporal variation of the pressure with the numerical simulation results (CMG, 2015). There are three layers (Injection zone, caprock, and above zone) discretized to 300000 grid blocks. The maximum size of the grid blocks is 10000 meter and local grid refinement has been done near the well and the fault zone. The grid discretization is three dimensional. The minimum size of the grid blocks is 0.1 meter. We consider α=1, α_u=0.12, T_D=1, and η_D=1. According to the analytical model, these values of dimensionless parameters show the capability of fault for lateral and vertical leakage and alteration of the reservoir properties at region 2 due to displacement. In dimensional terms (corresponding to the dimensional values), the width of the fault is 0.1 m, the porosity is 0.2, total compressibility factor is 1×10^{-6} 1/kPa, and rate of injection is 0.005 m^3/s. The reservoir thickness and permeability of region 1 are 10 m and 10 mD, respectively. Fault lateral and vertical permeabilities are 0.01 mD and 5000 mD, respectively. The system specifications are given in Table 3.1. Fig. 3.2 exhibits the pressure distribution on the line drawn through the well perpendicular to the fault plane. The lateral pressure discontinuity is visible across the fault, which shows that the lateral permeability of the fault is less than the reservoir permeability. Fig. 2 illustrates that the analytical solution is in good agreement with the numerical simulation at both regions 1 and 2. If there is no lateral leakage, the pressure in region 2 remains constant (at initial pressure). Fluid leakage across the fault causes pressure changes in region 2. Therefore, the pressure gradient along region 2 shown in Fig. 3.2 (from x=-100 to x=0) is a sign of lateral leakage through the fault.

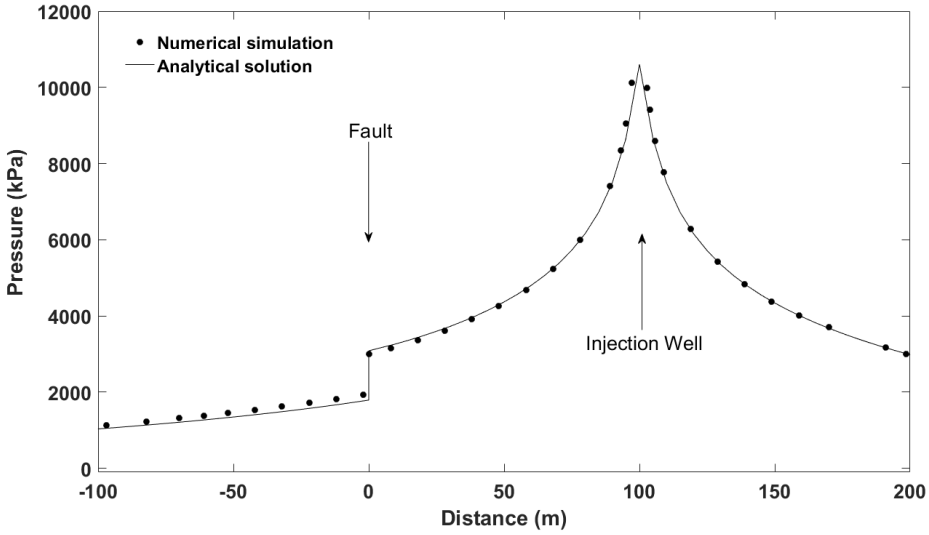

Fig. 3.2. Validation of the spatial pressure distribution in the injection zone after 10 days.

Fig. 3.3 illustrates good agreements of pressure and logarithmic pressure derivative (referred to as derivative hereafter) between analytical and numerical simulation. The verification of the pressure derivative is important because the characterization method to be presented later is based on the pressure derivative curves.

Table 3.1 Reservoir properties

Parameter	Value	Parameter	Value
Effective width of the fault (m)	0.1	Viscosity (cp)	0.5
Lateral permeability of the fault (mD)	0.01	Injection rate ($m^3.s^{-1}$)	0.005
Vertical permeability of the fault (mD)	5000	Porosity (fraction)	0.2
Target zone thickness (m)	10	Total compressibility (1/kPa)	10^{-6}
Fault-well Distance (m)	100	fault vertical conductivity , α_u	0.12
Permeability of region 1 (mD)	10	fault lateral conductivity , α	1
Permeability of region 2 (mD)	10	Diffusivity ratio , η_D	1
Permeability of upper layer (mD)	10	Flow capacity ratio , T_D	1

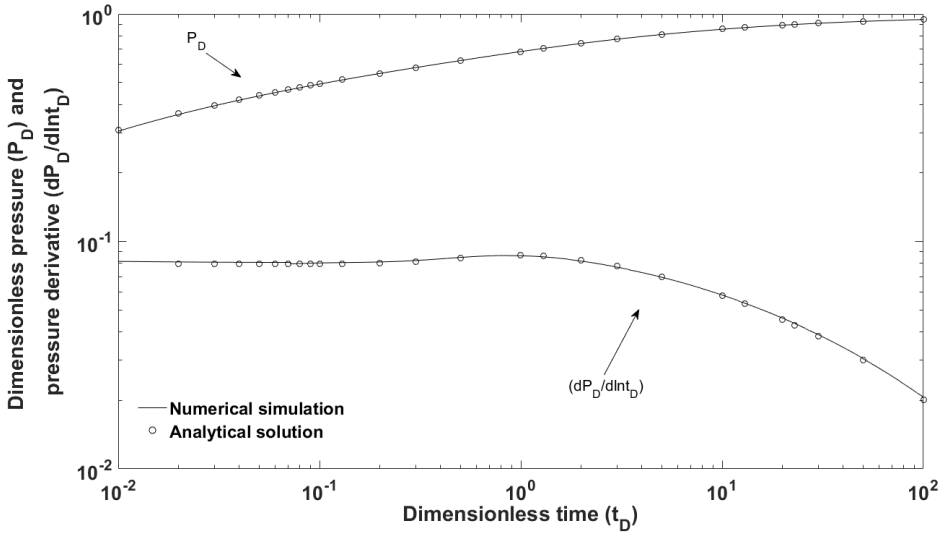

Fig. 3.3. Validation of temporal variation of well pressure and (logarithmic) pressure derivative with respect to time using numerical simulation

3.2.3. Fault characterization

In this section, type curves are introduced for characterization of the leaky fault modeled in previous sections. Type curves are generalized and adjusted in terms of dimensionless variables, which make them applicable to the corresponding system. Based on the analytical solution (Section 3), the reservoir-fault system can be characterized by four groups: Fault lateral and vertical conductivities, reservoir flow capacity ratio, and diffusivity ratio. These four groups are represented by dimensionless parameters: α, α_u, T_D, and η_D, respectively. We use the analytical model to provide type curves in terms of dimensionless parameters of the leaky fault system. Next, we present a characterization procedure based on the type curves.

3.2.4. Type curves

Fig. 3.4 illustrates the type curves corresponding to the leaky fault system in terms of fault lateral (α) and vertical (α_u) conductivities for $T_D = \eta_D = 1$. In these curves, the variations of the dimensionless bottom hole pressure of the injection well and its derivative are illustrated. We refer

to type curves of Fig. 3.4 as the base type curves. The type curves are grouped for various values of α_u. At each group, α varies from zero to infinity. The negative unit slope line of the logarithmic derivative curves in Fig. 3.4 shows the existence of the fault in the reservoir. Rahman et al. (2003) showed this negative unit slope line for different cases of fault leakage. The negative unit slope line would occur before appearance of flow resistance from the overlying/underlying zone unless the flow capacity of that zone is high enough. Using these type curves, hydraulic characteristics of the fault can be estimated with the well pressure data without detecting any resistance from the overlying/underlying zones.

A well pressure data corresponding to unique values of α and α_u would match with a unique type curve. In finding the matching type curve, α_u is easier to obtain from late time pressure data while parameter α is easier to estimate using early time data. Implementing this technique of using the early time and the late time data separately can help in resolving the choice of intermediate values of α and α_u. In other words, for two close values of α_u, the two corresponding groups of type curves may be very close to one another at late time, but the two curves should deviate from each other at early time making it easy to recognize which one belongs to which group. If two curves of two different groups of α_u are very close to each other at late time so that both match the given data, the early time curvature will be different for the two type curves and therefore, can be used to distinguish between them. In addition, two curves with too close values of α and different values of α_u may be close to each other at the early time. Then, their late time deviation can be used to determine the correct type curve. In short, there is a unique type curve for each combination of α_u and α which should be easy to distinguish from the other curves. In addition, the point when deviation from the radial flow (the zero-slope derivative line prior to reaching the fault) would commence are useful to find the best matching type curve.

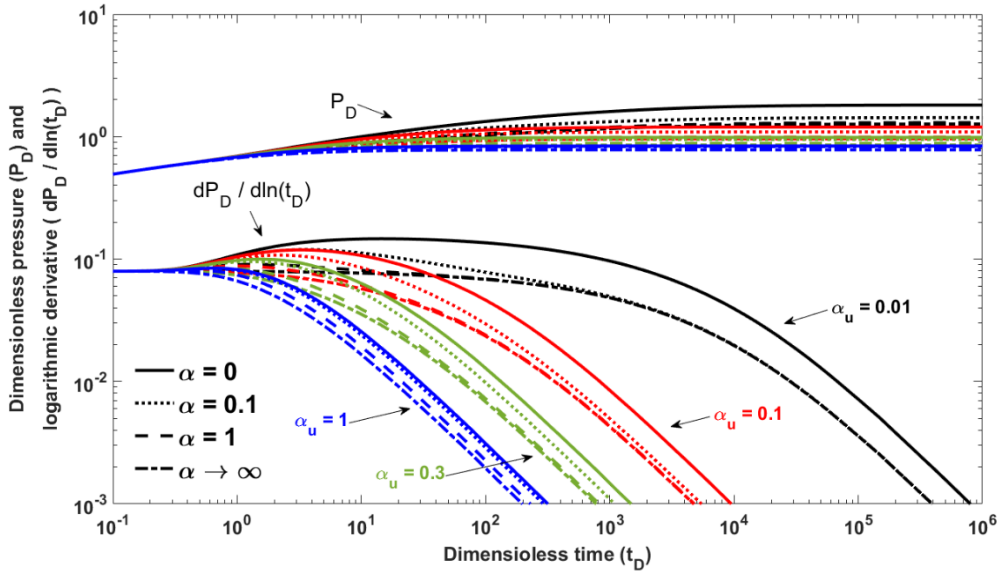

Fig. 3.4. Type curves of the leaky fault system considering T_D =1 and η_D =1

In order to use these type curves, the well pressure data should be plotted versus time in the same scale as the type curves on a transparent plot. The resulting plot should be next moved horizontally and vertically (without rotation) to find the best match with the type curves to estimate α and α_u. In addition to α and α_u, region 1 permeability and fault-well distance can also be evaluated based on the radial flow prior to reaching the fault. By selecting an arbitrary match point, we get $(p_D)_M$, $(\Delta p)_M$, $(t)_M$, and $(t_D)_M$ of that match point to calculate region 1 permeability (k) and fault-well distance (a) based on Equations (3.19) and (3.20).

$$k = \frac{q\mu}{h}\left(\frac{p_D}{\Delta p}\right)_M \tag{3.19}$$

$$a = \sqrt{\eta\left(\frac{t}{t_D}\right)_M} \tag{3.20}$$

One observation from these type curves is that 2 to 3 log-cycles of data may be required for identification of the fault characteristics. This implies that if the fault is felt after 1 hr test, 100 to 1000 hrs of test may be required to enable characterizing of the fault.

The type curves can be extended to determine T_D and η_D as well. Fig. 3.5 illustrates the effect of T_D and η_D on the pressure and pressure derivative for a fixed value of α (=0.1). The effect of T_D and η_D is most visible at the lowest values of α_u. Similar patterns are achieved for different values of α.

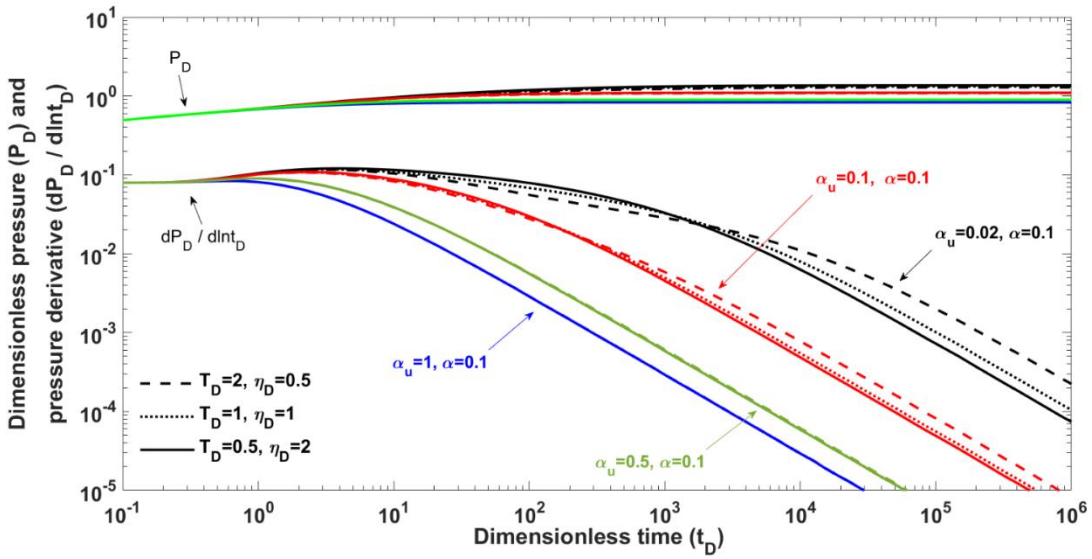

Fig. 3.5. Effect of T_D and η_D on the type curves

Fig. 3.5 shows that by increasing α_u, the sensitivity of the pressure derivative curve to the parameters T_D and η_D will decrease. In the following, we introduce a procedure to estimate the dimensionless parameters. First, initial values of α and α_u are estimated by the base type curves. Next, an optimization method is applied to find the accurate values of the dimensionless parameters using the initial values obtained from type curve analysis. We use the MATLAB built-in optimization tool given by the *fmincon* optimization function. This function is based on a

sequential quadratic programming, which is a gradient-based algorithm (2015). Here, fmincon optimization is applied to minimize the square of the difference between well pressure data and the mathematical solution by changing the four dimensionless parameters.

3.2.5. Characterization procedure

In characterization procedure, first, we estimate the initial values of α and α_u from the type curves. Next, we calculate the values of permeability and fault-well distances using Equations (3.19) and (3.20). In the optimization process, first, we use the late time pressure data to modify the estimated initial value of α_u. We fix α, T_D, and η_D at the initial values and modify α_u to find the optimum value of α_u starting with the estimated initial value. Next, we run the optimization process using the early time data to modify the value of α while the values of α_u, T_D, and η_D are fixed. After that, we apply the optimization process to modify α and α_u simultaneously using the whole pressure data.

As a final step, we apply the optimization process to modify the values of T_D and η_D while α and α_u are fixed. The initial values of T_D and η_D can be considered equal to 1. This step is done by the late time data because T_D and η_D have a negligible effect on the early time data. This sequential procedure improves the optimization process compared to optimizing all four dimensionless parameters simultaneously using the whole the pressure data. This optimization procedure can also be used in the case that T_D=η_D=1 to remove the possible errors. In this case, the final step is not required. The characterization procedure is summarized in Fig. 3.6.

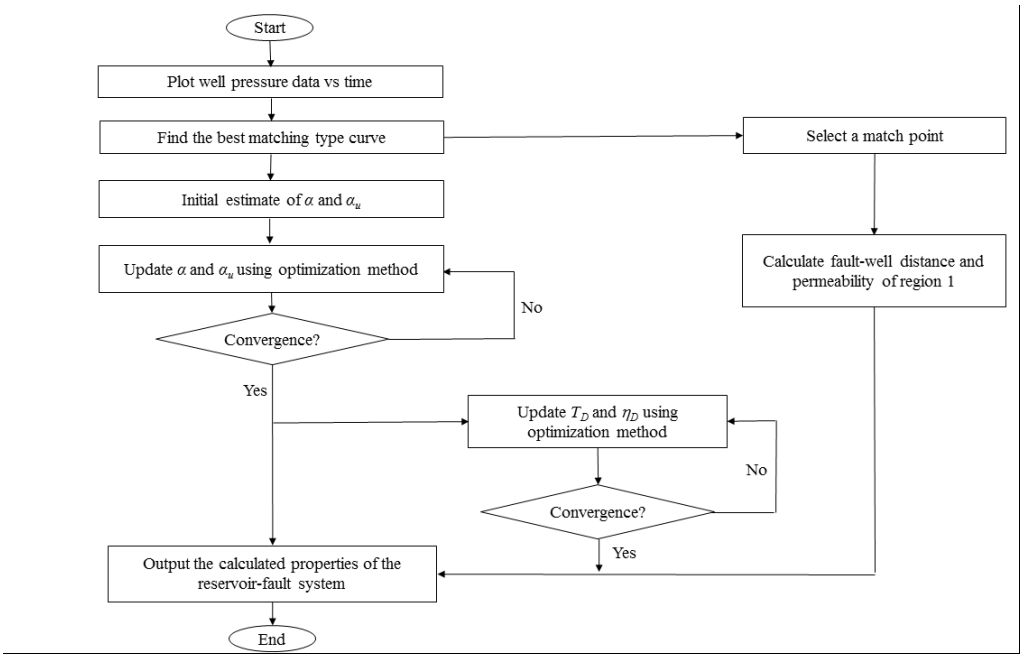

Fig. 3.6. Characterization procedure of the leaky fault system

3.2.6. Results and discussion

In this part, two examples are presented to estimate fault characteristics by the type-curve method using the procedure described in the previous section.

Example 1: No alteration of reservoir properties across the fault

In this example, we analyze the well pressure data of an injection well near a fault. The permeability, porosity, total compressibility, and thickness of the target zone at both sides of the fault are respectively 100 mD, 0.1, 10^{-6} 1/kPa, and 10 m. The flow capacity of the upper zone is large enough compared to the injection zone. The injection rate is 0.005 $m^3.s^{-1}$ and fluid viscosity is 0.5 cp. Fig. 3.7 shows the synthetic well pressure data and pressure derivative of the first example in which α and α_u are considered 1 and 0.3, respectively. These values correspond to 62 D and 0.1 mD for vertical and horizontal permeabilities of the fault considering a 0.1-m wide fault. Fluid leakage through the fault can be inferred from the derivative curve. If the fault is sealing, the pressure derivative becomes zero-slope after departing from the zero-slope corresponding to initial

radial flow (Fig. 3.8). The late time horizontal line in Fig. 8 exhibits the pressure response of a sealing fault in which α and α_u are equal to zero.

The pressure data and the derivative are required on a plot with the same scale as the type curves for type-curve matching. Fig. 3.9 shows the type curve that best agrees with the pressure data. Corresponding values of α and α_u are estimated for the fault. The estimated values of α and α_u are 1 and 0.3, which are the true values used in generating our synthetic data. By selecting an arbitrary match point and using equations (3.19) and (3.20), the permeability of region 1 and the fault-well distance can be calculated as below:

$$(p_D)_M = 0.08,\ (\Delta p)_M = 199\ \ kPa\ ,\ (t_D)_M = 0.07\ ,\ (t)_M = 1000\ \ s \tag{3.21}$$

$$k = \frac{q\mu}{h}\left(\frac{p_D}{\Delta p}\right)_M = 100.5 \text{ mD} \tag{3.22}$$

$$a = \sqrt{\eta (t/t_D)_M} = 100.2 \text{ m} \tag{3.23}$$

These values are in close agreement with the correct values (k=100 mD, a=100 m).

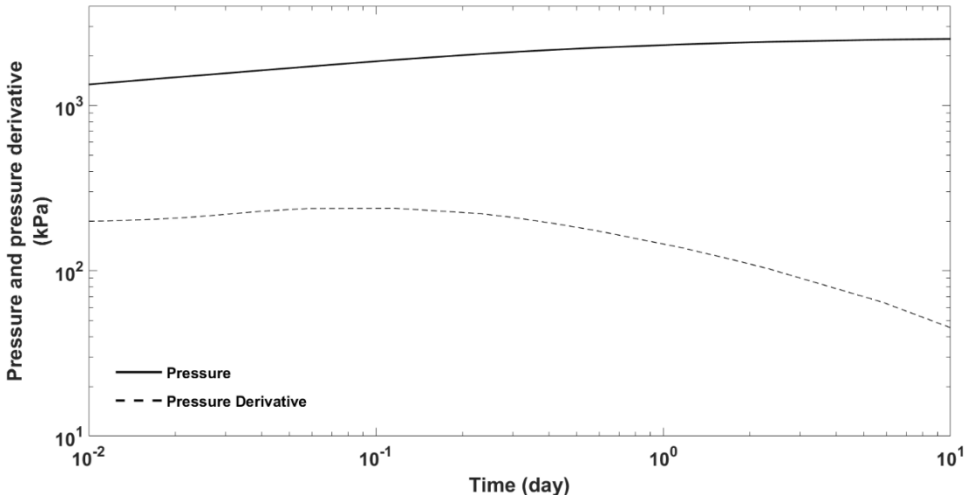

Fig. 3.7 Pressure and pressure derivative for example 1

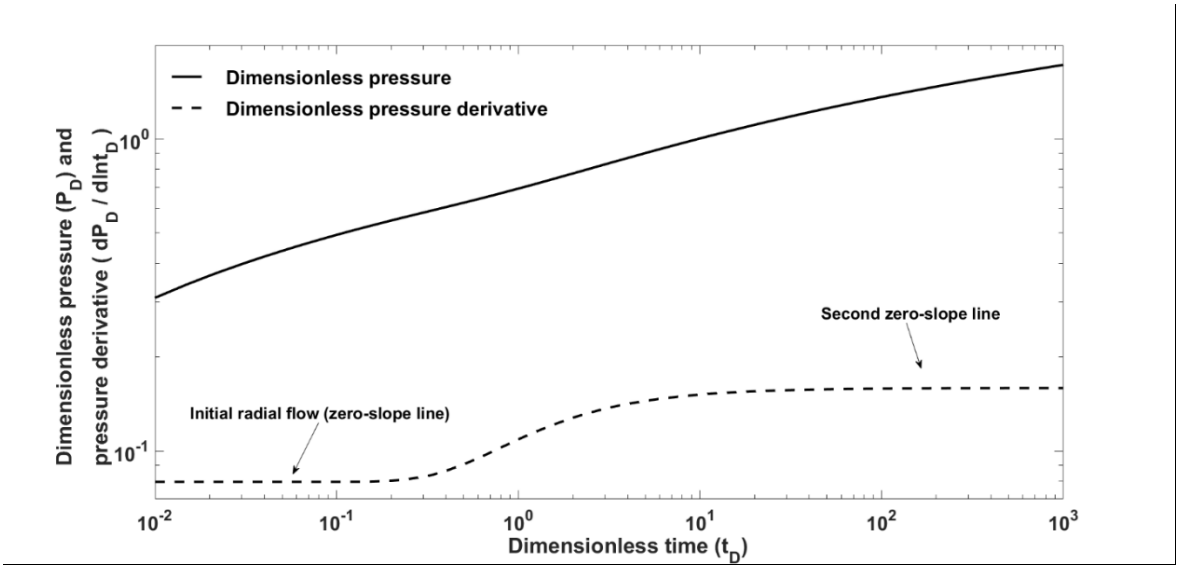

Fig. 3.8. Pressure and derivative response for a sealing fault, considering $\alpha = \alpha_u = 0$.

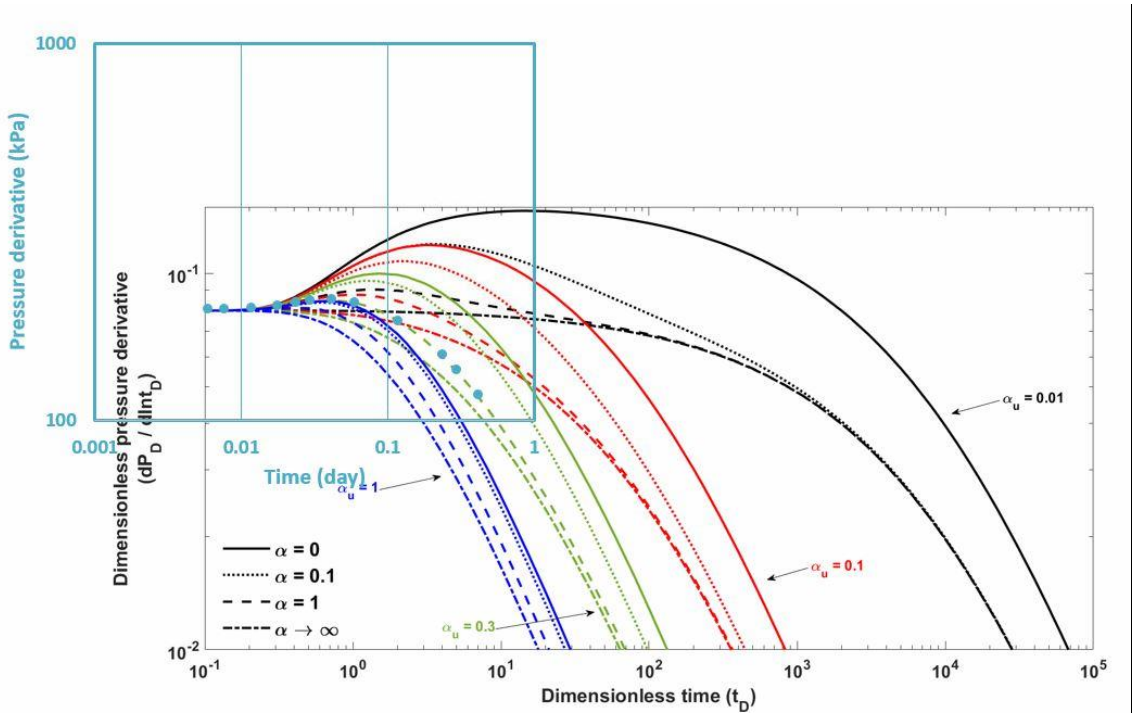

Fig. 3.9. Estimating α and α_u with the base type curves for example 1

Example 2: Alteration of reservoir properties across the fault

Fig. 3.10 shows the synthetic pressure data of an injection well near a fault in which α, α_u, T_D, and η_D are considered 0.02, 0.5, 0.1, and 0.1 respectively. The flow capacity of the upper zone is large in proportion to the injection zone. The reservoir properties and the formation thickness on region 2 are unknown. Therefore, we characterize the leaky fault while the reservoir properties of region 2 may not be identical to those of region 1. The injection rate is 0.005 $m^3.s^{-1}$, the viscosity is 0.5 cp, the porosity is 0.1, total compressibility is 10^{-6} 1/kPa, and reservoir thickness is 20 m. First, we use the base type curves to find the initial values for α and α_u. In this case, the pressure data curve may not accurately match with the type curves but we try to find the best match. The best match of the pressure data with the type curves is illustrated in Fig. 3.11. The estimated initial values of α and α_u are 0.2 and 0.03 respectively.

When $T_D \neq 1$ and/or $\eta_D \neq 1$, the effects of T_D and η_D on the pressure derivative curve appear after the arrival of the pressure pulse to the fault. Hence, variations of T_D and η_D will not affect the early time pressure data. Thus, similar to example 1, we can select an arbitrary match point to estimate the fault-well distance and permeability of region 1 (Equations (3.24)-(3.26)).

$$(p_D)_M = 0.098,\ (\Delta p)_M = 248 \text{ kPa},\ (t_D)_M = 1,\ (t)_M = 10022 \text{ s} \tag{3.24}$$

$$k = \frac{q\mu}{h}\left(\frac{p_D}{\Delta p}\right)_M = 49.4 \text{ mD} \tag{3.25}$$

$$a = \sqrt{\eta\left(t/t_D\right)_M} = 100.1 \text{ m} \tag{3.26}$$

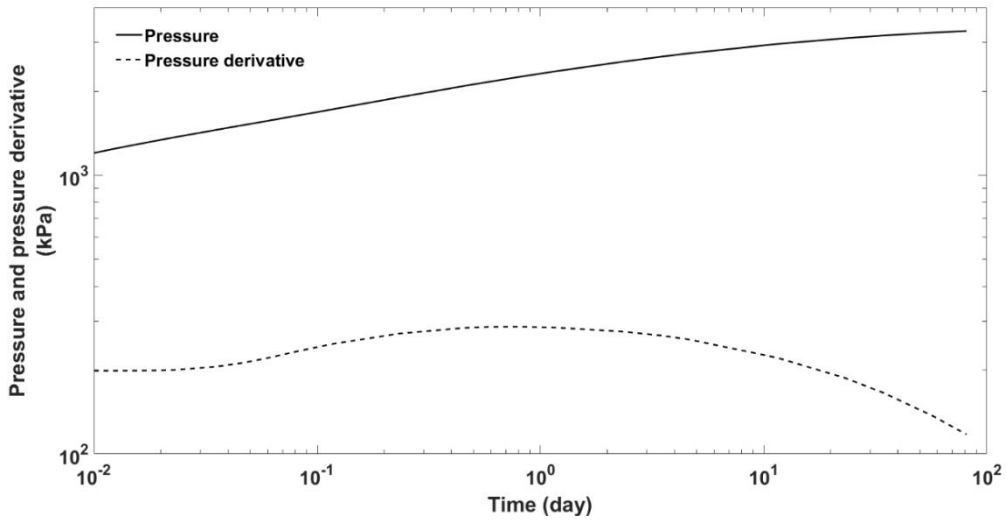

Fig. 3.10. Pressure and derivative data for example 2

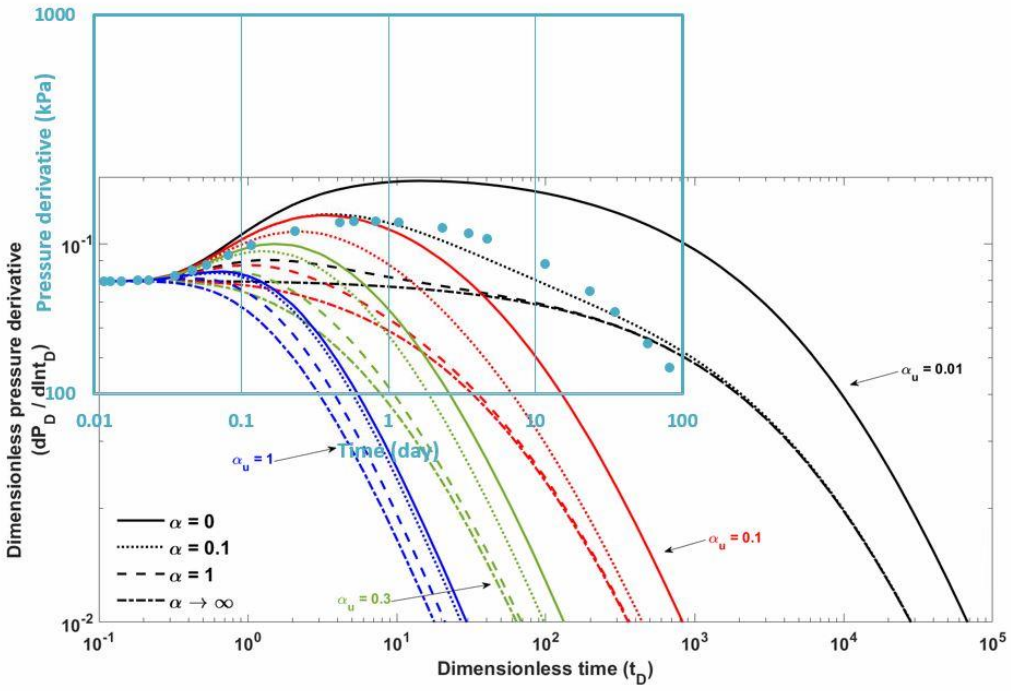

Fig. 3.11. Estimation of α and α_u with the base type curves for example 2

Next, the optimization method is used to find the accurate values of the dimensionless parameters. We set the initial values of T_D and η_D equal to one. The calculated permeability and

fault-well distance (k and a) are used to convert the well pressure data to dimensionless numbers. We apply optimization function to find the best match between the dimensionless pressure data and the analytical solution by modifying the four dimensionless parameters. Using the optimization method, the estimated values of the dimensionless parameters are α=0.5, α_u=0.02, T_D=0.1 and η_D=0.29. The estimated values of fault conductivities (α and α_u) are true values corresponding to synthetic data. Generally, the effects of fault conductivities on the pressure derivative are more than the effect of diffusivity and flow capacity ratios.

3.3. Anisotropic fault leakage

The anisotropic nature of fault permeability is necessary to be honored when modeling flow through faults. The fault permeability can be categorized into three different permeabilities: across-fault, along-fault, and up-fault. Along-fault permeability is generally orders of magnitude larger than the across-fault permeability.

3.3.1. Introduction

Fault core properties affect the across-fault permeability. While, the along-fault permeability mainly depends on the fault damage zone properties (IEAGHG, 2016). Across-fault permeability is determined by the degree of juxtaposition accommodated by displacement as well as fault core flow resistance. If the sand interval is juxtaposed against a shale interval the across-fault permeability will be negligible. If not, the fault flow resistance is traditionally evaluated using the shale smear factor (Lindsay, Murphy, & Walsh) or shale gouge ratio (Yielding, Freeman, & Needham, 1997). Along-fault permeability is primarily governed by the host zone properties. If shale is the host zone, the along-fault permeability may be higher than the host zone. In sand host zones the permeability of the damage zone may be higher or lower depending upon the nature of process and deformations. Up-fault permeability is governed by same parameters controlling the

damage zone along-fault permeability. In addition, compaction can decrease the permeability further making the ratio of up-fault to along-fault permeabilities less than 1. The up-fault permeability is also affected by the orientation of effective stress acting on the fault and its magnitude. The possible range for permeability across the fault is between 10^{-19} to 10^{-14} m^2 compared to 10^{-15} to 10^{-12} m^2 for along-fault permeability (Manzocchi, Childs, & Walsh, 2010). Setting a lower limit to the up-fault permeability can be difficult because there may negligible vertical leakage potential through the fault.

In this section, we introduce an analytical solution which accounts for fault's anisotropic nature considering distinct across-, along-, and up-fault transmissibilities. The model enables evaluation of pressure response in the injection zone and above zone on both sides of the fault. In the following, the physical model is presented first. Next, the analytical model is set up for the physical model configuration by writing the relevant governing equations and corresponding initial and boundary conditions. Next, the analytical solution is derived through applying the combined Laplace and Fourier integral transforms. Then, the analytical solution is validated by comparing its results to those obtained through the numerical simulation. Type curves are provided in terms fault conductivities to demonstrate the ability of the solution for fault leakage characterization. The type curves are next utilized to characterize fault leakage for an example problem.

3.3.2. Physical model description

Fig. 3.12a shows the schematic representation of the faulted system. We consider horizontal flow across and along the fault plane as well as vertical leakage to the shallower formation. The fault divides each layer into two regions (region 1 and region 2). The injection well is located in region 1. The fault consists of four regions (*f1*, *f2*, *fa1*, *fa2*) that conduct fluid in three directions (*x, y,* and *z* directions). Fig 3.12b illustrates hydraulic connections between the fault

regions as well as the reservoirs' regions. Each region of the fault zone is in direct hydraulic connection with the adjacent region of injection/above zones (regions 1, 2, a1, and a2). q is the injection rate and μ is fluid viscosity. k_{fx}, k_{fy} and k_{fz} are fault permeabilities in three directions. k and h are permeability and thickness of region 1 of the injection zone. Due to fault displacement, diffusivity and thickness of regions 2, *a1*, and *a2* can be different from region 1. k_j and h_j are permeability and thickness of the altered zones (j=2, *a1*, and *a2*).

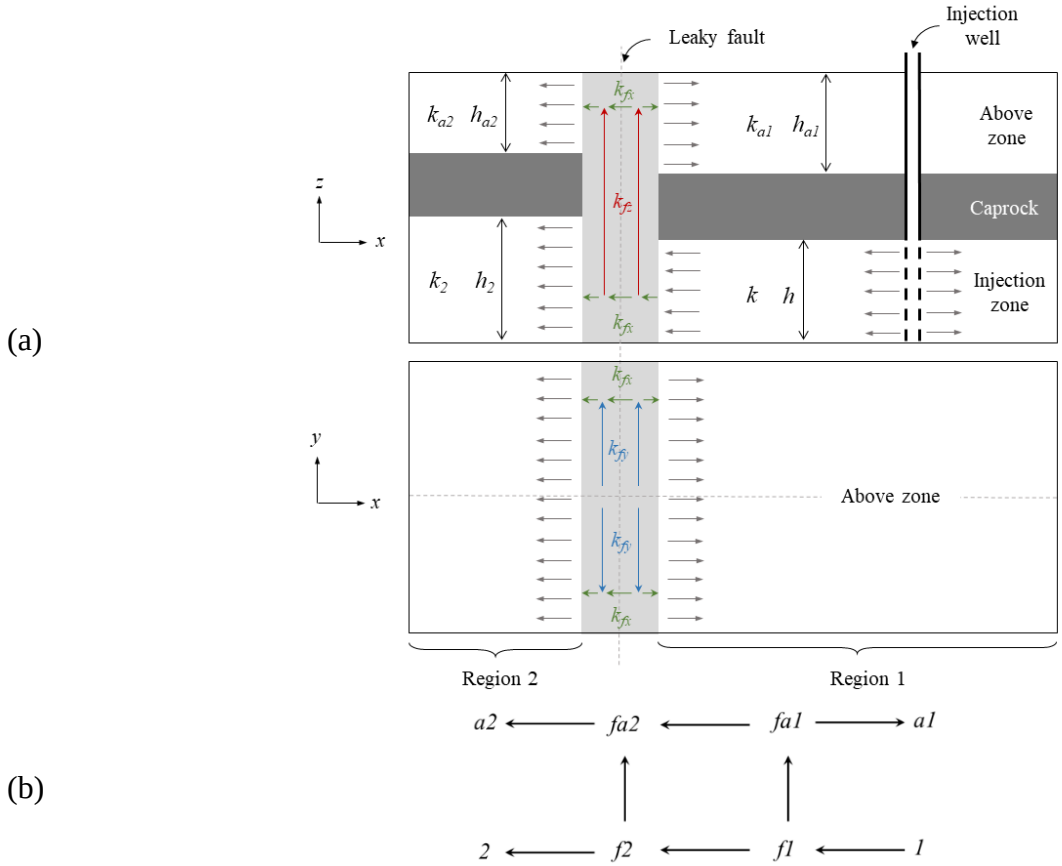

Fig. 3.12. (a) Schematic representation of the physical model, (b) Directions of intra-fault and fault-reservoirs hydraulic connections on x-z coordinate

3.3.3. Analytical model

In this section, we derive an analytical solution of pressure variations in the system of the injection zone and above zone connected by the fault zone. The fault zone pressure variations are

important as it conducts the flow into the far distance in the reservoir. The fault is fed from the injection zone due to pressure gradients associated with injection operations on the side of the injection well. The pressure diffusivity equations are written for all regions in the injection zone and the above zone. The injection well is considered in region 1 introducing Dirac delta function (δ) in the corresponding diffusivity equation (Eq. 3.27). The governing diffusivity equations for the four regions of the injection zone (regions 1 and 2) and above zone (regions *a1* and *a2*) are shown below.

Injection zone:

$$\frac{\partial^2 \Delta p_1}{\partial x^2} + \frac{\partial^2 \Delta p_1}{\partial y^2} + \frac{q\mu}{kh}\delta(x-a)\delta(y) = \frac{1}{\eta}\frac{\partial \Delta p_1}{\partial t} \tag{3.27}$$

$$\frac{\partial^2 \Delta p_2}{\partial x^2} + \frac{\partial^2 \Delta p_2}{\partial y^2} = \frac{1}{\eta_2}\frac{\partial \Delta p_2}{\partial t} \tag{3.28}$$

Above zone:

$$\frac{\partial^2 \Delta p_{a1}}{\partial x^2} + \frac{\partial^2 \Delta p_{a1}}{\partial y^2} = \frac{1}{\eta_{a1}}\frac{\partial \Delta p_{a1}}{\partial t} \tag{3.29}$$

$$\frac{\partial^2 \Delta p_{a2}}{\partial x^2} + \frac{\partial^2 \Delta p_{a2}}{\partial y^2} = \frac{1}{\eta_{a2}}\frac{\partial \Delta p_{a2}}{\partial t} \tag{3.30}$$

where $\Delta p_j = p_0 - p_j$. p_j denotes the pressure of region j (j= 1, 2, $a1$, $a2$) and p_0 is the initial pressure of the system. The diffusivity coefficient of region j of the reservoirs is defined as below (j= *1, 2, a1, a2*).

$$\eta_j = \frac{k_j}{\phi\mu c_t} \tag{3.31}$$

The fault zone is divided into the four zones. Each zone of the fault is in the vicinity of the corresponding region of the injection zone (regions 1 and 2) or the above zone (regions a1 and a2) (Fig. 3.12b). The pressure diffusion inside the fault at region f1 is given by:

$$\frac{\partial^2 \Delta p_{f1}}{\partial y^2} + \frac{k}{k_{fy} w_f / 2} \frac{\partial \Delta p_1(t,0,y)}{\partial x} - \frac{k_{fx}}{k_{fy} w_f / 2} \frac{\Delta p_{f1} - \Delta p_{f2}}{w_f / 2} - \frac{k_{fz}}{k_{fy} L / 2} \frac{\Delta p_{f1} - \Delta p_{fa1}}{L} = \frac{1}{\eta_f} \frac{\partial \Delta p_{f1}}{\partial t} \tag{3.32}$$

where η_f and w_f are diffusivity coefficient of the fault zone and fault width. The first term on the left-hand-side (LHS) of Equation (3.33) is the pressure diffusivity along the fault and the right-hand-side (RHS) term is the accumulation term. The flow to/from region *f1* to regions 1, *f2*, and fa1 are given by the second, third, and forth terms on the LHS respectively. Similarly, for regions *f*2, *fa*1, and *fa*2 we can write, respectively:

$$\frac{\partial^2 \Delta p_{f2}}{\partial y^2} - \frac{k_2}{k_{fy} w_f / 2} \frac{\partial \Delta p_2(t,0,y)}{\partial x} + \frac{k_{fx}}{k_{fy} w_f / 2} \frac{\Delta p_{f1} - \Delta p_{f2}}{w_f / 2} - \frac{k_{fz}}{k_{fy} L_2 / 2} \frac{\Delta p_{f2} - \Delta p_{fa2}}{L_2} = \frac{1}{\eta_f} \frac{\partial \Delta p_{f2}}{\partial t} \tag{3.33}$$

$$\frac{\partial^2 \Delta p_{fa1}}{\partial y^2} - \frac{k_{a1}}{k_{fy} w_f / 2} \frac{-\partial \Delta p_{a1}(t,0,y)}{\partial x} - \frac{k_{fx}}{k_{fy} w_f / 2} \frac{\Delta p_{fa1} - \Delta p_{fa2}}{w_f / 2} + \frac{k_{fz}}{k_{fy} L / 2} \frac{\Delta p_{f1} - \Delta p_{fa1}}{L} = \frac{1}{\eta_f} \frac{\partial \Delta p_{fa1}}{\partial t} \tag{3.34}$$

$$\frac{\partial^2 \Delta p_{fa2}}{\partial y^2} - \frac{k_{a2}}{k_{fy} w_f / 2} \frac{\partial \Delta p_{a2}(t,0,y)}{\partial x} + \frac{k_{fx}}{k_{fy} w_f / 2} \frac{\Delta p_{fa1} - \Delta p_{fa2}}{w_f / 2} + \frac{k_{fz}}{k_{fy} L_2 / 2} \frac{\Delta p_{f2} - \Delta p_{fa2}}{L_2} = \frac{1}{\eta_f} \frac{\partial \Delta p_{fa2}}{\partial t} \tag{3.35}$$

The third term in LHS of Equations (3.32)-(3.35) include k_{fx} that make the core zone permeability different from that of the damaged zone to fully honor the anisotropic fault structure. Next, we need to define initial and boundary conditions in order to solve the system of partial differential equations. We consider the initial uniform pressure (p_0) is the system (Equation 3.36).

$$\begin{aligned} &p_1(0,x,y) = p_2(0,x,y) = p_{a1}(0,x,y) = p_{a2}(0,x,y) = p_{f1}(0,y) = p_{f2}(0,y) = p_{fa1}(0,y) \\ &= p_{fa2}(0,y) = p_0 \end{aligned} \tag{3.36}$$

The whole system is assumed infinite acting in horizontal directions (Equation 3.37).

$$\begin{aligned} &p_1(t, x \to \infty, y) = p_2(t, x \to -\infty, y) = p_{a1}(t, x \to \infty, y) = p_{a2}(t, x \to -\infty, y) \\ &= p_1(t, x, y \to \pm\infty) = p_2(t, x, y \to \pm\infty) = p_{a1}(t, x, y \to \pm\infty) = p_{a2}(t, x, y \to \pm\infty) \\ &= p_{f1}(t, y \to \pm\infty) = p_{f2}(t, y \to \pm\infty) = p_{fa1}(t, y \to \pm\infty) = p_{fa2}(t, y \to \pm\infty) = p_0 \end{aligned} \tag{3.37}$$

Equations (3.38)-(3.41) are boundary conditions that describe the hydraulic connections between the fault and the reservoir regions 1, 2, *a*1, and *a*2 respectively.

$$\frac{kh}{\mu}\frac{\partial \Delta p_1(t,0,y)}{\partial x} = \frac{kh}{\mu w_f / 4}\left(\Delta p_1(t,0,y) - \Delta p_{f1}(t,y)\right) \tag{3.38}$$

$$\frac{k_2 h_2}{\mu}\frac{\partial \Delta p_2(t,0,y)}{\partial x} = \frac{kh_2}{\mu w_f / 4}\left(\Delta p_{f2}(t,y) - \Delta p_2(t,0,y)\right) \tag{3.39}$$

$$-\frac{k_{a1} h_{a1}}{\mu}\frac{\partial \Delta p_{a1}(t,0,y)}{\partial x} = \frac{kh_{a1}}{\mu w_f / 4}\left(\Delta p_{fa1}(t,y) - \Delta p_{a1}(t,0,y)\right) \tag{3.40}$$

$$\frac{k_{a2} h_{a2}}{\mu}\frac{\partial \Delta p_{a2}(t,0,y)}{\partial x} = \frac{kh_{a2}}{\mu w_f / 4}\left(\Delta p_{fa2}(t,y) - \Delta p_{a2}(t,0,y)\right) \tag{3.41}$$

The dimensionless groups are defined below:

$$p_{Dj} = \frac{kh}{q\mu}\Delta p_j \quad (\text{for } j= 2, a1, a2, f1, f2, fa1, fa2), \quad t_D = \frac{\eta t}{a^2}$$

$$\alpha_x = \frac{4k_{fx}a}{kw_f} \ , \ \alpha_y = \frac{k_{fy}w_f}{2ka} \ , \ \alpha_z = \frac{k_{fz}aw_f}{kL^2} \ , \ \eta_{Dj} = \frac{\eta_j}{\eta} \ (\text{for } j= 2, a1, a2, f), \tag{3.42}$$

$$h_{Dj} = \frac{h_j}{h}, \ T_{Dj} = \frac{k_j h_j}{kh} \quad (\text{for } j= 2, a1, a2), \ L_D = \frac{L_2}{L}, \ w_{fD} = \frac{w_f}{L}$$

where L is the leakage interval, which is the vertical distance between the middle height of the injection zone and middle height of the above zone (L is identical for regions 1 and 2). In order to simplify the system of partial differential equations to the ordinary system of differential equations, we apply Laplace ($\mathcal{L}$) and Fourier ($\mathcal{F}$) transforms on time and y-direction variables (Equations (3.43)-(3.44)).

$$\overline{\Delta p}(x,y,s) = \mathcal{L}\left[\Delta p(x,y,t)\right] = \int_0^\infty \Delta p(x,y,t)e^{-st}dt \tag{3.43}$$

$$\overline{\overline{\Delta p}}(x,\omega,s) = \mathcal{F}\left[\overline{\Delta p}(x,y,s)\right] = \int_{-\infty}^{+\infty} \overline{\Delta p}(x,y,s)e^{i\omega y}dy \tag{3.44}$$

ω and s are Fourier and Laplace Variables, respectively. The bar and = signs denoted the Laplace and Laplace-Fourier domains, respectively. The solution for pressure variations of the system in the Laplace-Fourier domain is shown below.

$$\bar{\bar{p}}_{D1} = \frac{1}{2sA}\left(e^{-|x_D-1|A}\right) + C_1 e^{-Ax_D} \tag{3.45}$$

$$\bar{\bar{p}}_{D2} = C_2 e^{A_2 x_D} \tag{3.46}$$

$$\bar{\bar{p}}_{Da1} = C_3 e^{-A_{a1} x_D} \tag{3.47}$$

$$\bar{\bar{p}}_{Da2} = C_4 e^{A_{a2} x_D} \tag{3.48}$$

where:

$$A^2 = 4\pi^2\omega^2 + s,\ A_2{}^2 = 4\pi^2\omega^2 + \frac{s}{\eta_{D2}},\ A_{a1}{}^2 = 4\pi^2\omega^2 + \frac{s}{\eta_{Da1}},\ A_{a2}{}^2 = 4\pi^2\omega^2 + \frac{s}{\eta_{Da2}}$$

$$A_f{}^2 = 4\pi^2\omega^2 + \frac{s}{\eta_{Df}} \tag{3.49}$$

Combining Equations (3.45)-(3.48) with the boundary conditions (Equations 3.38-3.41), the coefficients C_1 through C_4 are calculated by solving the following system of linear algebraic equations for the coefficient vector C.

$$\boldsymbol{H}.C = F \tag{3.50}$$

where:

$$H = \begin{bmatrix} 0 & \alpha_z\left(1+\frac{A_2 T_{D2}}{\alpha_x h_{D2}}\right) & \frac{\alpha_x}{2\alpha_y}\left(1+\frac{A_{a1} T_{Da1}}{\alpha_x h_{Da1}}\right) & -\frac{A_{a2}}{\alpha_y} - \left(A_f{}^2 + \frac{\alpha_x}{2\alpha_y} + \alpha_z\right)\left(1+\frac{A_{a2} T_{Da2}}{\alpha_x h_{Da2}}\right) \\ \alpha_z\left(1+\frac{A}{\alpha_x}\right) & 0 & -\frac{A_{a1}}{\alpha_y} - \left(A_f{}^2 + \frac{\alpha_x}{2\alpha_y} + \alpha_z\right)\left(1+\frac{A_{a1} T_{Da1}}{\alpha_x h_{Da1}}\right) & \frac{\alpha_x}{2\alpha_y}\left(1+\frac{A_{a2} T_{Da2}}{\alpha_x h_{Da2}}\right) \\ \frac{\alpha_x + A}{2\alpha_y}\left(1+\frac{A}{\alpha_x}\right) & -\frac{A_2}{\alpha_y} - \left(A_f{}^2 + \frac{\alpha_x}{2\alpha_y} + \alpha_z\right)\left(1+\frac{A_2 T_{D2}}{\alpha_x h_{D2}}\right) & 0 & \alpha_z\left(1+\frac{A_{a2} T_{Da2}}{\alpha_x h_{Da2}}\right) \\ -\frac{A}{\alpha_y} - \left(A_f{}^2 + \frac{\alpha_x}{2\alpha_y} + \alpha_z\right)\left(1+\frac{A}{\alpha_x}\right) & \frac{\alpha_x}{2\alpha_y}\left(1+\frac{A_2 T_{D2}}{\alpha_x h_{D2}}\right) & \alpha_z\left(1+\frac{A_{a1} T_{Da1}}{\alpha_x h_{Da1}}\right) & 0 \end{bmatrix} \tag{3.51}$$

$$F^T = \begin{bmatrix} 0 & -\frac{e^{-A}}{2s}\alpha_z\left(\frac{1}{A}-\frac{1}{\alpha_x}\right) & -\frac{e^{-A}}{2s}\frac{\alpha_x}{2\alpha_y}\left(\frac{1}{A}-\frac{1}{\alpha_x}\right) & \frac{e^{-A}}{2s}\left(\frac{1}{\alpha_y} + \left(A_f{}^2 + \frac{\alpha_x}{2\alpha_y} + \alpha_z\right)\left(\frac{1}{A}-\frac{1}{\alpha_x}\right)\right) \end{bmatrix} \tag{3.52}$$

$$C^T = \begin{bmatrix} C_1 & C_2 & C_3 & C_4 \end{bmatrix} \tag{3.53}$$

The superscript *T* indicated the vector transpose. The details of the solution derivation are explained in the Appendix 3. We apply numerical Laplace inversion (Stehfest, 1970) and numerical Fourier inversion to obtain the solution in the time–space domain.

3.3.4. Validation

In this section, we validate the analytical solution of the anisotropic fault system with the numerical simulation using the CMG-IMEX (CMG, 2015). The simulated system is large enough to keep the infinite acting behavior during the test. Local grid refinement has been used near the wellbore as well as the fault. Fig. 3.13 a shows the CMG physical model from top view. Fig. 3.13 b demonstrates top view of the well and fault locations in the injection zone and the local grid refinement near the wellbore as well as near the fault. The total number of grids are 1080000 (n_x=600, n_y=600, n_z=3) and the duration of the simulation is two hours for one-minute time step. Fig. 3.13c shows the pressure profile in the injection zone which shows good agreement between the analytical solution and the numerical results. The pressure discontinuity is obvious across the fault. Table 3.2 shows the values of the system properties. The rock and fluid properties are assumed identical in the four regions of the injection and above zones.

Table 3.2. Values of the system properties

Parameter	Value	Parameter	Value
k_{fx} (m^2)	10^{-14}	k_{a2} (m^2)	10^{-14}
k_{fy} (m^2)	10^{-11}	L_1 (m)	25
k_{fz} (m^2)	10^{-13}	L_2 (m)	25
w_f (m)	1	h (m)	20
a (m)	100	h_2 (m)	20
ϕ	0.1	h_{a1} (m)	20
c_t (1/Pa)	10^{-9}	h_{a2} (m)	20
k (m^2)	10^{-14}	q (m^3/s)	0.01
k_2 (m^2)	10^{-14}	μ (Pa.s)	0.0005
k_{a1} (m^2)	10^{-14}		

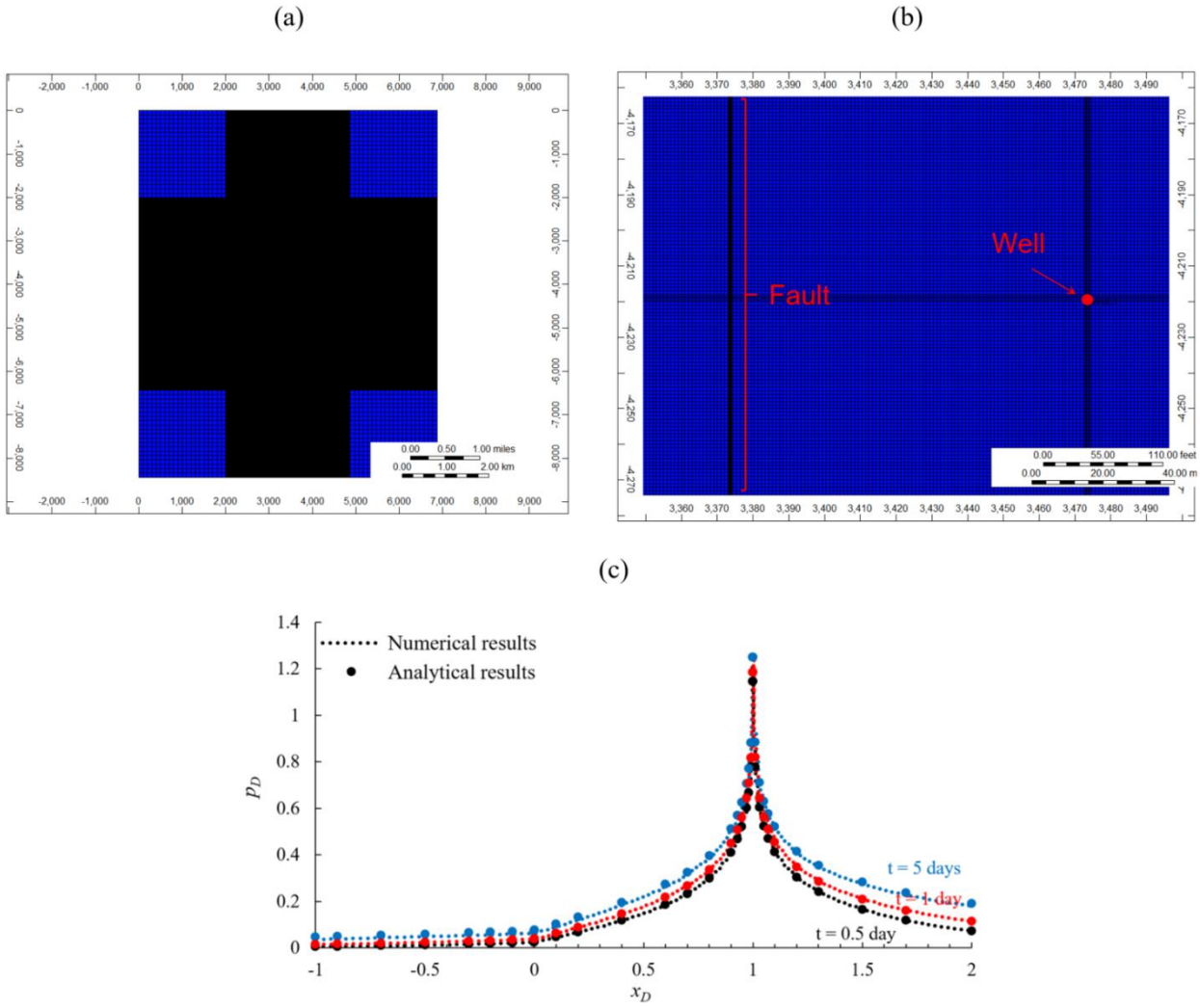

Fig. 3.13. (a) Physical model on x-y coordinate for the numerical simulator, (b) Location of well and fault in the injection zone on x-y coordinate for the numerical simulator, (c) Comparison of the analytical (dots) versus numerical (lines) pressure distribution in the injection zone at different times

In addition to the pressure profile, we validate the pressure derivative as the pressure derivative is required for leakage characterization. Figs. 3.14 illustrates good agreements between analytical and numerical results.

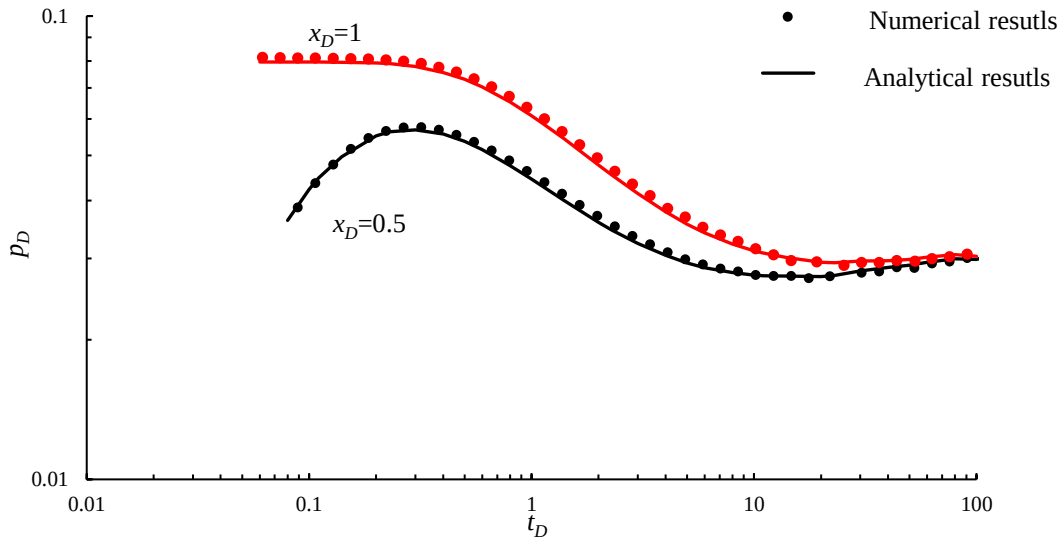

Fig. 3.14. Injection-zone pressure derivative validation.

3.3.5. Results and discussion

In this section, we show the ability of the analytical solution for leaky fault characterization by providing type curves based on the derivative curves. Next, we apply the type curves to an example problem for anisotropic leaky fault characterization.

Effect of fault conductivities on the pressure response

We show the effect of fault conductivities (α_x, α_y, α_z) on the pressure derivative at the active well. Figs. 3.15-3.17 show the effect of α_x, α_y, and α_z respectively on the injection well's pressure derivative. Considering the definition of the dimensionless pressure, the 0.08 (=1/4π) is the value of the derivative for the early-time radial flow.

Fig. 3.15 shows the effect of α_x on the derivative curves while α_y= α_z= 1. α_x = 0 illustrates the same derivative horizontal line (derivative= 0.08) after the early time radial flow, which indicates that the fault acts as a partially sealing fault. The derivative did not drop because the vertically-leaking fault exposes the semi-infinite injection zone to another semi-infinite reservoir volume of the region 1 of the above zone. For α_x > 0, the derivative curves would ultimately reach

0.04 at the late time, which is half of the early time radial derivative. This value is a sign of the vertical hydraulic connection in the fault zone which indicates fault leakage in x-, y-, and z-directions simultaneously. It can be inferred form Fig. 3.15 that the late time radial flow (derivative = 0.04) would be delayed by decreasing α_x.

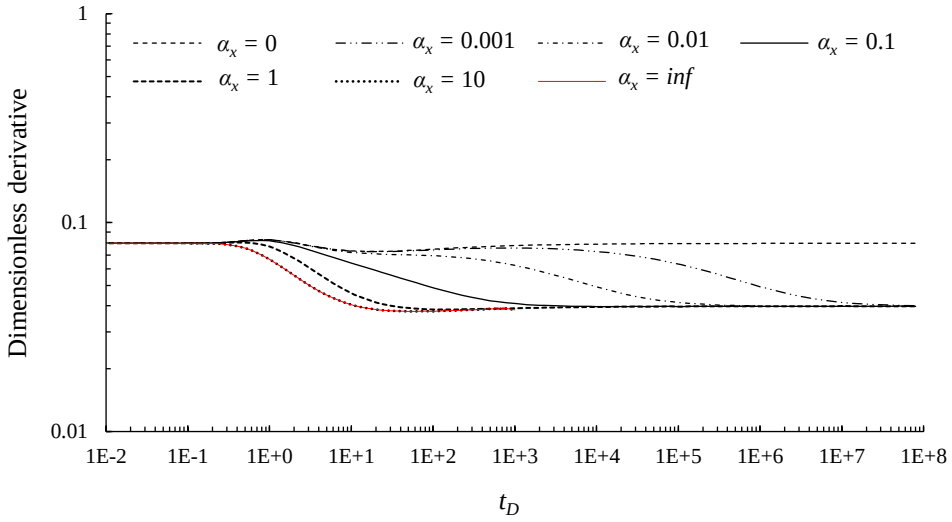

Fig. 3.15. Effect of α_x on pressure derivative (α_y=1, α_z=1, η_{fD}=1000, η_{fD}=1000, w_{fD}=0.001, L_D=1)

Fig. 3.16 shows the impact of α_y on the injection well's pressure derivative while α_x=0.1 and α_z= 1. It is evident that the derivative curves reach a valley after the early-time radial flow. The valley would become deeper by increasing the along-fault conductivity α_y. Also, increasing α_y delays the arrival of late-time 0.04 derivative value.

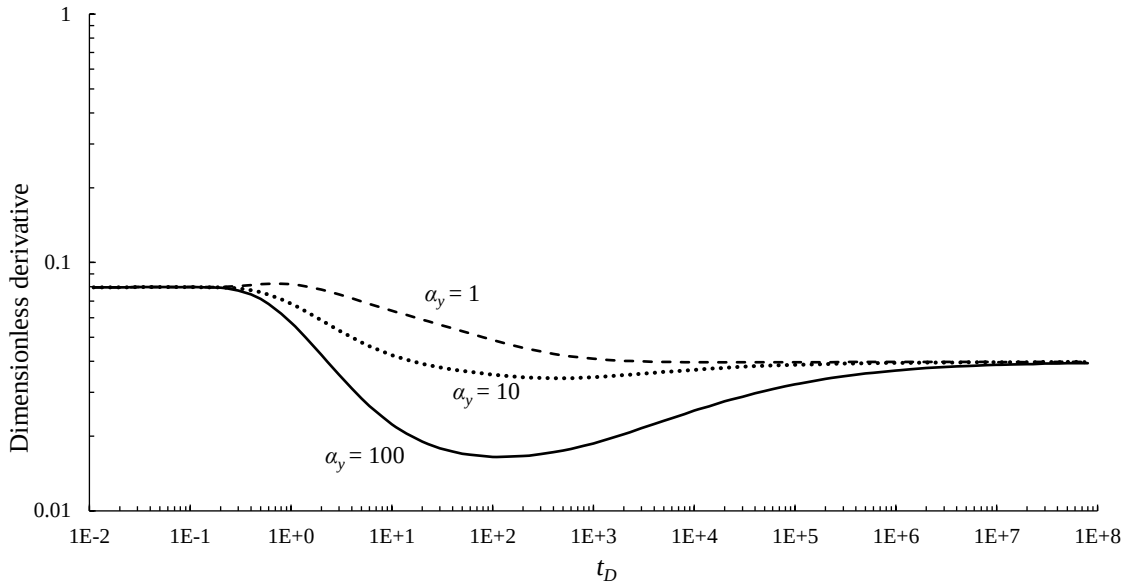

Fig. 3.16. Effect of α_y on pressure derivative (α_x = 0.1, α_z = 1, η_{fD}=1000, w_{fD}=0.001)

Fig. 3.17 shows the effect of vertical conductivity of the fault az on the pressure derivative curves for fixed α_x=0.1 and α_y=1. The late time derivative value is equal to its early-time for vertically sealing fault (α_z=0). However, it is half of the early-time value for vertically leaking fault ($\alpha_z > 0$).

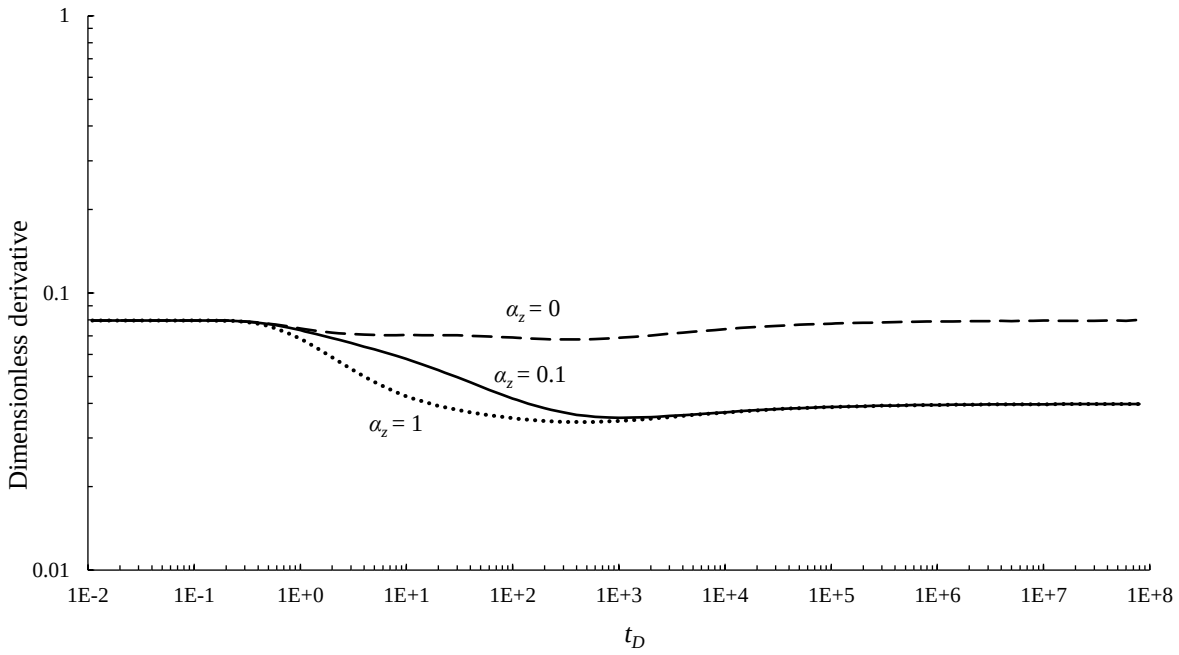

Fig. 3.17. Effect of α_z on pressure derivative (α_x=0.1, α_y=10, η_{fD}=1000, w_{fD}=0.001)

Fault leakage characterization

Fig. 3.18 shows the type curves of the combined effects of α_x, α_y, and α_z on the derivative curves. The leaky fault type curves are classified into three main categories. The first category is the sealing fault that shows the doubled derivative compared to the early time radial flow (derivative=0.16, the blue curve in Fig. 3.18). The second category is the partially-sealing fault (black curves in Fig. 3.18) that are conductive only across the fault ($\alpha_x = 0$, $\alpha_z \neq 0$) or upward ($\alpha_x \neq 0$, $\alpha_z = 0$). In this category, the late time derivative value equals the early-time radial flow value (=0.08). The third category of type curves show the derivative curves of leaky faults (red curves in Fig. 3.18) that are conductive both across the fault and upward. In this category, the late time radial flow derivative is half of the early time derivative (derivative= 0.04). We do not show the values of fault conductivities in Fig. 3.18 for brevity and to assist the reader to focus on the three main categories (shown by blue, black, and red curves).

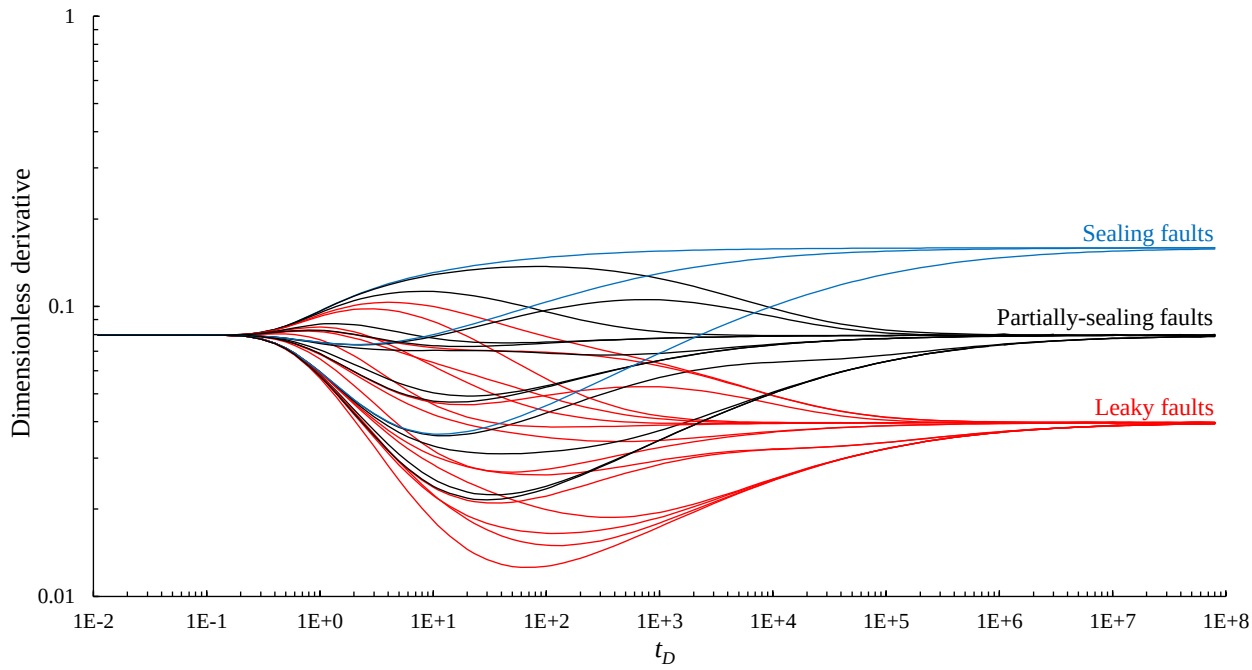

Fig. 3.18. Type curves for anisotropic fault characterization applying pressure derivative of the injection well ($\eta_{D2} = \eta_{Da1} = \eta_{Da2} = 1$, $\eta_{Df} = 1000$, $w_{fD}=0.001$, $L_D=1$).

In order to differentiate the type curve groups based on the variations of α_x, α_y, and α_z, we show the three categories of type curves in separate curves. Fig. 3.19 shows the type curves of sealing faults that confine the fluid flow inside region 1 of the injection zone.

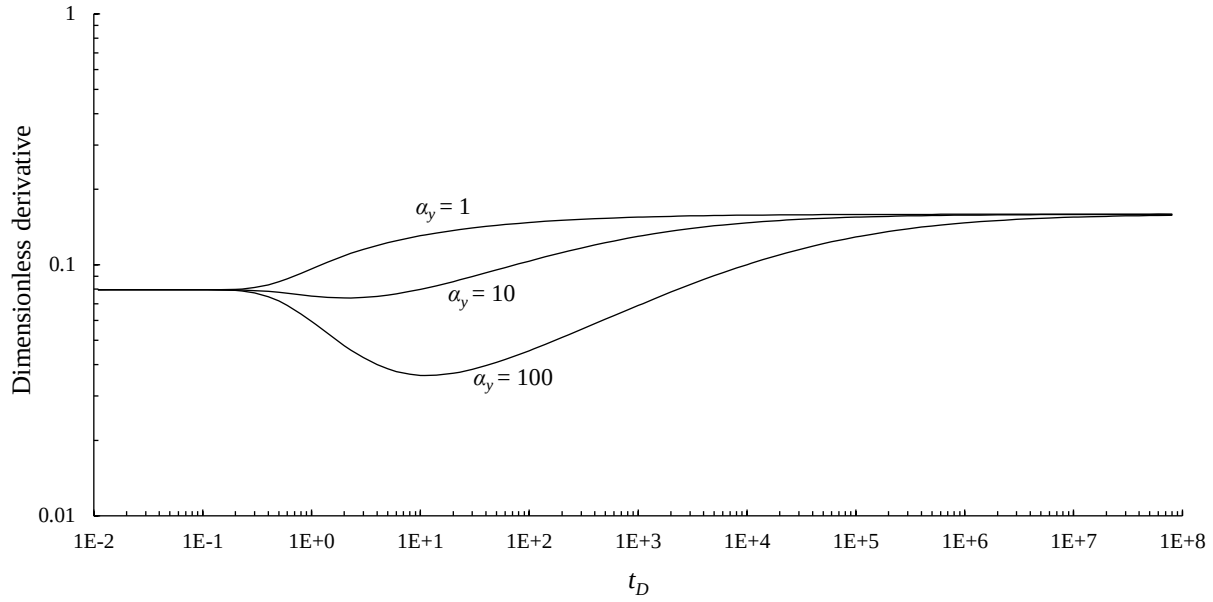

Fig. 3.19. Type curves for faults that are sealing upward and across the fault ($\eta_{D2} = \eta_{Da1} = \eta_{Da2} = 1$, $\eta_{Df} = 1000$, $w_{fD} = 0.001$, $L_D = 1$).

Fig. 3.20 shows type curves of partially sealing faults that conduct fluid across or up the fault. Either of these conductivities results in the same late time derivative representative of radial flow. Considering this similar response, it may be difficult to distinguish between these two types of partially sealing faults by the injection zone pressure response alone especially if data is noisy.

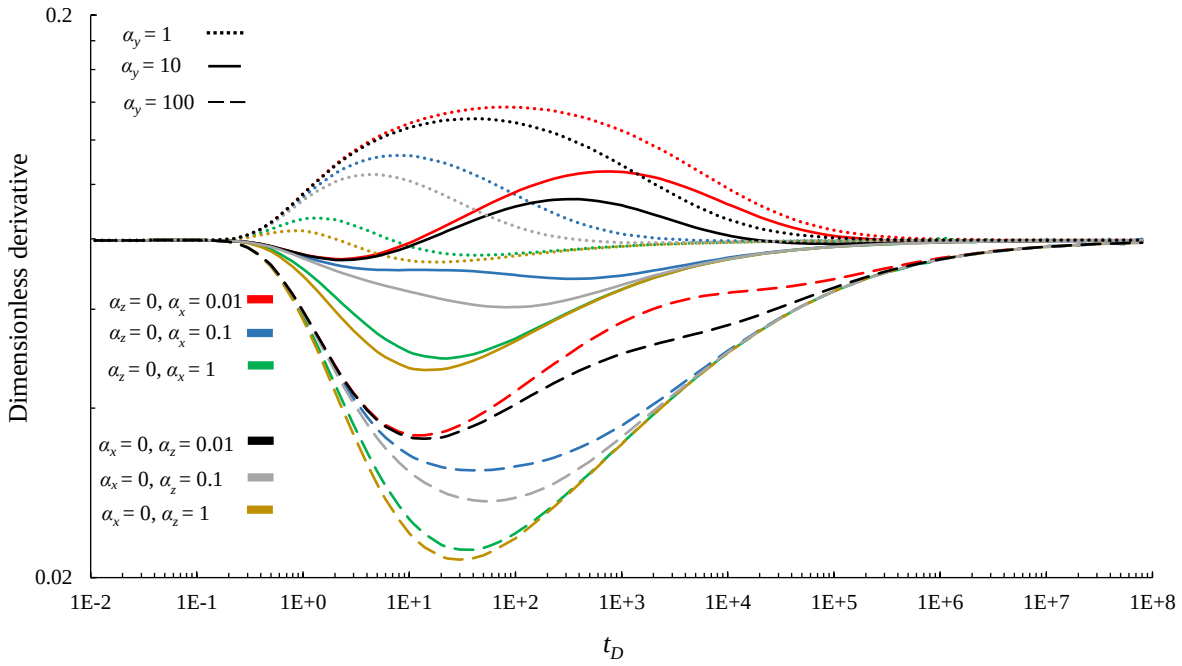

Fig. 3.20. Type curves for Partially-sealing faults ($\eta_{D2} = \eta_{Da1} = \eta_{Da2} = 1$, $\eta_{Df} = 1000$, $w_{fD} = 0.001$, $L_D = 1$).

Fig. 3.21 illustrates the type curves of leaky faults that conduct fluid into the other side of the fault as well as the above zone. As explained before, the most important sign of a leaky fault is the late–time value of derivative ($1/8\pi$), which is half of the early-time radial flow before the leakage response.

Figs. 18-21 show that the type curves with the same values of α_y would merge at early-time of fault leakage response. In addition, Fig. 3.21 shows that the curves with the same values of α_x and α_y merge at late-time before the late-time radial flow response.

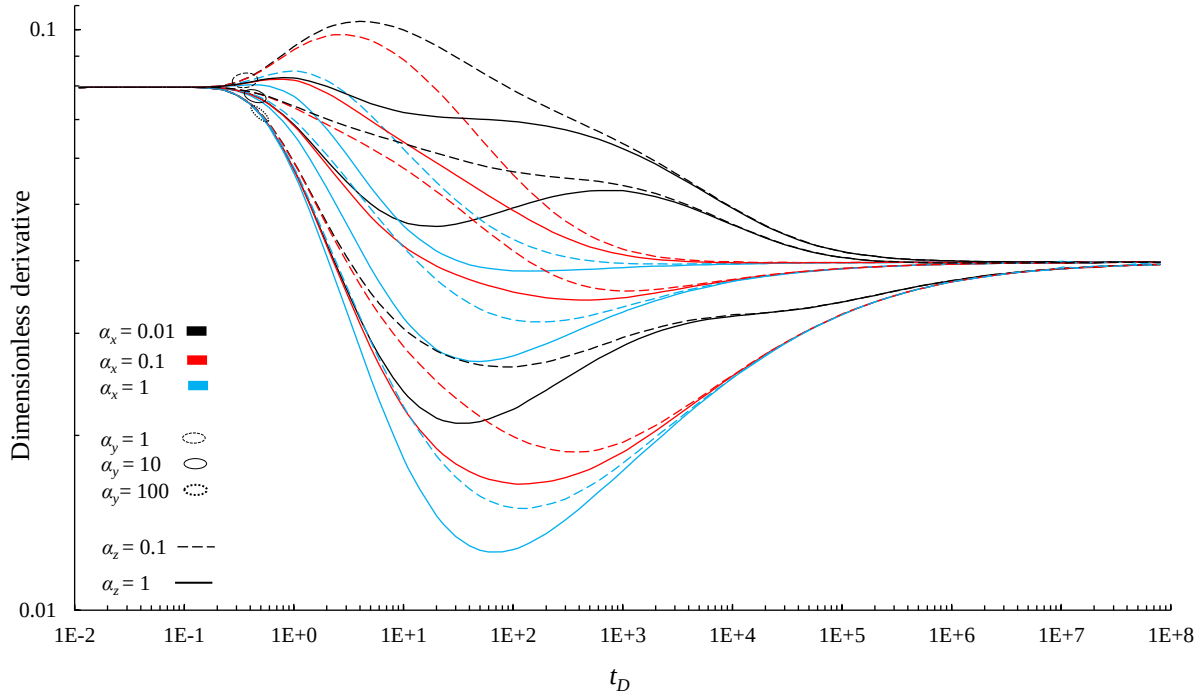

Fig.3.21. Type curves for Leaky faults ($\eta_{D2} = \eta_{Da1} = \eta_{Da2}$ =1, η_{Df} =1000, w_{fD}=0.001, L_D=1).

It can be inferred from Figs. 3.18-3.21 that fault conductivities (α_x, α_y, and α_z) can be estimated by the pressure derivative type curves. The pressure derivative curves derived by the analytical solution are unique for each combination of fault conductivities (α_x, α_y, and α_z). Therefore, the unique values of α_x, α_y, and α_z can be estimated by the pressure variations applying the analytical solution. For all types of faults, the first thing that occur after the early-time radial flow is the effect of α_y that typically appear by a valley. The valley would become deeper by increasing the value of α_y. For small values of α_y, the valley would alter to a hump that would be bigger as α_y got smaller values. For sealing fault, α_y can easily be estimated as it is the only unknown conductivity (Fig. 3.18). For non-sealing faults (Figs. 3.19-3.20), α_y can be estimated by early-time merge of the derivative curves.

After estimation of α_y, we explain the estimation of α_x and α_z. As explained before, for partially sealing fault, it is difficult to distinguish between the across fault and vertical leakage

based on the active well pressure response (Fig. 3.19). However, if we know the types of the partially sealing fault ($\alpha_x = 0$ or $\alpha_z = 0$), the type curves of Fig. 3.19 are useful to estimate the other nonzero across fault conductivity (α_x) or vertical conductivity (α_z), applying the middle-time derivative effect.

In spite of the partially sealing faults, α_x and α_z can be distinguishable if significant across-fault and vertical leakage occur through a leaky fault. For leaky faults (Fig. 3.21), α_x can be estimated by the late-time merge before the late-time radial flow. α_z can also be estimated by the middle-time effect after estimation of α_x. In this characterization procedure, the sequential estimation of fault conductivities is vital (α_y by the early-time merge → α_x by the late time merge → α_z by the middle time merge).

Effects of fault displacement

Fault displacement may result in non-identical thickness and diffusivity at two sides of the fault both in the injection zone and the above zone. In order to evaluate the effect of fault displacement, we investigate the effects of transmissibility ratio (T_{Dj}), diffusivity ratio (η_{Dj}), thickness ratio (h_{Dj}), Leakage interval ratio (L_D), and fault thickness (w_{fD}). on the pressure response. Fig. 3.22 shows that the variation of η_{Dj}, h_{Dj}, L_D, and w_{fD} would not affect the estimation of fault conductivities (Base case: $T_{D2} = T_{Da1} = T_{Da2} = \eta_{D2} = \eta_{Da1} = \eta_{Da2} = h_{D2} = h_{Da1} = h_{Da2} = 1$, $\eta_{Df} = 1000$, $\alpha_x = 0.1$, $\alpha y = 1$, $\alpha_z = 0.1$, $L_D = 1$, and $w_{fD} = 0.01$).

(a)

(b)

(c)

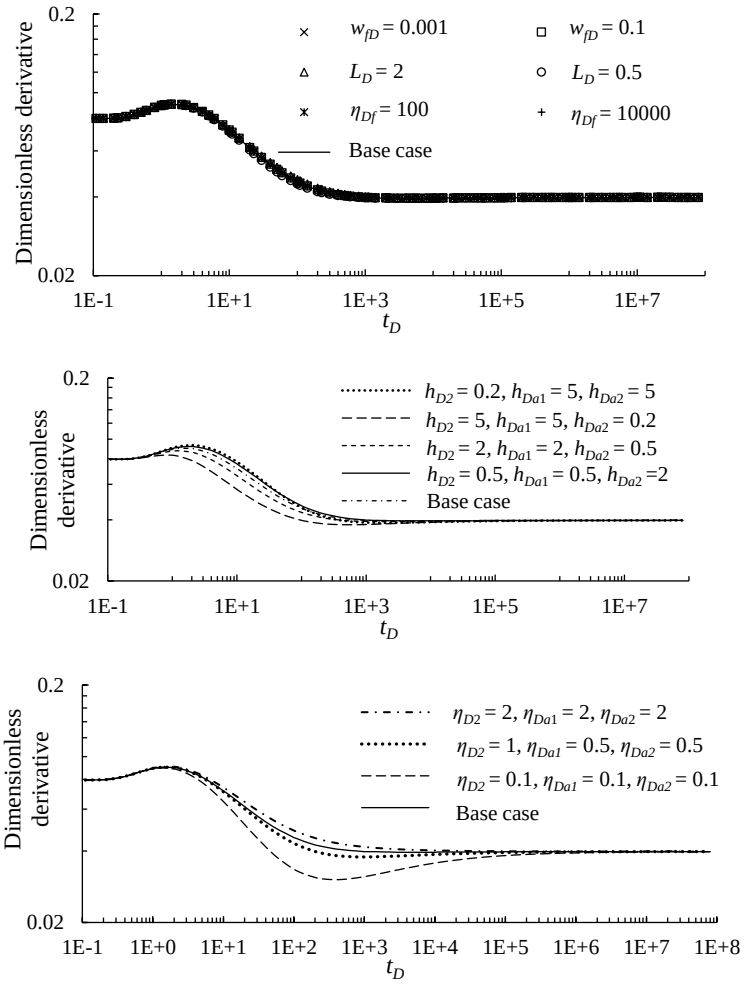

Fig. 3.22. (a) Effect of dimensionless fault width and leakage interval ratio on pressure derivative of injection well, (b) Effect of thickness ratios on pressure derivative of the active well, (c) Effect of diffusivity ratios on pressure derivative of injection well

Leakage rate

After estimation of fault conductivities, we can calculate the leakage rate applying the estimated fault parameters to Equation (28). Fig. 3.23 shows the effect of up-fault conductivity on the leakage rate. The ultimate leakage rate is half of the injection rate, because the fluid flow has been divided between two layers with identical transmissivity ($T_{D2} = T_{Da1} = T_{Da2}$=1).

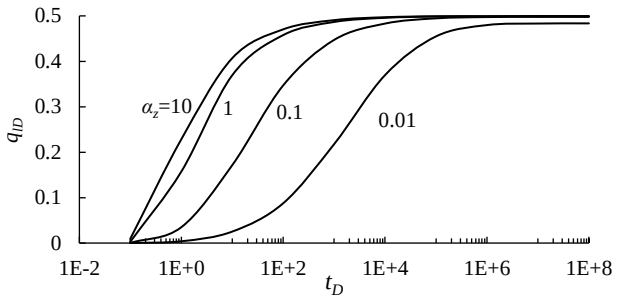

Fig. 3.23. Effect of up-fault conductivity on the leakage rate ($T_{D2} = T_{Da1} = T_{Da2} = \eta_{D2} = \eta_{Da1} = \eta_{Da2} = h_{D2} = h_{Da1} = h_{Da2} = 1$, $\eta_{Df} = 1000$, $w_{fD} = 0.01$, $\alpha_x = 1$, $\alpha_y = 1$)

Example problem

In this section, an example problem is provided for fault characterization. Numerical simulation data is given with the following values of the system properties: permeability of the injection zone and the above zone is 10^{-14} m^2. Fault zone permeabilities are $k_{fx}=2.5\times10^{-17}$, $k_{fy}=2\times10^{-11}$, and $k_{fz}=6.25\times10^{-14}$ m^2. Fault-well distance is 20 m, fluid viscosity is 0.0005 Pa.s, and total compressibility is 10^{-9} Pa^{-1}. Therefore, the values of fault conductivities are $\alpha_x=1$, $\alpha_y=10$, and $\alpha_z=1$. Fig. 3.24 shows the type curve matching for the pressure derivative of the injection well. The green curve is the derivative of the injection well pressure data. This match shows $\alpha_x=1$, $\alpha_y=10$, and $\alpha_z=1$ which are equal to the actual values. Although the early-time radial flow is missed in the pressure data, the shape of the derivative curve is clearly distinguishable between the type curves (Fig. 3.24).

Next, we estimate k and a applying a match point between the two curves. We choose an arbitrary match point on the plots that shows $\Delta p'$=2021.6 kPa and t=0.1 day on the pressure data plot and p_D'=0.08 and t_D=0.2 on the type curves. Next, we calculate k and a. The estimated k and a are 9.9×10^{-15} m^2 and a=92.5 m that are close to the actual values.

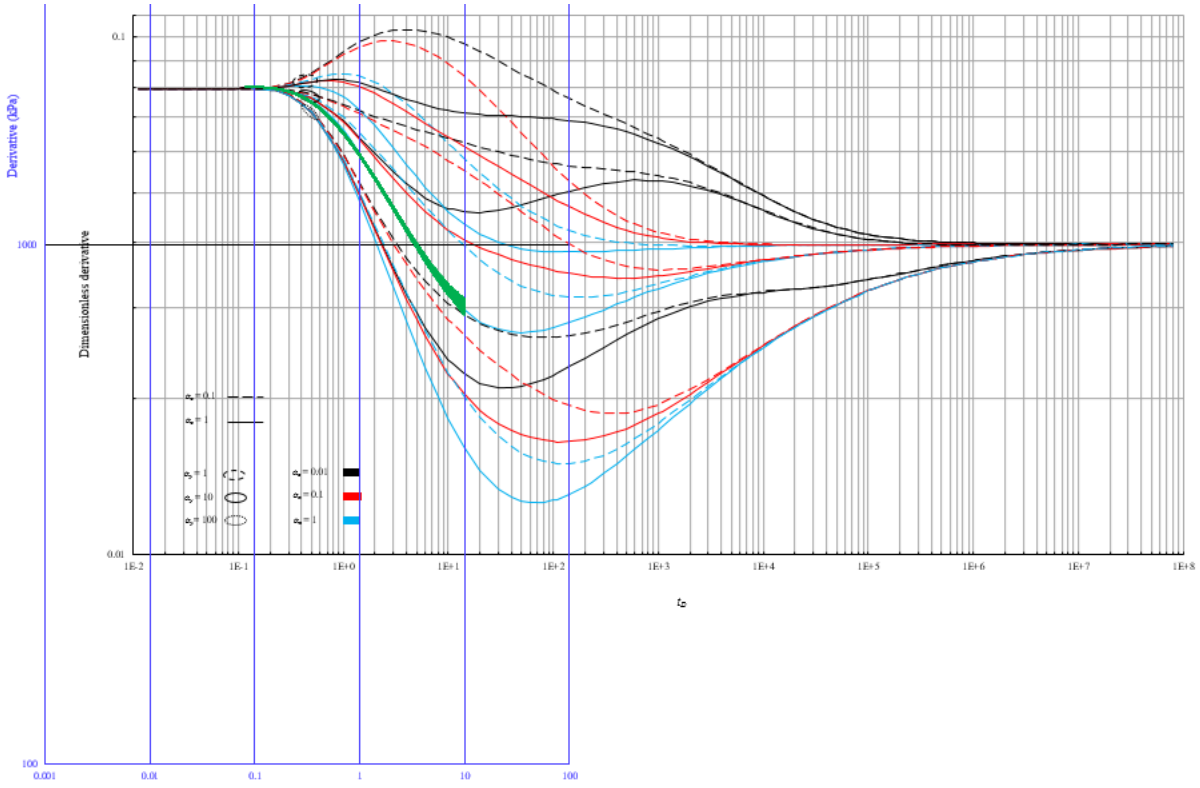

Fig. 3.24. Type curve matching for leaky fault characterization.

3.4. Fault leakage extension to multiple shallower formations

In this section, we propose an analytical solution for fault leakage into multiple overlying layers. The vertical fault intersects the sequential layers and divides each layer into two regions. The diffusivity equations are written for all regions of the connected layers. The fault structure is considered by a low permeability core surrounded by high permeability damaged zones. In addition, three directional flow is considered inside the fault zone. The system of equations is solved using Fourier and Laplace transforms. Applying the solution, fault leakage is investigated in three directions and the vertical extension of fault leakage into shallower formations is evaluated.

In the following, we explain the physical model and assumptions as well as the governing equations for fluid flow in the layers and the fault zone. Next, the system of equations is solved in

Laplace-Fourier domain. Finally, the solution is applied to a multi-layer system to show its potential and demonstrate its ability to determine effect of fault leakage.

3.4.1. Methodology

Fig. 3.25 shows the physical model of a leaky fault in a multi-layer system. The bottom layer is the injection zone and layers 1 to *N* are shallower permeable formations intersected by the fault. *k* and k_2 are the permeabilities of the injection zone at both sides of the fault and *h* is thickness of the injection zone. k_{aj} and h_{aj} are permeability and thickness of the above formations at both sides of the fault (for j=1, 2, …, 2N). The leaky fault can conduct fluid in three directions (x, y, and z). k_{fx}, k_{fy}, and k_{fz} are fault permeabilities in three directions. We assume fault permeabilities k_{fx} and k_{fy} are homogeneous along the fault plane in all layers. The vertical permeability of the fault may be defferent from a layer to another.

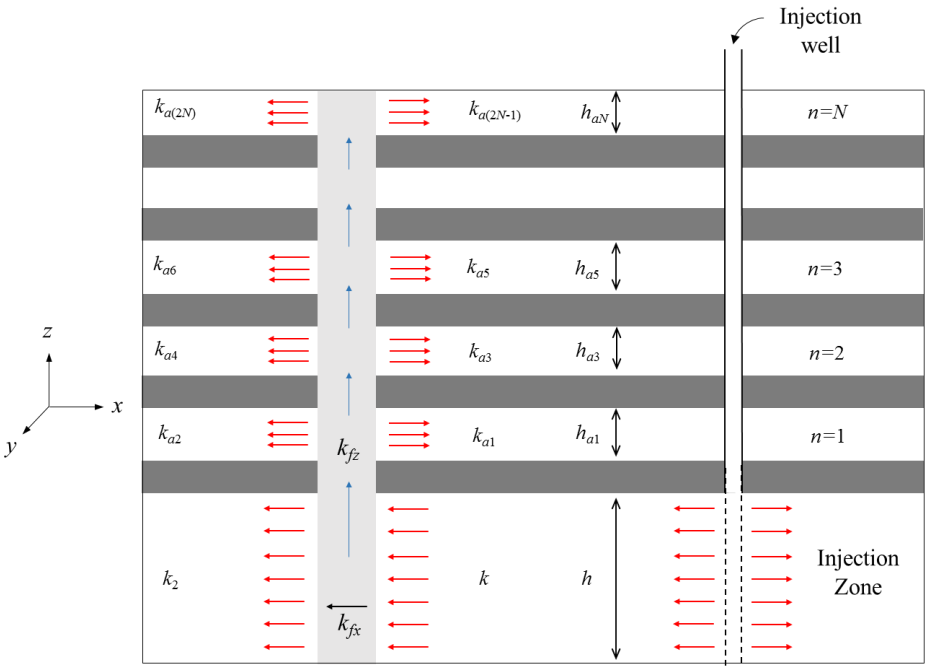

Fig. 3.25. Schematic of fault leakage in the multilayer system

In order to develop the analytical model, we need to write the diffusivity equations for all of the reservoir regions as well as the fault zone. Fault zone pressure is different at each reservoir/fault interface, therefore, we need to write separate flow equations for different parts of the fault zone connected to each reservoir region. In this model, we assume identical reservoir properties and thicknesses for all layers. Equations (1)-(8) show the diffusivity equations for reservoir regions:

$$\frac{\partial^2 \Delta p_1}{\partial x^2} + \frac{\partial^2 \Delta p_1}{\partial y^2} + \frac{q\mu}{kh}\delta(x-a)\delta(y) = \frac{1}{\eta}\frac{\partial \Delta p_1}{\partial t} \tag{3.54}$$

$$\frac{\partial^2 \Delta p_2}{\partial x^2} + \frac{\partial^2 \Delta p_2}{\partial y^2} = \frac{1}{\eta}\frac{\partial \Delta p_2}{\partial t} \tag{3.55}$$

$$\frac{\partial^2 \Delta p_{a1}}{\partial x^2} + \frac{\partial^2 \Delta p_{a1}}{\partial y^2} = \frac{1}{\eta}\frac{\partial \Delta p_{a1}}{\partial t} \tag{3.56}$$

$$\frac{\partial^2 \Delta p_{a2}}{\partial x^2} + \frac{\partial^2 \Delta p_{a2}}{\partial y^2} = \frac{1}{\eta}\frac{\partial \Delta p_{a2}}{\partial t} \tag{3.57}$$

$$\frac{\partial^2 \Delta p_{a3}}{\partial x^2} + \frac{\partial^2 \Delta p_{a3}}{\partial y^2} = \frac{1}{\eta}\frac{\partial \Delta p_{a3}}{\partial t} \tag{3.58}$$

$$\frac{\partial^2 \Delta p_{a4}}{\partial x^2} + \frac{\partial^2 \Delta p_{a4}}{\partial y^2} = \frac{1}{\eta}\frac{\partial \Delta p_{a4}}{\partial t} \tag{3.59}$$

For the last layer (n=*N*):

$$\frac{\partial^2 \Delta p_{a(2N-1)}}{\partial x^2} + \frac{\partial^2 \Delta p_{a(2N-1)}}{\partial y^2} = \frac{1}{\eta}\frac{\partial \Delta p_{a(2N-1)}}{\partial t} \tag{3.60}$$

$$\frac{\partial^2 \Delta p_{a(2N)}}{\partial x^2} + \frac{\partial^2 \Delta p_{a(2N)}}{\partial y^2} = \frac{1}{\eta}\frac{\partial \Delta p_{a(2N)}}{\partial t} \tag{3.61}$$

$$\frac{\partial^2 \Delta p_{f1}}{\partial y^2} + \frac{k}{k_{fy} w_f / 2} \frac{\partial \Delta p_1(t,0,y)}{\partial x} - \frac{2k_{fx}}{k_{fy} w_f} \frac{\Delta p_{f1} - \Delta p_{f2}}{w_f / 2} - \frac{k_{fz}}{k_{fy} h} \frac{\Delta p_{f1} - \Delta p_{fa1}}{L} = \frac{1}{\eta_{fy}} \frac{\partial \Delta p_{f1}}{\partial t} \tag{3.62}$$

$$\frac{\partial^2 \Delta p_{f2}}{\partial y^2} - \frac{k}{k_{fy} w_f / 2} \frac{\partial \Delta p_2(t,0,y)}{\partial x} + \frac{2k_{fx}}{k_{fy} w_f} \frac{\Delta p_{f1} - \Delta p_{f2}}{w_f / 2} - \frac{k_{fz}}{k_{fy} h} \frac{\Delta p_{f2} - \Delta p_{fa2}}{L} = \frac{1}{\eta_{fy}} \frac{\partial \Delta p_{f2}}{\partial t} \tag{3.63}$$

$$\frac{\partial^2 \Delta p_{fa1}}{\partial y^2} - \frac{k}{k_{fy} w_f / 2} \frac{-\partial \Delta p_{a1}(t,0,y)}{\partial x} - \frac{2k_{fx}}{k_{fy} w_f} \frac{\Delta p_{fa1} - \Delta p_{fa2}}{w_f / 2} + \frac{k_{fz}}{k_{fy} h} \frac{\Delta p_{f1} - \Delta p_{fa1}}{L} - \frac{k_{fz}}{k_{fy} h} \frac{\Delta p_{fa1} - \Delta p_{fa3}}{L} = \frac{1}{\eta_{fy}} \frac{\partial \Delta p_{fa1}}{\partial t} \tag{3.64}$$

$$\frac{\partial^2 \Delta p_{fa2}}{\partial y^2} - \frac{k}{k_{fy} w_f / 2} \frac{\partial \Delta p_{a2}(t,0,y)}{\partial x} + \frac{2k_{fx}}{k_{fy} w_f} \frac{\Delta p_{fa1} - \Delta p_{fa2}}{w_f / 2} + \frac{k_{fz}}{k_{fy} h} \frac{\Delta p_{f2} - \Delta p_{fa2}}{L} - \frac{k_{fz}}{k_{fy} h} \frac{\Delta p_{fa2} - \Delta p_{fa4}}{L} = \frac{1}{\eta_{fy}} \frac{\partial \Delta p_{fa2}}{\partial t} \tag{3.65}$$

$$\frac{\partial^2 \Delta p_{fa3}}{\partial y^2} - \frac{k}{k_{fy} w_f / 2} \frac{-\partial \Delta p_{a3}(t,0,y)}{\partial x} - \frac{2k_{fx}}{k_{fy} w_f} \frac{\Delta p_{fa3} - \Delta p_{fa4}}{w_f / 2} + \frac{k_{fz}}{k_{fy} h} \frac{\Delta p_{fa1} - \Delta p_{fa3}}{L} - \frac{k_{fz}}{k_{fy} h} \frac{\Delta p_{fa3} - \Delta p_{fa5}}{L} = \frac{1}{\eta_{fy}} \frac{\partial \Delta p_{fa3}}{\partial t} \tag{3.66}$$

$$\frac{\partial^2 \Delta p_{fa4}}{\partial y^2} - \frac{k}{k_{fy2} w_f / 2} \frac{\partial \Delta p_{a2}(t,0,y)}{\partial x} + \frac{2k_{fx}}{k_{fy} w_f} \frac{\Delta p_{fa1} - \Delta p_{fa2}}{w_f / 2} + \frac{k_{fz}}{k_{fy2} h} \frac{\Delta p_{f2} - \Delta p_{fa2}}{L} - \frac{k_{fz}}{k_{fy} h} \frac{\Delta p_{fa2} - \Delta p_{fa4}}{L} = \frac{1}{\eta_{fy}} \frac{\partial \Delta p_{fa4}}{\partial t} \tag{3.67}$$

For each reservoir region we write a diffusivity equation of fluid flow in fault zone:

For the last layer:

$$\frac{\partial^2 \Delta p_{fa(2N-1)}}{\partial y^2} - \frac{k}{k_{fy} w_f / 2} \frac{-\partial \Delta p_{a(2N-1)}(t,0,y)}{\partial x} - \frac{2k_{fx}}{k_{fy} w_f} \frac{\Delta p_{fa(2N-1)} - \Delta p_{fa(2N)}}{w_f / 2} + \frac{k_{fz}}{k_{fy} h} \frac{\Delta p_{fa(2N-1)} - \Delta p_{fa(2N-3)}}{L} = \frac{1}{\eta_{fy}} \frac{\partial \Delta p_{f(2N-1)}}{\partial t} \tag{3.68}$$

$$\frac{\partial^2 \Delta p_{fa(2N)}}{\partial y^2} - \frac{k}{k_{fy} w_f / 2} \frac{-\partial \Delta p_{a(2N-1)}(t,0,y)}{\partial x} - \frac{2k_{fx}}{k_{fy} w_f} \frac{\Delta p_{fa(2N-1)} - \Delta p_{fa(2N)}}{w_f / 2} + \frac{k_{fz}}{k_{fy} h} \frac{\Delta p_{fa(2N)} - \Delta p_{fa(2N-2)}}{L} = \frac{1}{\eta_{fy}} \frac{\partial \Delta p_{f(2N)}}{\partial t} \tag{3.69}$$

In order to solve the diffusivity equations of the multiple layers (Equations 1-8), we need reservoir-fault boundary conditions (Equations 17-22):

$$\frac{kh}{\mu} \frac{\partial \Delta p_1(t,0,y)}{\partial x} = \frac{kh}{\mu w_f / 4} \left(\Delta p_1(t,0,y) - \Delta p_{f1}(t,y) \right) \tag{3.70}$$

$$\frac{kh}{\mu}\frac{\partial \Delta p_2(t,0,y)}{\partial x}=\frac{kh}{\mu w_f/4}\left(\Delta p_{f2}(t,y)-\Delta p_2(t,0,y)\right) \tag{3.71}$$

$$-\frac{kh}{\mu}\frac{\partial \Delta p_{a1}(t,0,y)}{\partial x}=\frac{kh}{\mu w_f/4}\left(\Delta p_{fa1}(t,y)-\Delta p_{a1}(t,0,y)\right) \tag{3.72}$$

$$\frac{kh}{\mu}\frac{\partial \Delta p_{a2}(t,0,y)}{\partial x}=\frac{kh}{\mu w_f/4}\left(\Delta p_{fa2}(t,y)-\Delta p_{a2}(t,0,y)\right) \tag{3.73}$$

For the last layer (n=*N*):

$$-\frac{kh}{\mu}\frac{\partial \Delta p_{a(2N-1)}(t,0,y)}{\partial x}=\frac{kh}{\mu w_f/4}\left(\Delta p_{fa(2N-1)}(t,y)-\Delta p_{a(2N-1)}(t,0,y)\right) \tag{3.74}$$

$$-\frac{kh}{\mu}\frac{\partial \Delta p_{a(2N)}(t,0,y)}{\partial x}=\frac{kh}{\mu w_f/4}\left(\Delta p_{fa(2N)}(t,y)-\Delta p_{a(2N)}(t,0,y)\right) \tag{3.75}$$

Next, we convert the governing equations to dimensionless form. The dimensionless groups are defined below:

$$\begin{aligned} &p_{Dj}=\frac{kh}{q\mu}\Delta p_j \quad (\text{for } j=1,\ 2,\ a1,\ a2,\ f1,\ f2,\ fa1,\ fa2,\ \ldots,\ fa(2N\text{-}1),\ fa(2N)),\ t_D=\frac{\eta t}{a^2} \\ &\alpha_x=\frac{k_{fx}a}{kw_f},\ \ \alpha_y=\frac{k_{fy}w_f}{2ka},\ \ \alpha_z=\frac{k_{fz}aw_f}{2khL},\ \ w_{fD}=\frac{w_f}{a},\ \ \eta_{Df}=\frac{\eta_f}{\eta} \end{aligned} \tag{3.76}$$

where *a* is distance between well and fault and *L* is the distance between the middle height of the sequential layers. Equations (24)-(29) state diffusivity equations of reservoir zones in dimensionless form.

$$\frac{\partial^2 p_{D1}}{\partial {x_D}^2}+\frac{\partial^2 p_{D1}}{\partial {y_D}^2}+\delta(x_D-1)\delta(y_D)=\frac{\partial p_{D1}}{\partial t_D} \tag{3.77}$$

$$\frac{\partial^2 p_{D2}}{\partial {x_D}^2}+\frac{\partial^2 p_{D2}}{\partial {y_D}^2}=\frac{\partial p_{D2}}{\partial t_D} \tag{3.78}$$

$$\frac{\partial^2 p_{Da1}}{\partial x_D{}^2}+\frac{\partial^2 p_{Da1}}{\partial y_D{}^2}=\frac{\partial p_{Da1}}{\partial t_D} \tag{3.79}$$

$$\frac{\partial^2 p_{Da2}}{\partial x_D{}^2}+\frac{\partial^2 p_{Da2}}{\partial y_D{}^2}=\frac{\partial p_{Da2}}{\partial t_D} \tag{3.80}$$

For the N^{th} layer:

$$\frac{\partial^2 p_{Da(2N-1)}}{\partial x_D{}^2}+\frac{\partial^2 p_{Da(2N-1)}}{\partial y_D{}^2}=\frac{\partial p_{Da(2N-1)}}{\partial t_D} \tag{3.81}$$

$$\frac{\partial^2 p_{Da(2N)}}{\partial x_D{}^2}+\frac{\partial^2 p_{Da(2N)}}{\partial y_D{}^2}=\frac{\partial p_{Da(2N)}}{\partial t_D} \tag{3.82}$$

Next, we convert the fault-zone diffusivity equations to dimensionless form:

$$\frac{\partial^2 p_{Df1}}{\partial y_D{}^2}+\frac{1}{\alpha_y}\frac{\partial p_{D1}(t_D,0,y_D)}{\partial x_D}-\frac{2\alpha_x}{\alpha_y}(p_{Df1}-p_{Df2})-\frac{\alpha_z}{\alpha_y}(p_{Df1}-p_{Dfa1})=\frac{1}{\eta_{Df}}\frac{\partial p_{Df1}}{\partial t_D} \tag{3.83}$$

$$\frac{\partial^2 p_{Df2}}{\partial y^2}-\frac{1}{\alpha_y}\frac{\partial p_{D2}(t_D,0,y_D)}{\partial x_D}+\frac{2\alpha_x}{\alpha_y}(p_{Df1}-p_{Df2})-\frac{\alpha_z}{\alpha_y}(p_{Df2}-p_{Dfa2})=\frac{1}{\eta_{Df}}\frac{\partial p_{Df2}}{\partial t_D} \tag{3.84}$$

$$\frac{\partial^2 p_{Dfa1}}{\partial y_D{}^2}-\frac{1}{\alpha_y}\frac{-\partial p_{Da1}(t_D,0,y_D)}{\partial x_D}-\frac{2\alpha_x}{\alpha_y}(p_{Dfa1}-p_{Dfa2})+\frac{\alpha_z}{\alpha_y}(p_{Df1}-p_{Dfa1})-\frac{\alpha_z}{\alpha_y}(p_{Dfa1}-p_{Dfa3})=\frac{1}{\eta_{Df}}\frac{\partial p_{Dfa1}}{\partial t_D} \tag{3.85}$$

$$\frac{\partial^2 p_{Dfa2}}{\partial y^2}-\frac{1}{\alpha_y}\frac{\partial p_{Da2}(t_D,0,y_D)}{\partial x}+\frac{2\alpha_x}{\alpha_y}(p_{Dfa1}-p_{Dfa2})+\frac{\alpha_z}{\alpha_y}(p_{Df2}-p_{Dfa2})-\frac{\alpha_z}{\alpha_y}(p_{Dfa2}-p_{Dfa4})=\frac{1}{\eta_{Df}}\frac{\partial p_{Dfa2}}{\partial t_D} \tag{3.86}$$

For all other n^{th} layers other than the last layer:

$$\frac{\partial^2 p_{Dfa(2n-1)}}{\partial y_D^{\,2}} - \frac{1}{\alpha_y}\frac{-\partial p_{Da(2n-1)}(t_D,0,y_D)}{\partial x_D} - \frac{2\alpha_x}{\alpha_y}(p_{Dfa(2n-1)} - p_{Dfa(2n)}) + \frac{\alpha_z}{\alpha_y}(p_{Dfa(2n-1)} - p_{Dfa(2n-3)})$$
$$-\frac{\alpha_z}{\alpha_y}(p_{Df(2n-1)} - p_{Dfa(2n+1)}) = \frac{1}{\eta_{Df}}\frac{\partial p_{Dfa(2n-1)}}{\partial t_D} \tag{3.87}$$

$$\frac{\partial^2 p_{Dfa(2n)}}{\partial y^2} - \frac{1}{\alpha_y}\frac{\partial p_{Da(2n)}(t_D,0,y_D)}{\partial x_D} + \frac{2\alpha_x}{\alpha_y}(p_{Dfa(2n-1)} - p_{Dfa(2n)}) + \frac{\alpha_z}{\alpha_y}(p_{Dfa(2n-2)} - p_{Dfa(2n)})$$
$$-\frac{\alpha_z}{\alpha_y}(p_{Dfa(2n)} - p_{Dfa(2n+2)}) = \frac{1}{\eta_{Df}}\frac{\partial p_{Dfa(2n)}}{\partial t_D} \tag{3.88}$$

For the last layer:

$$\frac{\partial^2 p_{Dfa(2N-1)}}{\partial y_D^{\,2}} - \frac{1}{\alpha_y}\frac{-\partial p_{Da(2N-1)}(t_D,0,y_D)}{\partial x_D} - \frac{2\alpha_x}{\alpha_y}(p_{Dfa(2N-1)} - p_{Dfa(2N)}) + \frac{\alpha_z}{\alpha_y}(p_{Dfa(2N-1)} - p_{Dfa(2N-3)})$$
$$= \frac{1}{\eta_{Df}}\frac{\partial p_{Dfa(2N-1)}}{\partial t_D} \tag{3.89}$$

$$\frac{\partial^2 p_{Dfa(2N)}}{\partial y^2} - \frac{1}{\alpha_y}\frac{\partial p_{Da(2N)}(t_D,0,y_D)}{\partial x_D} + \frac{2\alpha_x}{\alpha_y}(p_{Dfa(2N-1)} - p_{Dfa(2N)}) + \frac{\alpha_z}{\alpha_y}(p_{Dfa(2N-2)} - p_{Dfa(2N)})$$
$$= \frac{1}{\eta_{Df}}\frac{\partial p_{Dfa(2N)}}{\partial t_D} \tag{3.90}$$

In order to convert the system of PDEs to ODEs, we apply Fourier-Laplace transforms to time and space (*y*-direction) variables. For reservoirs:

$$\frac{\partial^2 \bar{\bar{p}}_{D1}}{\partial x_D^{\,2}} - A^2 \bar{\bar{p}}_{D1} + \frac{1}{s}\delta(x_D - 1) = 0 \tag{3.91}$$

$$\frac{\partial^2 \bar{\bar{p}}_{D2}}{\partial x_D^{\,2}} - A^2 \bar{\bar{p}}_{D2} = 0 \tag{3.92}$$

$$\frac{\partial^2 \bar{\bar{p}}_{Da1}}{\partial x_D^{\,2}} - A^2 \bar{\bar{p}}_{Da1} = 0 \tag{3.93}$$

$$\frac{\partial^2 \bar{\bar{p}}_{Da2}}{\partial x_D^{\ 2}} - A^2 \bar{\bar{p}}_{Da2} = 0 \tag{3.94}$$

For all other n[th] layers other than the last layer:

$$\frac{\partial^2 \bar{\bar{p}}_{Da(2n-1)}}{\partial x_D^{\ 2}} - A^2 \bar{\bar{p}}_{Da(2n-1)} = 0 \tag{3.95}$$

$$\frac{\partial^2 \bar{\bar{p}}_{Da(2n)}}{\partial x_D^{\ 2}} - A^2 \bar{\bar{p}}_{Da(2n)} = 0 \tag{3.96}$$

For the last layer:

$$\frac{\partial^2 \bar{\bar{p}}_{Da(2N-1)}}{\partial x_D^{\ 2}} - A^2 \bar{\bar{p}}_{Da(2N-1)} = 0 \tag{3.97}$$

$$\frac{\partial^2 \bar{\bar{p}}_{Da(2N)}}{\partial x_D^{\ 2}} - A^2 \bar{\bar{p}}_{Da(2N)} = 0 \tag{3.98}$$

For fault zone:

$$-A_f^{\ 2} \bar{\bar{p}}_{Df1}(s,\omega) + \frac{1}{\alpha_y} \frac{\partial \bar{\bar{p}}_{D1}(s,0,\omega)}{\partial x_D} - \frac{2\alpha_x}{\alpha_y}(\bar{\bar{p}}_{Df1}(s,\omega) - \bar{\bar{p}}_{Df2}(s,\omega)) - \frac{\alpha_z}{\alpha_y}(\bar{\bar{p}}_{Df1}(s,\omega) - \bar{\bar{p}}_{Dfa1}(s,\omega)) = 0 \tag{3.99}$$

$$-A_f^{\ 2} \bar{\bar{p}}_{Df2}(s,\omega) - \frac{1}{\alpha_y} \frac{\partial \bar{\bar{p}}_{D2}(s,0,\omega)}{\partial x_D} + \frac{2\alpha_x}{\alpha_y}(\bar{\bar{p}}_{Df1}(s,\omega) - \bar{\bar{p}}_{Df2}(s,\omega)) - \frac{\alpha_z}{\alpha_y}(\bar{\bar{p}}_{Df2}(s,\omega) - \bar{\bar{p}}_{Dfa2}(s,\omega)) = 0 \tag{3.100}$$

$$-A_f^{\ 2} \bar{\bar{p}}_{Dfa1}(s,\omega) - \frac{1}{\alpha_y} \frac{-\partial \bar{\bar{p}}_{Da1}(s,0,\omega)}{\partial x_D} - \frac{2\alpha_x}{\alpha_y}(\bar{\bar{p}}_{Dfa1}(s,\omega) - \bar{\bar{p}}_{Dfa2}(s,\omega)) + \frac{\alpha_z}{\alpha_y}(\bar{\bar{p}}_{Df1}(s,\omega) - \bar{\bar{p}}_{Dfa1}(s,\omega)) - \frac{\alpha_z}{\alpha_y}(\bar{\bar{p}}_{Dfa1}(s,\omega) - \bar{\bar{p}}_{Dfa3}(s,\omega)) = 0 \tag{3.102}$$

$$-A_f^{\ 2} \bar{\bar{p}}_{Dfa2}(s,\omega) - \frac{1}{\alpha_y} \frac{\partial \bar{\bar{p}}_{Da2}(s,0,\omega)}{\partial x_D} + \frac{2\alpha_x}{\alpha_y}(\bar{\bar{p}}_{Dfa1}(s,\omega) - \bar{\bar{p}}_{Dfa2}(s,\omega)) + \frac{\alpha_z}{\alpha_y}(\bar{\bar{p}}_{Df2}(s,\omega) - \bar{\bar{p}}_{Dfa2}(s,\omega)) - \frac{\alpha_z}{\alpha_y}(\bar{\bar{p}}_{Dfa2}(s,\omega) - \bar{\bar{p}}_{Dfa4}(s,\omega)) = 0 \tag{3.103}$$

$$-A_f{}^2\bar{\bar{p}}_{Dfa(2n-1)}(s,\omega)-\frac{1}{\alpha_y}\frac{-\partial\bar{\bar{p}}_{Da(2n-1)}(s,0,\omega)}{\partial x_D}-\frac{2\alpha_x}{\alpha_y}(\bar{\bar{p}}_{Dfa(2n-1)}(s,\omega)-\bar{\bar{p}}_{Dfa(2n)}(s,\omega))$$
$$+\frac{\alpha_z}{\alpha_y}(\bar{\bar{p}}_{Dfa(2n-1)}(s,\omega)-\bar{\bar{p}}_{Dfa(2n-3)}(s,\omega))-\frac{\alpha_z}{\alpha_y}(\bar{\bar{p}}_{Df(2n-1)}(s,\omega)-\bar{\bar{p}}_{Dfa(2n+1)}(s,\omega))=0 \quad (3.104)$$

$$-A_f{}^2\bar{\bar{p}}_{Dfa(2n)}(s,\omega)-\frac{1}{\alpha_y}\frac{\partial\bar{\bar{p}}_{Da(2n)}(s,0,\omega)}{\partial x_D}+\frac{2\alpha_x}{\alpha_y}(\bar{\bar{p}}_{Dfa(2n-1)}(s,\omega)-\bar{\bar{p}}_{Dfa(2n)}(s,\omega))$$
$$+\frac{\alpha_z}{\alpha_y}(\bar{\bar{p}}_{Dfa(2n-2)}(s,\omega)-\bar{\bar{p}}_{Dfa(2n)}(s,\omega))-\frac{\alpha_z}{\alpha_y}(\bar{\bar{p}}_{Dfa(2n)}(s,\omega)-\bar{\bar{p}}_{Dfa(2n+2)}(s,\omega))=0 \quad (3.105)$$

$$-A_f{}^2\bar{\bar{p}}_{Dfa(2N-1)}(s,\omega)-\frac{1}{\alpha_y}\frac{-\partial\bar{\bar{p}}_{Da(2N-1)}(s,0,\omega)}{\partial x_D}-\frac{2\alpha_x}{\alpha_y}(\bar{\bar{p}}_{Dfa(2N-1)}(s,\omega)-\bar{\bar{p}}_{Dfa(2N)}(s,\omega))$$
$$+\frac{\alpha_z}{\alpha_y}(\bar{\bar{p}}_{Dfa(2N-1)}(s,\omega)-\bar{\bar{p}}_{Dfa(2N-3)}(s,\omega))=0 \quad (3.106)$$

$$-A_f{}^2\bar{\bar{p}}_{Dfa(2N)}(s,\omega)-\frac{1}{\alpha_y}\frac{\partial\bar{\bar{p}}_{Da(2N)}(s,0,\omega)}{\partial x_D}+\frac{2\alpha_x}{\alpha_y}(\bar{\bar{p}}_{Dfa(2N-1)}(s,\omega)-\bar{\bar{p}}_{Dfa(2N)}(s,\omega))$$
$$+\frac{\alpha_z}{\alpha_y}(\bar{\bar{p}}_{Dfa(2N-2)}(s,\omega)-\bar{\bar{p}}_{Dfa(2N)}(s,\omega))=0 \quad (3.107)$$

where $A^2=4\pi^2\omega^2+s$ and $A_f{}^2=4\pi^2\omega^2+s/\eta_{Df}$. The solution for pressure variations in multilayer system is given below.

$$\bar{\bar{p}}_{D1}=\frac{1}{2sA}e^{-|x_D-1|A}+C_1e^{-Ax_D}\quad,\ \bar{\bar{p}}_{D2}=C_2e^{Ax_D}$$
$$\bar{\bar{p}}_{Da1}=C_3e^{-Ax_D}\quad,\ \bar{\bar{p}}_{Da2}=C_4e^{Ax_D}$$
$$\bar{\bar{p}}_{Da3}=C_5e^{-Ax_D}\quad,\ \bar{\bar{p}}_{Da4}=C_6e^{Ax_D} \quad (3.108)$$
$$\vdots\qquad\qquad\vdots$$
$$\bar{\bar{p}}_{Da(2N-1)}=C_{2N-1}e^{-Ax_D}\quad,\ \bar{\bar{p}}_{Da(2N)}=C_{2N}e^{Ax_D}$$

Coefficients C_1-C_{2N} are functions of reservoir and fault properties calculated by solving the following system of linear algebraic equations for the coefficient vector C.

$$H.C = F \tag{3.109}$$

where:

$$F^T = \frac{e^{-A}}{8A\alpha_y s}\left[-4\alpha_y d_1 \quad 2\alpha_x(-4+Aw_{fD}) \quad \alpha_z(-4+Aw_{fD}) \quad 0 \quad 0 \quad \cdots \quad 0\right] \tag{3.110}$$

$$H = \begin{bmatrix} d_1 & m_1 & m_2 & 0 & 0 & 0 & 0 & 0 & 0 & 0 \\ m_1 & d_1 & 0 & m_2 & 0 & 0 & 0 & 0 & 0 & 0 \\ m_2 & 0 & d_2 & m_1 & m_2 & 0 & 0 & 0 & 0 & 0 \\ 0 & m_2 & m_1 & d_2 & 0 & \ddots & 0 & 0 & 0 & 0 \\ 0 & 0 & m_2 & 0 & d_2 & \ddots & m_2 & 0 & 0 & 0 \\ 0 & 0 & 0 & \ddots & \ddots & d_2 & \ddots & m_2 & 0 & 0 \\ 0 & 0 & 0 & 0 & m_2 & \ddots & \ddots & m_1 & m_2 & 0 \\ 0 & 0 & 0 & 0 & 0 & m_2 & m_1 & d_2 & 0 & m_2 \\ 0 & 0 & 0 & 0 & 0 & 0 & m_2 & 0 & d_1 & m_1 \\ 0 & 0 & 0 & 0 & 0 & 0 & 0 & m_2 & m_1 & d_1 \end{bmatrix} \tag{3.111}$$

$$C^T = \begin{bmatrix} C_1 & C_2 & \cdots & C_{2N+2} \end{bmatrix} \tag{3.112}$$

where H dimension is $(2N+2)\times(2N+2)$ and F dimension is $(2N+2)\times 1$. d_1, d_2, m_1, and m_2 are defined below.

$$\begin{aligned} d_1 &= -\frac{1}{4\alpha_y}\left[4(2\alpha_x + {A_f}^2\alpha_y + \alpha_z) + A(4 + 2\alpha_x w_{fD} + {A_f}^2\alpha_y w_{fD} + \alpha_z w_{fD})\right] \\ d_2 &= -\frac{1}{4\alpha_y}\left[4(2\alpha_x + {A_f}^2\alpha_y + \alpha_z) + A(4 + 2\alpha_x w_{fD} + {A_f}^2\alpha_y w_{fD} + 2\alpha_z w_{fD})\right] \\ m_1 &= \frac{\alpha_x}{2\alpha_y}(4 + Aw_{fD}) \\ m_2 &= \frac{\alpha_z}{4\alpha_y}(4 + Aw_{fD}) \end{aligned} \tag{3.113}$$

We apply numerical Fourier-Laplace transforms to convert the solution to time-space domain.

3.4.2. Results and discussion

In this section, we show the capability of the model to assess fault leakage to shallower formations as well as up-, across-, and along-fault fluid flow. In addition, the pressure response of the shallower formations is evaluated.

Fig. 3.26 shows the pressure derivative of the injection well response for different number of layers. It can be inferred that the vertical extension of fault leakage can be detected by the value of the ultimate derivative. The ultimate derivative of two-, three-, and four-layer systems are one-half, one-third, and one-quarter of the initial radial flow. In single layer system, there is no vertical leakage and the ultimate derivative is identical to the initial derivative.

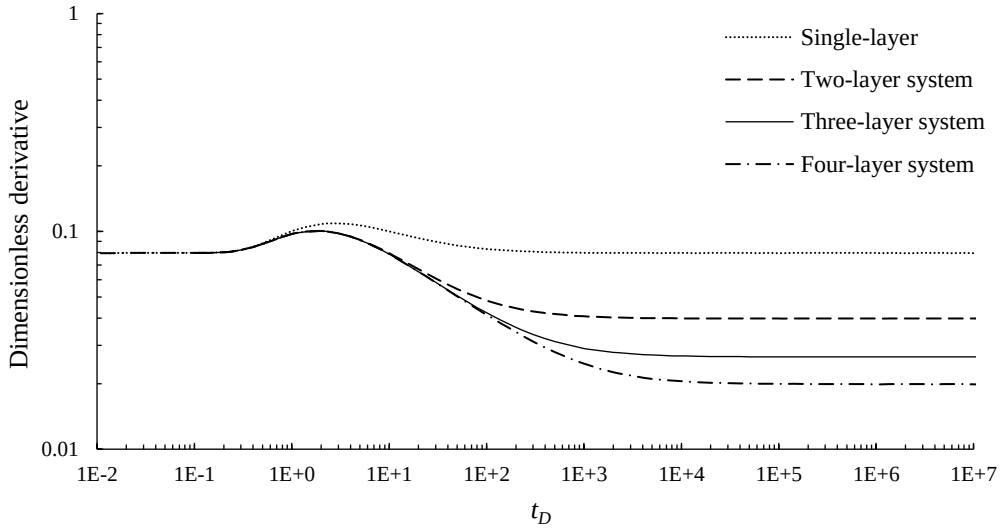

Fig. 3.26. Pressure derivative of the injection well for different number of layers

In above cases, we assumed that the transmissivity of all layers are identical. The effect of transmissivities must be considered if the transmissivities are not identical. Equation (60) below shows the effect of transmissivity ratios on the ultimate derivative (D_{ua}).

$$D_{ua} = \frac{2}{1 + T_{D2} + \sum_{1}^{2N} T_{Daj}} D \tag{3.114}$$

D is value of the derivative for initial radial flow, which is equal to 0.08 ($1/4\pi$). The value of D_{ua} shows the vertical extension of fault leakage to the shallower layers. For example, we consider a fault leakage system with the sequential permeable layers by the following transmissivity ratios: T_{D2}=0.5, T_{Da1}=0.5, T_{Da2}=0.5, T_{Da3}=0.25, T_{Da4}=0.25, T_{Da5}=0.25, and T_{Da6}=0.25. If fault leakage is extended into the third layer, D_{ua} is equal to 0.67D. If the leakage has reached to the fourth layer, D_{ua} is equal to 0.57D.

In this following, we provide an example problem for a fault leakage system with an injection layer and four shallower layers. The reservoir diffusivity is 10 m^2/s, porosity is 0.3, compressibility is 10^{-9} pa^{-1}, and fluid viscosity is 1 cp. Fault-well distance is 100 m, k_{fz}=100 mD, and k_{fx}=1 mD. The fault permeabilities and reservoir rock and fluid properties are similar to the multilayer example problem from Zeidouni (2016). Thicknesses of the layers are 40 m with 10 m impermeable layers in between. Fig. 3.27 shows the pressure responses of the above layers (n=1, 2, 3, 4) on a semi-log plot. The pressure is observed at 100 m far from the fault at region 1 of each layer. The along-fault permeability is identical to the reservoir permeability (k_{fy}=k=450 mD) for black curves (first case). The time that the pressure change reaches 1 psi (~7 kPa) for layers 1 and 2 are less than a day, for layer 3 is one day, and for layer 4 is 22 days. For the second case, we evaluate the effect of the along-fault permeability on the pressure responses of the above layers for k_{fy}=450 D (The brown curves). The pressure build-up of all layers for the second case is less than the first case. In this case, the times that the pressure of the layers reaches 1 psi are less than one day for layers 1 and 2, two days for layer 3, and 33 days for layer 4.

In the second case where k_{fy}=450 mD, fault allows for significant fluid flow along the fault plane that engages more reservoir volume to storage which was not engaged in the first case

(k_{fy}=0.450 mD). The along-fault fluid flow reduces the risk of fault reactivation that may happen by pressure build-up.

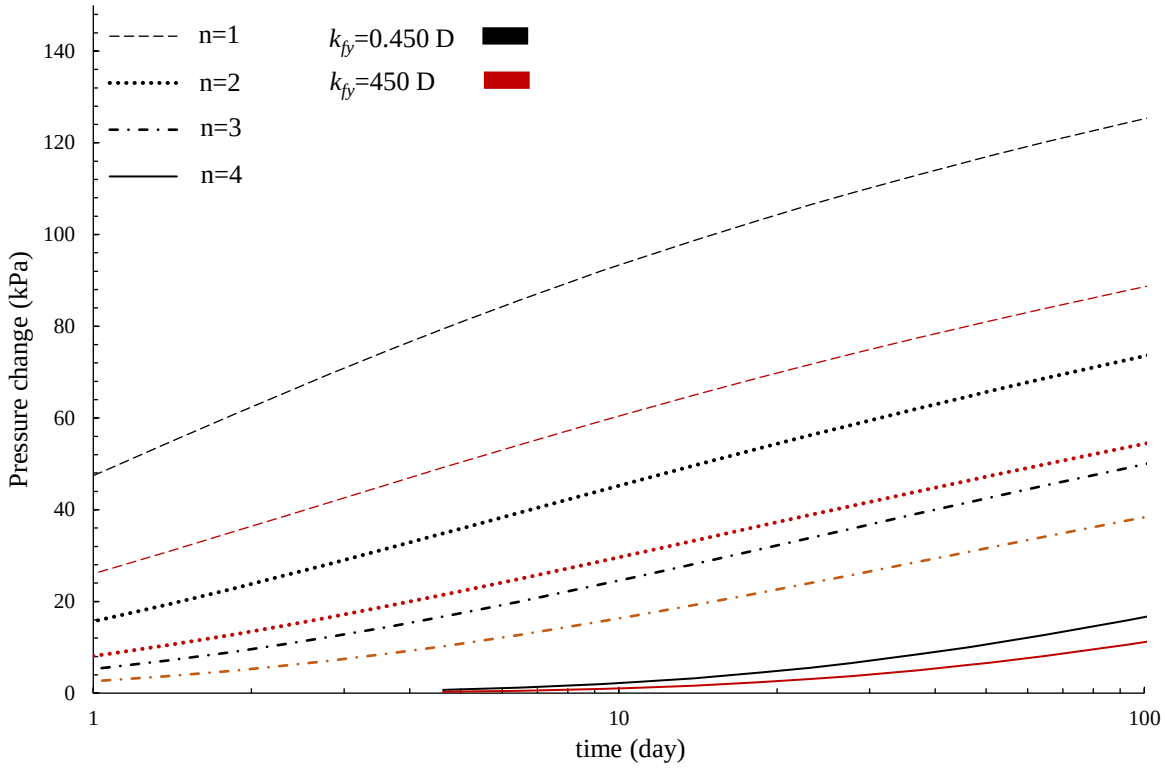

Fig. 3.27. Pressure response of the shallower formations in a five-layer system

Next, we investigate the effect of fault leakage on a production case. We assume same number of layers and reservoir properties as the above example problem. The active well is producing from the bottom reservoir that leads to fault migration from the four above zone aquifers to the production layer. We investigate the production for the following cases: (i) k_{fy}=0.450, (ii) k_{fy}=450, (iii) No fault. Fig. 3.28 shows that fault fluid flow reduces the pressure drawdown comparing to the no fault case. The pressure drawdown for no fault case is about 790 kPa after 1 years of production. However, it reduces to 757 kPa and 683 kPa for k_{fy}=0.450 and k_{fy}=450, respectively. The fluid flow from the above aquifers supports the reservoir pressure during the

production that reduces the reservoir pressure decline. In addition, the along-fault fluid flow engages more reservoir volume to the production that also leads to less pressure drawdown.

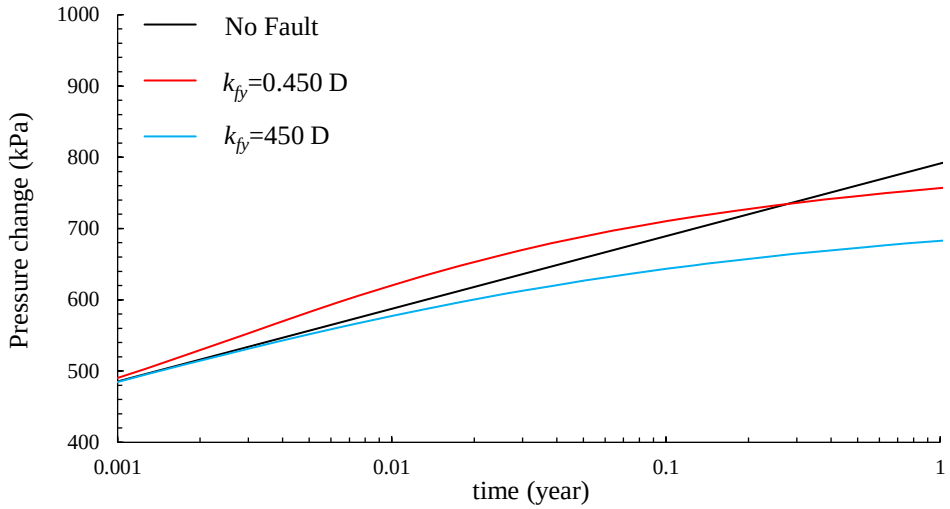

Fig. 3.28. Pressure drawdown of the production well

Fig. 3.29 illustrates the pressure derivative of the production well for the three cases. The horizontal line in Fig. 3.29 shows that the radial flow is not distracted in the no fault case. However, the pressure derivative significantly decreases due to aquifer support caused by the fault leakage. The early-time hump of the red curve shows the across-fault resistance to flow as the across fault permeability is significantly low (Fig. 3.29). This early-time rise in pressure derivative causes the temporary rise in pressure drawdown at early-time comparing to the no-fault case (Fig. 3.28). The high along-fault permeability prevents this early time hump in pressure derivative (blue curve in Fig. 3.29).

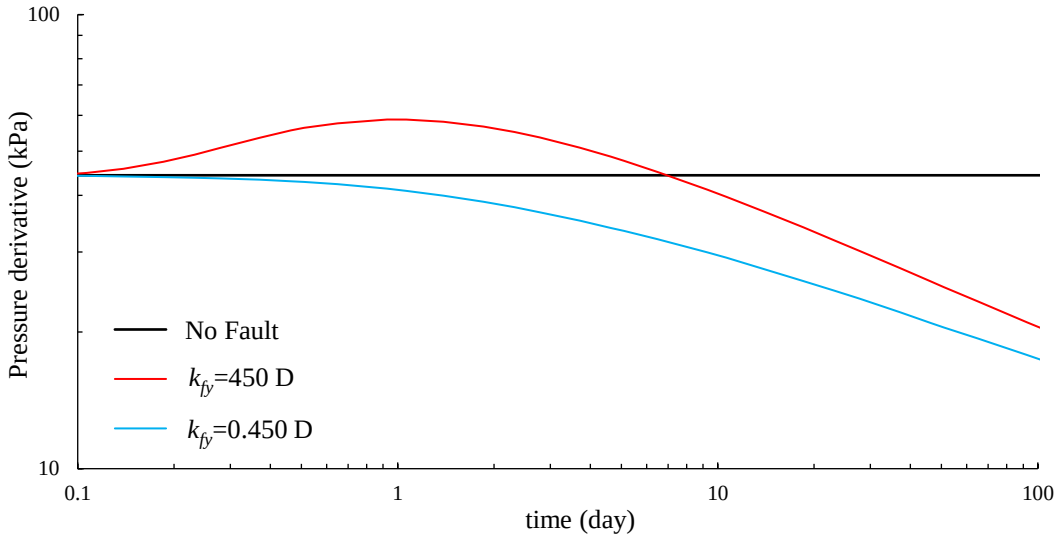

Fig. 3.29. Pressure derivative of the production well

3.5. Summary

In this chapter, we present a type-curve based method to characterize a vertically and laterally leaking fault using pressure data. In order to develop the type curves, we present an analytical solution to evaluate the pressure response corresponding to injection/production near a leaky fault. For the first model, we neglect the resistance to flow by overlying/underlying permeable layers connected to the reservoir by the fault. The reservoir is divided into two regions at each side of the fault plane. In addition, the reservoir properties on the two sides of the fault are considered non-identical. The analytical solution was verified against the numerical simulation results. The model was next cast in the form of type curves to characterize lateral and vertical leakage through the fault and the reservoir properties on the two sides of the fault.

For the second model, an analytical solution is derived for anisotropic fault leakage to a shallower formation in which, the three-directional flow is considered inside the fault zone. The analytical solution is validated with the numerical results and good agreement is observed. Results show that the pressure response is distinctly sensitive to the fault conductivities. Type curves are

provided from pressure derivative curves based on the variations of fault conductivities. Type curves are classified into three categories: (1) sealing fault, (2) vertically-sealing and laterally-leaking fault, and (3) vertically-leaking fault. In the first category, the derivative value of the late-time horizontal line is doubled after the early-time radial flow. In the second category, the late time derivative value is equal to the derivative on the early-time radial flow. In the third category, the late time derivative is half of the early time derivative value. Type curves are grouped based on the variations of fault conductivities in three directions. The across-fault conductivity can be grouped by the early-time merge of the pressure derivative values. The derivative curves of identical values of along-fault conductivity would merge at the late time before reaching to the ultimate steady state radial flow

For the third model, an analytical approach is proposed to investigate the pressure perturbation of fault leakage in a multilayer system. The leaky fault intersected the sequential permeable layers that are otherwise confined by impermeable layers. The system of diffusivity equations is written and solved for all of the permeable layers as well as the fault zone and the anisotropic fluid flow is considered in the fault. This model is capable to estimate the pressure variations of all layers during the leakage occurrence considering that the fault-zone pressure is different in vicinity of different permeable layers. The effect of fault leakage is investigated for injection and production cases.

CHAPTER 4. LEAKY CAPROCK

Thin shale layers isolating productive intervals in a reservoir have important implications for reservoir development and EOR strategies. In addition, weaknesses in caprocks overlying injection intervals may adversely affect the safety of fluid injection approaches including gas storage, waste water disposal, and CO_2 geological storage. Even low permeability of a caprock overlying the injection zone can be very important by allowing for pressure dissipation out of the reservoir. In this work, we apply harmonic pressure testing method to characterize a caprock overlying a given injection zone. A periodic flow rate pulse is disseminated from the injection well. The pressure pulses traveled through the caprock are observed in the above zone. The hydraulic characteristics of the low permeability caprock are estimated applying the analytical solution based on the above zone pressure amplitude. The caprock diffusivity is found to be in acceptable agreement with the true value. It is shown that the harmonic pulse testing is useful to characterize the intra/inter reservoir low permeability layers (caprocks).

4.1. Introduction

Existence and characteristics of low-permeability thin/thick zones isolating permeable layers from other permeable zones in multilayered system and/or from those out of a reservoir are highly important for reservoir development. Presence of even thin shale layers in a multilayer reservoir can determine if cross flow between layers may occur.

Cheng and Morohunfola (1993) and Cihan et al. (2011) derived analytical solutions for caprock leakage from an injection layer to adjacent formations. Dejam and Hassanzadeh (2018) presented a three dimensional model for caprock diffuse leakage. These models are based on the conventional pressure modeling methods in which the active well is at constant rate or constant pressure conditions.

Extending conventional well testing methods, harmonic (periodic) well testing can be applied for reservoir characterization. The periodic pressure signals from an active well travel through the media and the signals are observed at a passive well nearby. Pulse testing is an oscillatory method of evaluating inter-connection of two wells to estimate the reservoir properties in between (Fokker, Borello, Serazio, & Verga, 2012; Johnson, Greenkorn, & Woods, 1966). In conventional well testing methods, the noise produced from the active wells are normally strong, because the active wells cause significant flow streams in the reservoir (Renner & Messar, 2006). In periodic well testing, the noise effects are minimized in comparison with conventional methods that require mobilization of significant amount of fluid. The signal-to-noise ratio (SNR) is improved by applying Fourier transform on the pressure data (Knabe & Wang, 2011). Unlike conventional drawdown test where constant rate constraint is strictly required, constant rate over each flow period is not necessary for harmonic interpretation because rate fluctuations mainly affect the high frequency components, which are relevant to the near wellbore (Fokker, Borello, Verga, & Viberti, 2017; Hollaender, Hammond, & Gringarten, 2002). In addition, there is no need to shut in the well during the test nor it is needed to know the well rate history for pressure analysis (Hollaender et al., 2002). Kuo (1972) showed that if the well boundary condition is periodic, the induced pressure signal through the reservoir would be periodic with the same frequency. Many works have been done on reservoir characterization by periodic pressure testing (Fokker & Verga, 2011; Knabe & Wang, 2011; Rosa & Horne, 1997; Shakiba & Hosseini, 2016; Shakiba, Hosseini, & Sepehrnoori, 2017; Sun, Lu, & Hovorka, 2015).

In this chapter, we provide an analytical solution for a system of two layers separated with a low permeability caprock in between. The analytical solution is in frequency domain and the injection rate is periodic. The solution can give the periodic signals in the injection zone, above

zone, and low permeability layer. We characterize the low permeability caprock using the analytical solution. We provide an example problem to show the application of the characterization method.

4.2. Methodology

The physical model consists of the injection and above zones and the caprock layer in between (Fig. 4.1). The caprock layer is low permeability and the injection well is perforated in the middle of the injection zone. The thicknesses of the injection zone, caprock, and above zone are h, h_c, and h_a, respectively. Subscripts a and c denotes caprock and above zone. η, η_c, and η_a are the diffusivity coefficients of injection zone, caprock and above zone respectively. The injection pulse is disseminated from the injection well and travels through the caprock to the above zone. The diffusivity equations are written for the three layers. Fourier transform is applied to solve the system of diffusivity equations. In this analytical solution the time variable is converted to frequency domain by the Fourier transform. The injection well is perforated at (x=0, y=0, z=z_w).

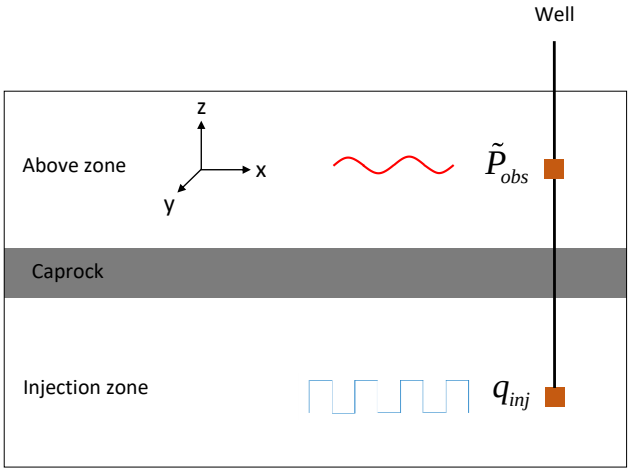

Fig. 4.1. Schematic representation of the physical model

4.3. Mathematical modeling

The system of diffusivity equations for injection zone, caprock, and the above zone is as below. For the injection zone:

$$\frac{\partial^2 p}{\partial x^2}+\frac{\partial^2 p}{\partial y^2}+\frac{\partial^2 p}{\partial z^2}+\frac{\mu}{kh}\delta(x)\delta(y)\delta(z)q(t)=\frac{1}{\eta}\frac{\partial p}{\partial t} \tag{4.1}$$

where $q(t)$ is the injection rate. δ is the Dirac-delta function, which is applied on the space parameters to specify the injection well location. The injection rate $q(t)$ is considered as a square pulse, which includes sequential injection and shut in periods. Equation (4.2) shows the square pulse injection rate.

$$q(t)=q_0\sum_{j=0}^{n-1}\left(\frac{(-1)^j+3}{4}\right)\Pi\left(\frac{2t}{T}-j-\frac{1}{2}\right) \tag{4.2}$$

where T is period of each cycle. Equation (4.2) shows that the injection rate is q_0 during the first half of each cycle and $q_0/2$ during the second half. This equation can be modified to model any rate change over a given pulse. n is the number of injection cycles. Π is the box function (Equation 4.3).

$$\Pi(t)=\begin{cases}1 & -\frac{1}{2}\le t\le\frac{1}{2}\\ 0 & \text{otherwise}\end{cases} \tag{4.3}$$

For caprock layer:

$$\frac{\partial^2 p_c}{\partial x^2}+\frac{\partial^2 p_c}{\partial y^2}+\frac{\partial^2 p_c}{\partial z^2}=\frac{1}{\eta_c}\frac{\partial p_c}{\partial t} \tag{4.4}$$

For above zone:

$$\frac{\partial^2 p_a}{\partial x^2}+\frac{\partial^2 p_a}{\partial y^2}+\frac{\partial^2 p_a}{\partial z^2}=\frac{1}{\eta_a}\frac{\partial p_a}{\partial t} \tag{4.5}$$

Equation (6) shows the initial and boundary conditions of the system.

$$
\begin{aligned}
&p(0,x,y,z) = p_i \\
&p_c(0,x,y,z) = p_i \\
&p_a(0,x,y,z) = p_i \\
&p(t,\pm\infty,y,0) = 0 \\
&p(t,x,\pm\infty,0) = 0 \\
&p_c(t,\pm\infty,y,0) = 0 \\
&p_c(t,x,\pm\infty,0) = 0 \\
&p_a(t,\pm\infty,y,0) = 0 \\
&p_a(t,x,\pm\infty,0) = 0 \\
&\frac{\partial p(t,x,y,0)}{\partial z} = 0 \\
&p(t,x,y,h) = p_c(t,x,y,h) \\
&\frac{\partial p(t,x,y,h)}{\partial z} = k_c \frac{\partial p_c(t,x,y,h)}{\partial z} \\
&p_c(t,x,y,h+h_c) = p_a(t,x,y,h+h_c) \\
&k_c \frac{\partial p_c(t,x,y,h+h_c)}{\partial z} = k_a \frac{\partial p_a(t,x,y,h+h_c)}{\partial z} \\
&\frac{\partial p_a(t,x,y,h+h_c+h_a)}{\partial z} = 0
\end{aligned}
\tag{4.6}
$$

We convert the equations to dimensionless form for brevity of the solution. The dimensionless groups are defined in Equation (4.7).

$$
p_D = \frac{kh}{q\mu}\Delta p\,,\quad t_D = \frac{\eta t}{l^2}\,,\quad x_D = \frac{x}{l}\,,\quad y_D = \frac{y}{l}\,,\quad z_D = \frac{z}{l} \tag{4.7}
$$

Equations (4.8)-(4.12) show the system of diffusivity equations and boundary conditions in dimensionless form.

$$
\frac{\partial^2 p_D}{\partial x_D^2} + \frac{\partial^2 p_D}{\partial y_D^2} + \frac{\partial^2 p_D}{\partial z_D^2} + \delta(x_D)\delta(y_D)\delta(z_D)q_D(t_D) = \frac{\partial p_D}{\partial t_D} \tag{4.8}
$$

$$
q_D(t_D) = \sum_{j=0}^{n-1}\left(\frac{(-1)^j + 3}{4}\right)\Pi\left(\frac{2t_D}{T_D} - j - \frac{1}{2}\right) \tag{4.9}
$$

where $T_D = \frac{\eta T}{l^2}$.

$$\frac{\partial^2 p_{cD}}{\partial x_D^2} + \frac{\partial^2 p_{cD}}{\partial y_D^2} + \frac{\partial^2 p_{cD}}{\partial z_D^2} = \frac{1}{\eta_{cD}} \frac{\partial p_{cD}}{\partial t_D} \tag{4.10}$$

$$\frac{\partial^2 p_{aD}}{\partial x_D^2} + \frac{\partial^2 p_{aD}}{\partial y_D^2} + \frac{\partial^2 p_{aD}}{\partial z_D^2} = \frac{1}{\eta_{aD}} \frac{\partial p_{aD}}{\partial t_D} \tag{4.11}$$

$$\begin{aligned}
&p_D\left(0, x_D, y_D, z_D\right) = p_{cD}\left(0, x_D, y_D, z_D\right) = p_{aD}\left(0, x_D, y_D, z_D\right) = \\
&p_D\left(t_D, \pm\infty, y_D, 0\right) = p_D\left(t_D, x_D, \pm\infty, 0\right) = p_{cD}\left(t_D, \pm\infty, y_D, 0\right) = \\
&p_{cD}\left(t_D, x_D, \pm\infty, 0\right) = p_{aD}\left(t_D, \pm\infty, y_D, 0\right) = p_{aD}\left(t_D, x_D, \pm\infty, 0\right) = 0 \\
&\frac{\partial p_D\left(t_D, x_D, y_D, 0\right)}{\partial z_D} = 0 \\
&p_D\left(t_D, x_D, y_D, h_D\right) = p_{cD}\left(t_D, x_D, y_D, h_D\right) \\
&\frac{\partial p_D\left(t_D, x_D, y_D, h_D\right)}{\partial z_D} = k_{cD} \frac{\partial p_{cD}\left(t_D, x_D, y_D, h_D\right)}{\partial z_D} \\
&p_{cD}\left(t_D, x_D, y_D, h_D + h_{cD}\right) = p_{aD}\left(t_D, x_D, y_D, h_D + h_{cD}\right) \\
&k_{cD} \frac{\partial p_{cD}\left(t_D, x_D, y_D, h_D + h_{cD}\right)}{\partial z_D} = k_{aD} \frac{\partial p_{aD}\left(t_D, x_D, y_D, h_D + h_{cD}\right)}{\partial z_D} \\
&\frac{\partial p_{aD}\left(t_D, x_D, y_D, h_D + h_{cD} + h_{aD}\right)}{\partial z_D} = 0
\end{aligned} \tag{4.12}$$

We transform the system of equations and boundary conditions into the Fourier domain to derive an analytical solution. The Fourier transform is defined in Equation (4.13a). F(*s*) is Fourier transform of function *f(t)*. We apply the Fourier transform on time (*t*) and space (*x* and *y*) domains (Equation (4.13b)).

$$\mathcal{F}(s) = \int_{-\infty}^{+\infty} f(t) e^{-2\pi i s t} dt \tag{4.13a}$$

$$\bar{\bar{p}}_D(s, \xi, \omega, z_D) = \int_{-\infty}^{+\infty} \int_{-\infty}^{+\infty} \int_{-\infty}^{+\infty} p_D(t_D, x_D, y_D, z_D) e^{-2\pi i \xi x_D} e^{-2\pi i \omega y_D} e^{-2\pi i s t_D} dx_D dy_D dt_D \tag{4.13b}$$

The system of equations in Fourier domain is given by:

$$\frac{\partial^2 \bar{\bar{p}}_D}{\partial z_D^2} + \delta(z_D)\bar{q}_D(s) = A^2 \bar{\bar{p}}_D \tag{4.14}$$

$$\bar{\bar{q}}_D(s) = \frac{(-1+e^{\pi i s T_D})}{8\pi i s} \sum_{j=0}^{n-1} (12 + (-1)^j) e^{-\pi i s T_D (1+j)} \tag{4.15}$$

$$\frac{\partial^2 \bar{\bar{p}}_{cD}}{\partial z_D^2} = A_c{}^2 \bar{\bar{p}}_{cD} \tag{4.16}$$

$$\frac{\partial^2 \bar{\bar{p}}_{aD}}{\partial z_D^2} = A_a{}^2 \bar{\bar{p}}_{aD} \tag{4.17}$$

where:

$$A = \sqrt{2\pi i s + 4\pi^2(\xi^2 + \omega^2)} \tag{4.18}$$

$$A_c = \sqrt{\frac{2\pi i s}{\eta_{cD}} + 4\pi^2(\xi^2 + \omega^2)} \tag{4.19}$$

$$A_a = \sqrt{\frac{2\pi i s}{\eta_{aD}} + 4\pi^2(\xi^2 + \omega^2)} \tag{4.20}$$

$$\begin{aligned}
&\frac{\partial \bar{\bar{p}}_D(s,\xi,\omega,0)}{\partial z_D} = 0 \\
&\bar{\bar{p}}_D(s,\xi,\omega,h_D) = \bar{\bar{p}}_{cD}(s,\xi,\omega,h_D) \\
&\frac{\partial \bar{\bar{p}}_D(s,\xi,\omega,h_D)}{\partial z_D} = \frac{\partial \bar{\bar{p}}_{cD}(s,\xi,\omega,h_D)}{\partial z_D} \\
&\bar{\bar{p}}_{cD}(s,\xi,\omega,h_D + h_{cD}) = \bar{\bar{p}}_{aD}(s,\xi,\omega,h_D + h_{cD}) \\
&\frac{\partial \bar{\bar{p}}_{cD}(s,\xi,\omega,h_D + h_{cD})}{\partial z_D} = \frac{\partial \bar{\bar{p}}_{aD}(s,\xi,\omega,h_D + h_{cD})}{\partial z_D} \\
&\frac{\partial \bar{\bar{p}}_{aD}(s,\xi,\omega,h_D + h_{cD} + h_{aD})}{\partial z_D} = 0
\end{aligned} \tag{4.21}$$

Equations (4.22)-(4.24) show the solution in frequency domain.

$$\bar{\bar{p}}_D = C_1 e^{Az_D} + C_2 e^{-Az_D} + \frac{\bar{\bar{q}}_D(s)}{2A} e^{-Az_D - Az_{wD}} \left(-e^{2A.z_D} + e^{2A.z_{wD}}\right) h(z_D - z_{wD}) \tag{4.22}$$

$$\bar{\bar{p}}_{cD} = C_3 e^{A_c z_D} + C_4 e^{-A_c z_D} \tag{4.23}$$

$$\bar{\bar{p}}_{aD} = C_5 e^{A_a z_D} + C_6 e^{-A_a z_D} \tag{4.24}$$

h is Heaviside function given by:

$$h(t) = \begin{vmatrix} 1 & x > 0 \\ 0 & x < 0 \end{vmatrix} \tag{4.25}$$

In order to apply the analytical solution, we use numerical Fourier inversion to revert the solution to *x* and *y* space domain. However, we keep the time variable in frequency domain. The observed pressure should be converted into Fourier domain using discrete Fourier transform (Equation (4.26)).

$$\bar{p}(s) = \sum_{j=0}^{N-1} \bar{p}(t_j) e^{-2\pi i s t_j} \Delta t \tag{4.26}$$

N is number of the pressure data and Δt is sampling time interval.

4.4. Results and discussion

In this section, we compare the analytical solution with the numerical simulation and provide an example problem for caprock characterization.

4.4.1. Validation

System properties are given in Table 4.2. The value of the compressibility can be in order of 10^{-10} for permeable layer and caprock (Lei, Cao, McPherson, Liao, & Chen, 2019; Mbia et al., 2014). The simulated above zone pressure response and injection flow rate are shown in Fig. 4.2a. The pressure is recorded at point z_D=1.0525. For simplicity, we assumed that the injection rate is zero at the second half of each injection cycle.

Table 4.1. Values of the system properties

Parameter	Value	Parameter	Value
k (m^2)	50×10^{-15}	ϕ_a	0.1
k_c (m^2)	5×10^{-16}	c_t (1/Pa)	10^{-10}
k_a (m^2)	10×10^{-15}	q_0 (m^3/s)	0.023
h (m)	100	μ (Pa.s)	0.0005
h_c (m)	5	T(s)	7200
h_a (m)	100	n	12
ϕ	0.1	l (m)	100
ϕ_c	0.1	z_w (m)	50

The simulated data is converted into the frequency domain. The analytical solution and numerical simulation results are compared in Fig. 4.2b in terms of amplitude of the above zone pressure signals versus frequency. In order to compare the curves, we evaluate the amplitudes only at harmonic frequencies (the spikes in the curves). The background in the amplitude curves may not match due to the numerical artifacts and the non-zero trend in the pressure data. The resolution of space discretization also may cause difference between the analytical and numerical results in the background data points, but still the match is good at harmonic frequencies. In the next section, we show that the analytical solution is accurate enough to evaluate the system properties.

(a)

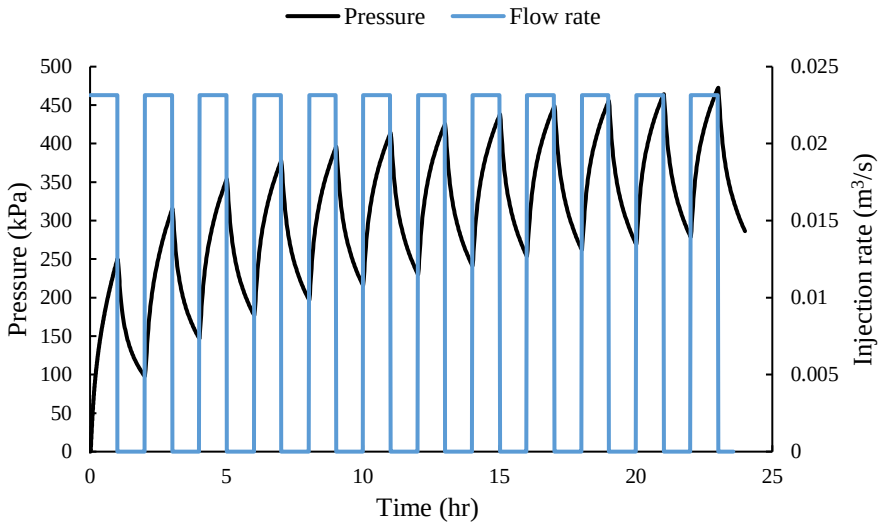

(b)

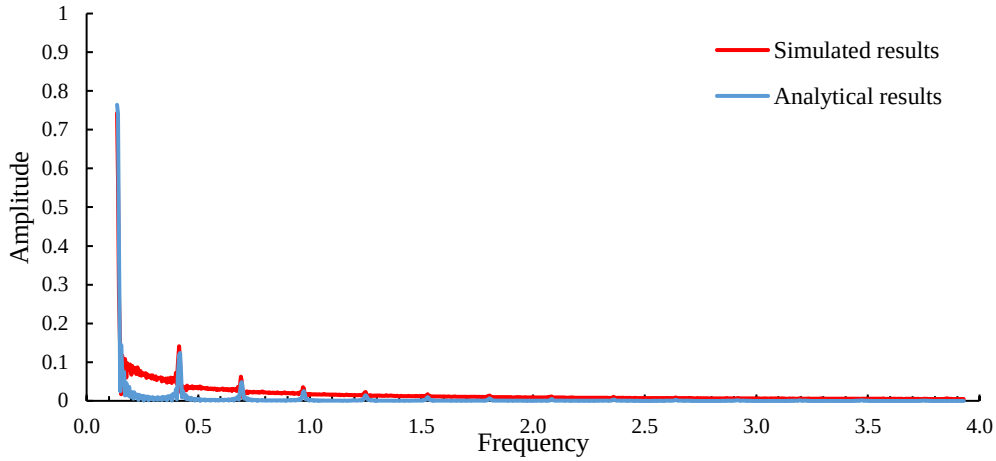

Fig. 4.2. (a) Injection rate and above zone pressure response (b) Amplitude of above zone pressure response for analytical solution against numerical simulation

4.4.2. Example problem

In this section, we present an example problem of pulse testing for caprock characterization. We simulated the two-layer system shown in Fig. 4.1. The rock and fluid properties are given in Table 4.2 except for the caprock permeability, which is 2×10^{-16} m^2. Fig. 4.3 shows the injection rate and above zone pressure response observed from a point in the above zone close to the caprock surface (z_D =1.0525).

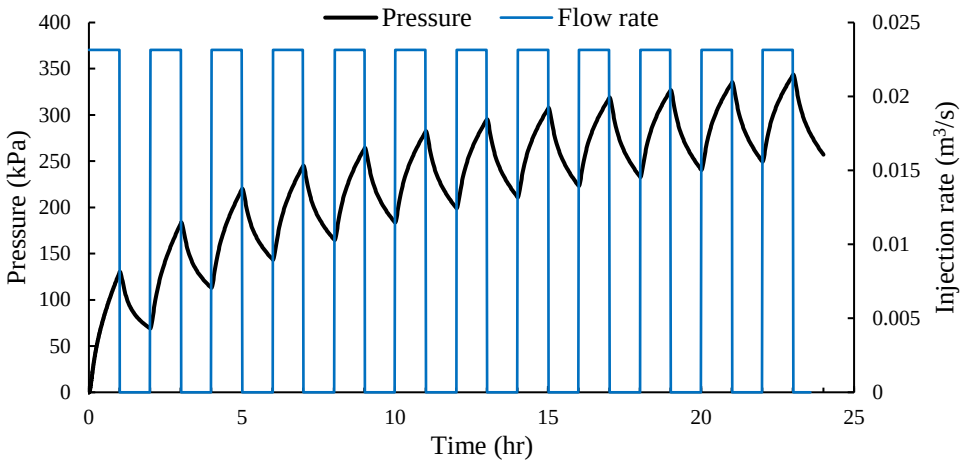

Fig. 4.3. Above zone pressure response for example problem

We use Discrete Fourier transform to calculate the amplitude of the above zone pressure of Fig. 4.3 in the frequency domain. Next, we compare the above zone response with the analytical solution to estimate the caprock diffusivity. We modified the caprock diffusivity in the analytical solution to match the amplitude of the above zone pressure response (Fig. 4.4). Fig. 4.4 shows that the amplitude of pressure response in the above zone varies as a function of caprock diffusivity. Higher caprock diffusivity coefficients lead to stronger signals observed at the above zone. In a tight caprock with a low diffusivity coefficient, most of the pressure signal is attenuated as it travels through the media. Moreover, based on this figure, the dimensionless diffusivity ratio matched by the analytical solution is 0.004, which is very close to that of the above zone.

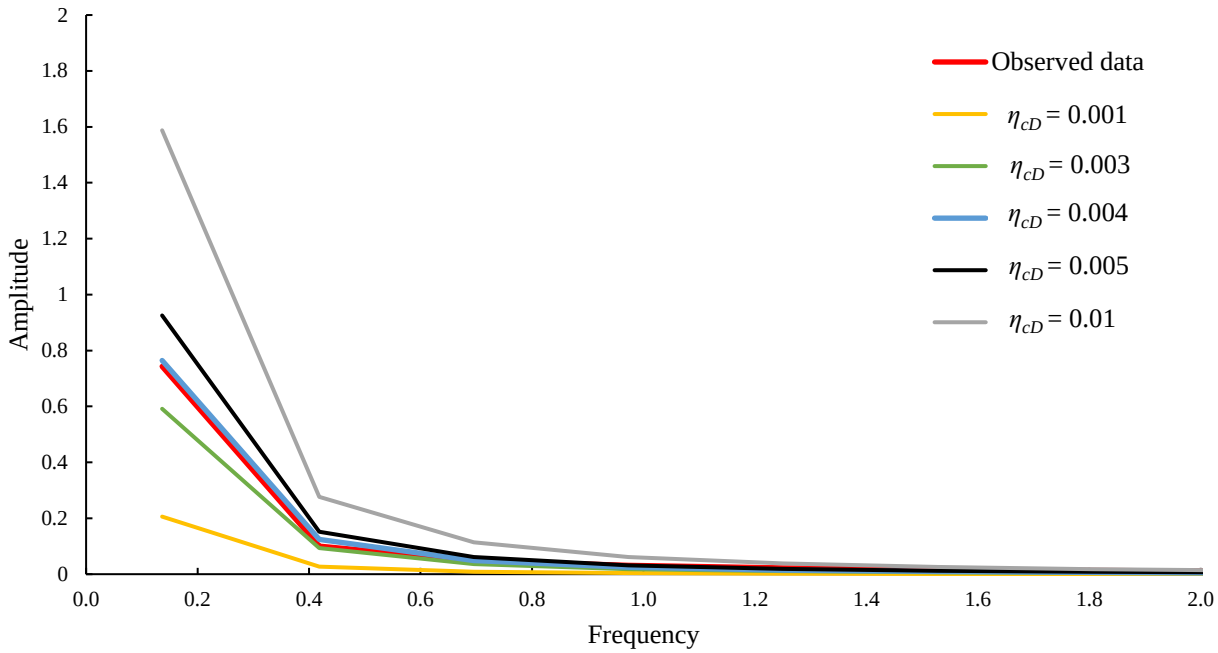

Fig. 4.4. Estimation of caprock diffusivity using the amplitude of above zone pressure response

The other properties of the system may not be known with certainty for the caprock characterization. We assess the effect of uncertainty in other parameters in estimation of caprock diffusivity ratio. In the example problem, the above zone diffusivity ratio (η_{aD}) is 0.2. We use η_{aD} with 50 percent error in analytical solution for caprock characterization. Fig. 4.5 shows the analytical pressure amplitude for η_{aD}=0.1and 0.3 resulting in estimated η_{cD}=0.0023 and 0.00495 respectively.

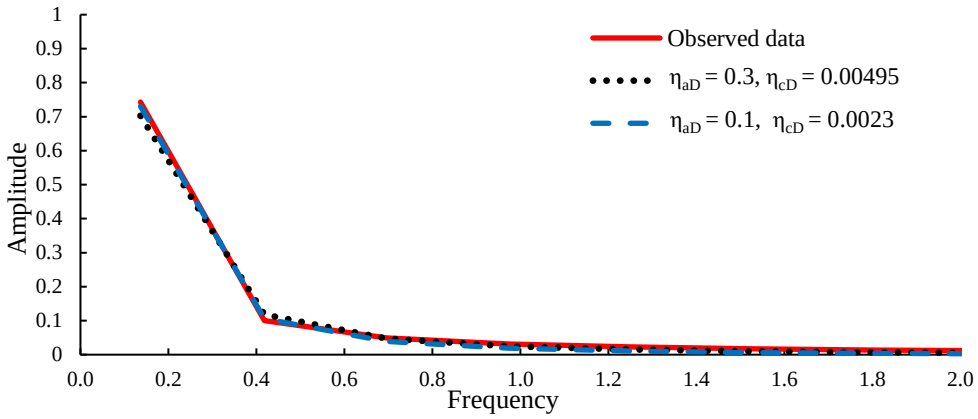

Fig. 4.5. Effect of 50% error in the above zone diffusivity ratio on estimating the caprock diffusivity ratio

Uncertainty in location of well perforations with respect to the caprock can effect the estimated η_{cD}. In the example problem z_{wD} is equal to 0.5. Fig. 4.6 shows the estimated η_{cD} considering 50% error in z_{wD}. For z_{wD}=0.25 and 0.75, the estimated η_{cD} is 0.0055 and 0.0022 respectively. These estimations show that uncertainty in η_{aD} and z_{wD} may lead to significant error in estimated η_{cD}.

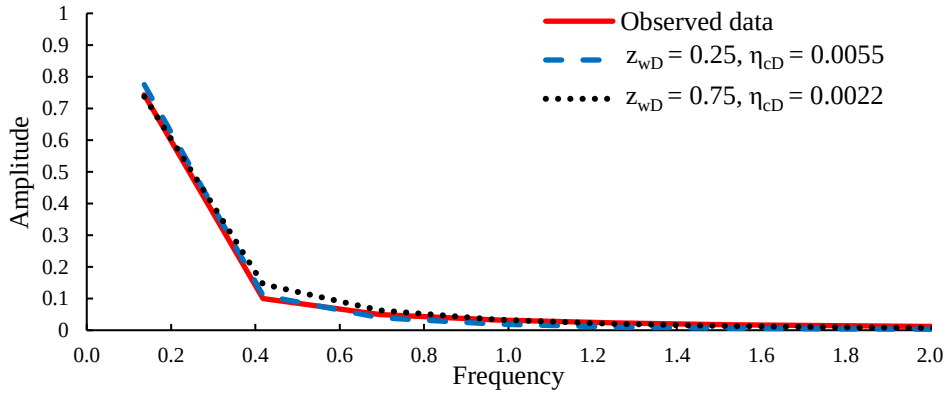

Fig. 4.6. Effect of 50% error in z_w on estimating the caprock diffusivity ratio

4.5. Optimal duty cycle to maximize value of information in periodic test

We propose an approach to increase the value of information gained from the pressure response during the harmonic pressure testing. Optimizing the pick to pick difference of the periodic pressure response can reduce reservoir disturbance during the periodic pressure test.

$$\frac{\partial p_D(x_D,t_D)}{\partial t_D}-\frac{\partial^2 p_D(x_D,t_D)}{\partial {x_D}^2}=q(t_D) \tag{4.27}$$

Green function $G(x_D, t_D)$ is the impulse response of the differential equation.

$$p_D(x_D,t_D)=G(x_D,t_D)\ *\ q(t_D) \tag{4.28}$$

$$\left(\frac{\partial}{\partial t_D}-\frac{\partial^2}{\partial {x_D}^2}\right)G(x_D,t_D)=\delta(x_D)e^{j\omega t_D} \tag{4.29}$$

$$G(x_D,t_D)=\bar{G}(x_D)e^{j\omega t_D} \tag{4.30}$$

$$\left(j\omega-\frac{\partial^2}{\partial {x_D}^2}\right)\bar{G}(x_D)=\delta(x_D) \tag{4.31}$$

Boundary conditions:

$$\begin{aligned} &p(t,0)=p_i \\ &p(t,x,+\infty)=p_i \end{aligned} \tag{4.32}$$

$$\left(\frac{\partial}{\partial t_D}-\frac{\partial^2}{\partial {x_D}^2}\right)G(x_D,t_D)=\delta(x_D)q(t_D) \tag{4.33}$$

$$q(t_D)=\sum_{-\infty}^{\infty}q_m e^{jm\omega_0 t_D} \tag{4.34}$$

$$\omega_0=\frac{2\pi}{T} \tag{4.35}$$

T: Period

τ: Injection/production duration

$D = \frac{\tau}{T}$: Duty cycle

We provide the solution in Fourier series form.

$$p_D\left(x_D, t_D\right) = \sum_{-\infty}^{\infty} u_m\left(x_D\right) e^{jm\omega_0 t_D} \tag{4.36}$$

$$u_m = q_m \bar{G}\left(x_D, t_D\right) \tag{4.37}$$

$$q_m = \frac{1}{T} \int_{-\frac{\tau}{2}}^{\frac{\tau}{2}} q\left(t_D\right) e^{-jm\omega_0 t_D} \tag{4.38}$$

Therefore:

$$q_m = D \ \mathrm{Sinc}\left(mD\right) \tag{4.39}$$

where: $\mathrm{Sinc}\left(x\right) = \frac{\mathrm{Sin}\left(\pi x\right)}{\pi x}$

$$q\left(t_D\right) = D + \sum_{m=1}^{\infty} 2D \ \mathrm{Sinc}\left(mD\right) \mathrm{Cos}\left(m\omega_0 t_D\right) \tag{4.40}$$

In order to calculate the pick to pick ripple (*PPR*), we consider the cumulative effect of the first and second harmonics.

$$p_D\left(x_D, t_D\right) = u_0\left(x\right) + u_1\left(x\right) e^{j\omega_0 t_D} + u_{-1}\left(x\right) e^{-j\omega_0 t_D} + u_2\left(x\right) e^{2j\omega_0 t_D} + u_{-2}\left(x\right) e^{-2j\omega_0 t_D} \tag{4.41}$$

$$p_D\left(x_D, t_D\right) = u_0\left(x\right) + 2\left\{u_1\left(x\right) e^{j\omega_0 t_D} + u_2\left(x\right) e^{2j\omega_0 t_D}\right\} \tag{4.42}$$

$$z = u_1\left(x\right) e^{j\omega_0 t_D} + u_2\left(x\right) e^{2j\omega_0 t_D} \tag{4.43}$$

z is a complex number and ϕ_z is the phase angle of z. Therefore:

$$p_D\left(x_D, t_D\right) = u_0\left(x\right) + 2\left|z\right| \mathrm{Cos}\left(\phi_z\right) \tag{4.44}$$

Therefore, pick to pick ripple of the pressure response is equal to $2|z|$.

$$PPR = 2\left|u_1 e^{j\omega_0 t_D} + u_2 e^{2j\omega_0 t_D}\right| = 2\sqrt{\left|u_1\right|^2 + \left|u_2\right|^2 + 2u_1 u_2^* \mathrm{Cos}\left(\omega_0 t_D\right)} \tag{4.45}$$

$$u_1 = q_1 \bar{G}\left(x_D, \omega_0\right) = 2D\ \mathrm{Sinc}(D)\left(x_D, \omega_0\right) \tag{4.46}$$

$$u_2 = q_2 \bar{G}\left(x_D, \omega_0\right) = 2D\ \mathrm{Sinc}(2D)\left(x_D, 2\omega_0\right) \tag{4.47}$$

$$u_1 = 2D\ \mathrm{Sinc}(D)\frac{1}{\left|\alpha\left(\omega_0\right)\right|} e^{-\alpha(\omega_0)|x|} \tag{4.48}$$

$$u_2 = 2D\ \mathrm{Sinc}(2D)\frac{1}{\left|\alpha\left(2\omega_0\right)\right|} e^{-\alpha(2\omega_0)|x|} \tag{4.49}$$

In order to optimize *PPR*, we neglect the term $\mathrm{Cos}\left(\omega_0 t_D\right)$.

$$PPR = \sqrt{\left|u_1^{\,2}\right| + \left|u_2^{\,2}\right|} \tag{4.50}$$

$$PPR = 2D\sqrt{\frac{\left(\mathrm{Sinc}(D)\right)^2}{\left|\omega_0\right|} e^{-2|\omega_0 x|} + \frac{\left(\mathrm{Sinc}(2D)\right)^2}{2\left|\omega_0\right|} e^{-4|\omega_0 x|}}$$

$$\frac{\partial PPR}{\partial D} = 0 \tag{4.51}$$

Optimum Duty cycle can be calculated by solving equation 4.54.

PPR=0.5

4.6. Summary

In this chapter, we applied pressure pulse testing method for characterization of low permeability caprock. We derive an analytical solution for diffuse caprock leakage from an injection zone to the above zone. The analytical solution is based on the harmonic testing method in which the injection flow rate is a periodic rate. The solution can be modified to model any rate change over a given pulse. The analytical solution is verified with numerical simulation results. The analytical solution is derived in frequency domain. In order to compare the above zone pressure with analytical solution, we use discrete Fourier transform to transform the pressure

response to frequency domain. In an example problem, we estimated the diffusivity of the caprock using the analytical model.

CHAPTER 5. CONCLUSIONS AND RECOMMENDATIONS

5.1. Conclusions

In this study, we proposed pressure interpretation methods to identify the undesirable leakage from the underground storage layers to shallower formations. In chapter 2, we proposed an analytical approach to identify leaky well from fault or caprock leakage. The identification method is based on the normalization of the above zone pressure response against the unknown leakage rate. Applying the above zone pressure, we can identify leaky well, fault, and caprock based on the specific flow regimes. The flow regime of each leaky pathway can be detected in the above zone, because the leakage pressure signals in that zone are not combined with other signals. However, in the injection zone, the leakage signals are combined with the strong injection signals. Results show that the leaky fault causes linear flow with one-half slope line. The one-half slope line would occur if the along-fault conductivity (α_y) is sufficiently high. The derivative slope would be between zero and one-half for smaller values of α_y. The consequent derivative curve for diffuse leakage shows spherical stabilization (-3/2 slope derivative line) while that for focused well leakage shows radial flow characterized by zero-slope derivative. The spherical stabilization may not be fully established because the pressure pulse reaches to the top boundary before reaching to the farther observation point. In such a case, the derivative slope line would show a negative slope lower than 3/2 in magnitude. The identification and characterization procedures in this study are fast and straightforward without the need for optimization procedures that can be computationally expensive. The linear flow of the fault leakage can only be detected at early time and will convert to radial at late time. Therefore, the fault leakage linear flow cannot be seen from a far observation point. We proposed a method to increase the radius of investigation of pressure signals from a linear source. We showed that the quadratic pressure variations can significantly increase the

radius of investigation from a linear source. This fact reduces the arrival time for identification of the linear source.

In chapter 3, we proposed analytical approaches to characterize fault leakage by interpreting the active well pressure signals. We proposed three fault leakage models: 1-fault leakage to a high permeability zone, 2- anisotropic fault leakage, 3- multilayer fault leakage. In the first model, we used the optimization method in combination with the type curves to identify system properties. The type curves were used to find the initial values of unknown parameters. Applying the optimization method, very accurate values of α_u and α were estimated by modifying the initial values. As α_u increased, the sensitivity of the pressure response to T_D and η_D was reduced. However, for low values of α_u, the well pressure data were considerably sensitive to T_D and η_D. The sensitivity of this range of pressure data on flow capacity and diffusivity ratios (T_D and η_D) is less than that to the fault vertical and lateral conductivities. This work shows that the pressure data prior to reaching the flow resistance of the overlying/underlying zone can be enough to estimate hydraulic characteristics of the leaky fault.

In the second fault model, the effect of vertical conductivity is visible during the middle-time response. Therefore, fault conductivities can be estimated by the early-time, middle-time, and late-time pressure response of the active well. Fault displacement may have a little effect on the estimation of the vertical conductivity of the fault. The value of the vertical conductivity can be verified by another observation point that can be the location of the injection well in the above zone. An example problem is provided for fault leakage characterization for which the estimated parameters are found to be identical to the actual values.

In the third fault model, the along-fault permeability significantly affects the pressure response of the shallower formations. The pressure changes of the injection zone and shallower

zone decrease by increasing the along fault permeability. Therefore, the along-fault flow can reduce risk of fault reactivation that may occur during the injection operation. In production cases, fault leakage provides support from the adjacent formations to reduce the reservoir pressure decline. We conclude that the assumption of anisotropic fluid flow inside the fault zone is crucial for fault leakage evaluation.

In chapter 4, we proposed periodic pressure interpretation method for caprock characterization. The periodic method is necessary for caprock leakage because the spherical flow regime ends and early-time after the pressure signals reach to the top boundary of the system. In this three-dimensional model, the analytical solution is significantly faster than the numerical simulation. To evaluate the above zone response, we must only consider the amplitude at the harmonic frequencies (periodic spikes). Results show that the pressure amplitude curves of the analytical solution is useful to characterize the caprock, because the above zone pressure amplitude is very sensitive on caprock diffusivity. Next, the characterization method is evaluated considering uncertainty in other system properties. Considering significant uncertainty in other system properties, the error in estimated caprock diffusivity ratio is less than the error of the above zone diffusivity ratio or error in the injection well distance from the caprock. In order to enhance the value of the information in a periodic test, we optimized the duty cycle to maximize the pick to pick ripple of the periodic pressure response that shows the 50% optimum duty cycle.

5.2. Recommendations

5.2.1. Well leakage

The leaky well signals are very weak in the injection zone comparing to the signals disseminated from the injection wells. Also, both injection and leakage signals are from similar sources (line source) that lead to similar pressure responses. Therefore, it is difficult to distinguish

leakage signals by the injection zone pressure signals. However, fault act as a plane source that disseminates strong leakage signals comparing to the injection wells. An identification method that can clearly distinguish injection from leaky well signals will considerably reduce the leakage identification costs. Further, identification of leaky wells signals from fault leakage using the injection zone responses is a tougher challenge that will lead to a comprehensive method for leakage characterization. This characterization method requires no observation well in the shallower formations. Moreover, leakage characterization by the injection signals is more preventive than above-zone identification to avoid consequent environmental contamination and/or economic losses. This method can be done with conventional pressure methods. However, periodic testing is more suitable to distinguish weak leakage signals from the injection signals.

5.2.2. Fault leakage

The multilayer leaky fault solutions presented in this dissertation are provided in the Laplace-Fourier domain. A simpler real-time solution is useful to understand the fault leakage system at early time, middle time, and late time considering the time as an explicit parameter. It is important to obtain the variation of leakage rate versus time by a fast real-time solution. A suggestion for simplification is to apply no resistance to flow from the upper layers for the multilayer system considering the actual structure of the fault. If the total transmissivity of the above layers is large enough, the calculated leakage rate would be close to the actual value. In addition, the flow geometries and sequential flow regimes can be explicitly investigated in all layers by a solution in the full space domain.

Fault permeability may not be constant during the injection operation. A sealing fault can be reactivated by reaching the threshold pressure and starts conducting fluid to the adjacent zones. A combination of the multilayer fault model with fault reactivation is useful for early detection of

previously sealing faults that start to conduct fluid. This early detection is helpful to prevent induced seismicity as well as significant fault leakage.

Experimental study is necessary to investigate the applications of anisotropic fault leakage. Sand pack set up is a practical method to design a lab experiment for fault leakage. In a multilayer system, the sequential layers of sands can be isolated by sealing materials. A vertical (or deviated) cut can provide the fault zone that should be filled with appropriate grain sizes to reach the anisotropic fluid flow in the fault zone. Fault core and the damaged zone can be made by fine and coarse grains, respectively. It is not required to cross all layers to provide the active well in the bottom layer. The injection well can be designed by setting specific valves in the bottom layer sand pack connected to a pump. The system of sequential layers should be created in a strong container with high pressure and thick material.

5.2.3. Caprock leakage

The above-zone periodic test for caprock leakage characterization can be developed to characterize other types of leakage pathways. This can be achieved by distinguishing the specific flow regimes. Considering the fact that the spherical flow of the caprock leakage would be eliminated after the early time of leakage, the periodic test is more appropriate to distinguish caprock leakage from other types of leaky pathways. In addition, the periodic flow regime identification can be extended to linear flow and radial flow. Therefore, the sequential flow regimes can be detected during the leakage occurrence to detect other types of leaky pathways. These methods must be more complex than normal flow regime identification methods because the leakage rate is an unknown parameter, which decreases the degree of freedom.

There is a large area of caprock weakness in diffusive leakage cases that faces the injected fluid at the early time of injection. Therefore, multiphase leakage can be important for diffusive

leakage. A two-phase model is required to investigate the effect of native fluid on the pressure signals detected in the above zone. Further, the above zone pressure signals can be interpreted to evaluate the condition and location of the native fluid plume in the above zone.

APPENDIX 1. GEOMETRICAL CALCULATIONS OF LOCATING THE LEAKY WELL

In this section, we show how to locate the leaky well when we know the distances between the observation wells (d) and the leaky well. ρ_1 and ρ_2 can be calculated by the proposed method. The three wells (leaky well and observation wells) form a triangle (see triangle ABC in Fig. 2.2). Three sides of the triangle are ρ_1 and ρ_2 and d. We can find location of the leaky well by finding angles of the triangle based on the relationships between sides and angles in the triangles (see Equation (2.12)). Therefore, we can provide the following system of equations (Equations (A1.1)-(A1.2)) for triangle ABC (Fig. 2.2).

$$|AC|.\sin(\theta_1) = |BC|.\sin(\hat{B}) \tag{A1.1}$$

$$|AC|.\sin(\theta_3) = |AB|.\sin(\hat{B}) \tag{A1.2}$$

where $|AC| = \rho_1$, $|BC| = \rho_2$, and $|AB| = d$. The term sin (θ_3) is identical to sin ($\theta_1 + B$), which should be replaced to solve the system of equations (Equations A1.3–A1.4).

$$|AC|.\sin(\theta_1) = |BC|.\sin(\hat{B}) \tag{A1.3}$$

$$|AC|.\sin(\theta_1 + \hat{B}) = d.\sin(\hat{B}) \tag{A1.4}$$

Angles θ_1 and B can be calculated by the above system of equations. Therefore, we can completely locate the leaky well. Next step is to calculate distance between the injection well and the leaky well. First, we should find the angle β_1. We form the same system of equations for triangle *ABD* (Equations A1.5–A1.6).

$$|AD|.\sin(\hat{A} + \theta_2) = |AB|.\sin(\theta_2) \tag{A1.5}$$

$$|AD|.\sin(\hat{A}) = |BD|.\sin(\theta_2) \tag{A1.6}$$

Angles θ_2 and A can be calculated by the above system of equations. Then, we can find the distance between the injection well and the leaky well (R) by solving the following system of equations (Equations A1.7–A1.8). We have already calculated angles B and θ_2. θ_4 is equal to B-θ_2.

$$|BC|.\sin(\theta_4) = |CD|.\sin(\beta_4) \quad \text{(A1.7)}$$

$$|BD|.\sin(\beta_4) = |BC|.\sin(\beta_4 + \theta_4) \quad \text{(A1.8)}$$

where $|CD| = R$.

APPENDIX 2. MATHEMATICAL SOLUTION OF FAULT LEAKAGE TO THE HIGH-PERMEABILITY ZONE

We present the system of differential equations in dimensionless form for generality and convenience. The system of differential equations of regions l and 2 and the corresponding boundary conditions (Equations 2.1-2.10) are converted to dimensionless form using Equations (1.15)-(1.17).

Region 1:

$$\frac{\partial^2 p_{D1}}{\partial x_D^2}+\frac{\partial^2 p_{D1}}{\partial y_D^2}+\delta(x_D-1)\delta(y_D)=\frac{\partial p_{D1}}{\partial t_D} \tag{A2.1}$$

$$p_{D1}(x_D,y_D,0)=0 \tag{A2.2}$$

$$p_{D1}(x_D,\pm\infty,0)=0 \tag{A2.3}$$

$$P_{D1}(+\infty,y_D,t_D)=0 \tag{A2.4}$$

$$\frac{\partial p_{D1}(0,y_D,t_D)}{\partial x_D}=\alpha(p_{D1}(0,y_D,t_D)-p_{D2}(0,y_D,t_D))+\alpha_u(p_{D1}(0,y_D,t_D)) \tag{A2.5}$$

Region 2:

$$\frac{\partial^2 p_{D2}}{\partial x_D^2}+\frac{\partial^2 p_{D2}}{\partial y_D^2}=\frac{1}{\eta_D}\frac{\partial p_{D2}}{\partial t_D} \tag{A2.6}$$

$$p_{D2}(x_D,y_D,0)=0 \tag{A2.7}$$

$$p_{D2}(x_D,\pm\infty,t_D)=0 \tag{A2.8}$$

$$p_{D2}(-\infty,y_D,t_D)=0 \tag{A2.9}$$

$$T_D\frac{\partial p_{D2}(0,y,t)}{\partial x_D}+\alpha_u(p_{D2}(0,y,t))=\alpha(p_{D1}(0,y,t)-p_{D2}(0,y,t)) \tag{A2.10}$$

To solve the system of differential equations, the method of Laplace and Fourier transforms is used. Applying the transforms, the system of partial differential equations in time-space domain

is converted into a system of ordinary differential equations in Laplace-Fourier domain that can be solved. Then, the solutions should be converted back to the time domain using Laplace-Fourier inverse transforms. The Laplace transform of the function P_D is defined as below:

$$\overline{p_D}(x_D, y_D, s) = \mathcal{L}[p_D(x_D, y_D, t_D)] = \int_0^{\infty} p_D(x_D, y_D, t_D) e^{-st} dt \tag{A2.11}$$

where s is the Laplace transform variable. First, the Laplace transform is applied into the time domain.

Region 1:

$$\frac{\partial^2 \overline{p}_{D1}}{\partial x_D^2} + \frac{\partial^2 \overline{p}_{D1}}{\partial y_D^2} + \frac{1}{s}\delta(x_D - 1)\delta(y_D) = s\overline{p}_{D1} \tag{A2.12}$$

$$\overline{p}_{D1}(x_D, \pm\infty, s) = 0 \tag{A2.13}$$

$$\overline{p}_{D1}(+\infty, y_D, s) = 0 \tag{A2.14}$$

$$\frac{\partial \overline{p}_{D1}(0, y_D, s)}{\partial x_D} = \alpha(\overline{p}_{D1}(0, y_D, s) - \overline{p}_{D2}(0, y_D, s)) + \alpha_u(\overline{p}_{D1}(0, y_D, s)) \tag{A2.15}$$

Region 2:

$$\frac{\partial^2 \overline{p}_{D2}}{\partial x_D^2} + \frac{\partial^2 \overline{p}_{D2}}{\partial y_D^2} = \frac{s}{\eta_D}\overline{p}_{D2} \tag{A2.16}$$

$$\overline{p}_{D2}(x_D, \pm\infty, s) = 0 \tag{A2.17}$$

$$\overline{p}_{D2}(-\infty, y_D, s) = 0 \tag{A2.18}$$

$$T_D \frac{\partial \overline{p}_{D2}(0, y_D, s)}{\partial x_D} + \alpha_u(\overline{p}_{D2}(0, y_D, s)) = \alpha(\overline{p}_{D1}(0, y_D, s) - \overline{p}_{D2}(0, y_D, s)) \tag{A2.19}$$

The Fourier transform of function $\overline{p}_D$ is defined as below:

$$\overline{\overline{p}}_D(x_D, \omega, s) = \mathcal{F}[\overline{p}_D(x_D, y_D, s)] = \int_{-\infty}^{+\infty} \overline{p}_D(x_D, y_D, s) e^{i.\omega.t} dt \tag{A2.20}$$

where ω is the Fourier parameter. Second, the Fourier transform is applied into the space domain (y_D) and the ordinary system of differential equations and corresponding boundary conditions in the Laplace-Fourier domain is obtained:

Region 1:

$$\frac{d^2\bar{\bar{p}}_{D1}}{dx_D^2} - A_1^2\bar{\bar{p}}_{D1} = -\frac{1}{s}\delta(x_D - 1) \tag{A2.21}$$

$$\bar{\bar{p}}_{D1}(+\infty) = 0 \tag{A2.22}$$

$$\frac{\partial\bar{\bar{p}}_{D1}(0)}{\partial x_D} = \alpha(\bar{\bar{p}}_{D1}(0) - \bar{\bar{p}}_{D2}(0)) + \alpha_u(\bar{\bar{p}}_{D1}(0)) \tag{A2.23}$$

Region 2:

$$\frac{d^2\bar{\bar{p}}_{D2}}{dx_D^2} - A_2^2\bar{\bar{p}}_{D2} = 0 \tag{A2.24}$$

$$\bar{\bar{p}}_{D2}(-\infty) = 0 \tag{A2.25}$$

$$T_D\frac{\partial\bar{\bar{p}}_{D2}(0)}{\partial x_D} + \alpha_u(\bar{\bar{p}}_{D2}(0)) = \alpha(\bar{\bar{p}}_{D1}(0) - \bar{\bar{p}}_{D2}(0)) \tag{A2.26}$$

where $A_1=\omega^2+s$ and $A_2=\omega^2+s/\eta_D$. The solution in Laplace-Fourier domain is as below.

Region 1:

$$\bar{\bar{p}}_{D1} = \frac{1}{2sA}\left(e^{-|x_D-1|A}\right) + C_1e^{-Ax_D} \tag{A2.27}$$

$$C_0A_1 - C_1A_1 = \alpha(C_0 + C_1 - C_2) + \alpha_u(C_0 + C_1) \tag{A2.28}$$

Region 2:

$$\bar{\bar{p}}_{D2} = C_2e^{A_2x_D} \tag{A2.29}$$

$$T_DC_2A_2 + C_2\alpha_u = \alpha(C_0 + C_1 - C_2) \tag{A2.30}$$

where $C_0 = (1/(2sA_1))e^{-A_1}$. C_1 and C_2 are unknown constants, which must be calculated by combining the equations (A2.28) and (A2.30). The solutions for dimensionless pressure of regions 1 and 2 in Laplace-Fourier domain are:

$$\bar{\bar{p}}_{D1} = \frac{1}{2sA_1}\left(e^{-A_1|x_D-1|} + \frac{A_1\alpha + A_1\alpha_u - 2\alpha\alpha_u - \alpha_u{}^2 + A_1A_2T_D - A_2T_D\alpha - A_2T_D\alpha_u}{A_1\alpha + A_1\alpha_u + 2\alpha\alpha_u + \alpha_u{}^2 + A_1A_2T_D + A_2T_D\alpha + A_2T_D\alpha_u} e^{-A_1(1+x_D)} \right) \quad \text{(A2.31)}$$

$$\bar{\bar{p}}_{D2} = \frac{\alpha}{s} \times \left(\frac{1}{A_1\alpha + A_1\alpha_u + 2\alpha\alpha_u + \alpha_u{}^2 + A_1A_2T_D + A_2T_D\alpha + A_2T_D\alpha_u} e^{(-A_1+A_2x_D)} \right) \quad \text{(A2.32)}$$

APPENDIX 3. ANALYTICAL SOLUTION OF ANISOTROPIC FAULT LEAKAGE

In this section, we show the details of the analytical solution. We converted the system of partial differential equations into the dimensionless form. The dimensionless groups are defined by Equation (16). Equations (A3.1)-(A3.8) shows the system of differential equations for injection zone, above zone, and fault zone in dimensionless form. Injection zone and above zone:

$$\frac{\partial^2 p_{D1}}{\partial {x_D}^2}+\frac{\partial^2 p_{D1}}{\partial {y_D}^2}+\delta(x_D-1)\delta(y_D)=\frac{\partial p_{D1}}{\partial t_D} \tag{A3.1}$$

$$\frac{\partial^2 p_{D2}}{\partial {x_D}^2}+\frac{\partial^2 p_{D2}}{\partial {y_D}^2}=\frac{1}{\eta_{D2}}\frac{\partial p_{D2}}{\partial t_D} \tag{A3.2}$$

$$\frac{\partial^2 p_{Da1}}{\partial {x_D}^2}+\frac{\partial^2 p_{Da1}}{\partial {y_D}^2}=\frac{1}{\eta_{Da1}}\frac{\partial p_{Da1}}{\partial t_D} \tag{A3.3}$$

$$\frac{\partial^2 p_{Da2}}{\partial {x_D}^2}+\frac{\partial^2 p_{Da2}}{\partial {y_D}^2}=\frac{1}{\eta_{Da2}}\frac{\partial p_{Da2}}{\partial t_D} \tag{A3.4}$$

Fault zone:

$$\frac{\partial^2 p_{Df1}}{\partial {y_D}^2}+\frac{1}{\alpha_y}\frac{\partial p_{D1}(t_D,0,y_D)}{\partial x_D}-\frac{\alpha_x}{2\alpha_y}(p_{Df1}-p_{Df2})-\alpha_z(p_{Df1}-p_{Dfa1})=\frac{1}{\eta_{Df}}\frac{\partial p_{fD1}}{\partial t_D} \tag{A3.5}$$

$$\frac{\partial^2 p_{Df2}}{\partial y^2}-\frac{1}{\alpha_y}\frac{\partial p_{D2}(t_D,0,y_D)}{\partial x_D}+\frac{\alpha_x}{2\alpha_y}(p_{Df1}-p_{Df2})-\frac{\alpha_z}{{L_D}^2}(p_{Df2}-p_{Dfa2})=\frac{1}{\eta_{Df}}\frac{\partial p_{Df2}}{\partial t} \tag{A3.6}$$

$$\frac{\partial^2 p_{Dfa1}}{\partial {y_D}^2}-\frac{1}{\alpha_y}\frac{-\partial p_{Da1}(t_D,0,y_D)}{\partial x_D}-\frac{\alpha_x}{2\alpha_y}(p_{Dfa1}-p_{Dfa2})+\alpha_z(p_{Df1}-p_{Dfa1})=\frac{1}{\eta_{Df}}\frac{\partial p_{Dfa1}}{\partial t_D} \tag{A3.7}$$

$$\frac{\partial^2 p_{Dfa2}}{\partial y^2}-\frac{1}{\alpha_y}\frac{\partial p_{Da2}(t_D,0,y_D)}{\partial x}+\frac{\alpha_x}{2\alpha_y}(p_{Dfa1}-p_{Dfa2})+\frac{\alpha_z}{{L_D}^2}(p_{Df2}-p_{Dfa2})=\frac{1}{\eta_{Df}}\frac{\partial p_{Dfa2}}{\partial t_D} \tag{A3.8}$$

Next, the initial and boundary conditions are converted to the dimensionless form.

Initial condition:

$$p_{D1}(x_D, y_D, 0) = p_{D2}(x_D, y_D, 0) = p_{Da1}(x_D, y_D, 0) = p_{Da2}(x_D, y_D, 0) = p_{Df1}(0, y_D)$$
$$= p_{Df2}(0, y_D) = p_{Dfa1}(0, y_D) = p_{Dfa2}(0, y_D) = 0 \quad \text{(A3.9)}$$

Boundary conditions:

$$p_{D1}(t_D, x_D \to \infty, y_D) = p_{D2}(t_D, x_D \to \infty, y_D) = p_{Da1}(t_D, x_D \to \infty, y_D) = p_{Da2}(t_D, x_D \to \infty, y_D) \quad \text{(A3.10)}$$
$$= p_{Df1}(t_D, y_D \to \pm\infty) = p_{Df2}(t_D, y_D \to \pm\infty) = p_{Dfa1}(t_D, y_D \to \pm\infty) = p_{Dfa2}(t_D, y_D \to \pm\infty) = 0$$

$$\frac{\partial p_{D1}(t_D, 0, y_D)}{\partial x_D} = \frac{4}{w_{fD}}\left(p_{D1}(t_D, 0, y_D) - p_{fD1}(t_D, y_D)\right) \quad \text{(A3.11)}$$

$$\frac{\partial p_2(t_D, 0, y_D)}{\partial x_D} = \frac{4}{w_{fD}}\left(p_{Df2}(t_D, y_D) - p_{D2}(t_D, 0, y_D)\right) \quad \text{(A3.12)}$$

$$-\frac{\partial p_{Da1}(t_D, 0, y_D)}{\partial x_D} = \frac{4}{w_{fD}}\left(p_{Dfa1}(t_D, y_D) - p_{Da1}(t_D, 0, y_D)\right) \quad \text{(A3.13)}$$

$$\frac{\partial p_{Da2}(t_D, 0, y_D)}{\partial x_D} = \frac{4}{w_{fD}}\left(p_{Dfa2}(t_D, y_D) - p_{Da2}(t_D, 0, y_D)\right) \quad \text{(A3.14)}$$

In order to convert the system of partial differential equations into a system of ordinary differential equations, we apply Laplace ($\mathcal{L}$) and Fourier ($\mathcal{F}$) transforms on time and y-direction variables (Equations (A3.15)-(A3.16)).

$$\overline{\Delta p}(x, y, s) = \mathcal{L}\left[\Delta p(x, y, t)\right] = \int_0^\infty \Delta p(x, y, t) e^{-st} dt \quad \text{(A3.15)}$$

$$\overline{\overline{\Delta p}}(x, \omega, s) = \mathcal{F}\left[\overline{\Delta p}(x, y, s)\right] = \int_{-\infty}^{+\infty} \overline{\Delta p}(x, y, s) e^{i\omega y} dy \quad \text{(A3.16)}$$

where ω and s are Fourier and Laplace Variables. The system of ordinary differential equations in the Laplace-Fourier domain is shown below.

$$\frac{\partial^2 \overline{\overline{p}}_{D1}}{\partial x_D^{\,2}} - A^2 \overline{\overline{p}}_{D1} + \frac{1}{s}\delta(x_D - 1) = 0 \quad \text{(A3.17)}$$

$$\frac{\partial^2 \overline{\overline{p}}_{D2}}{\partial x_D^{\,2}} - A_2^{\,2} \overline{\overline{p}}_{D2} = 0 \quad \text{(A3.18)}$$

$$\frac{\partial^2 \bar{\bar{p}}_{Da1}}{\partial x_D^{\,2}} - A_{a1}{}^2 \bar{\bar{p}}_{Da1} = 0 \tag{A3.19}$$

$$\frac{\partial^2 \bar{\bar{p}}_{Da2}}{\partial x_D^{\,2}} - A_{a2}{}^2 \bar{\bar{p}}_{Da2} = 0 \tag{A3.20}$$

Next, we convert Equations (5)-(8) to dimensionless form:

$$-A_f{}^2 \bar{\bar{p}}_{Df1}(s,\omega) + \frac{1}{\alpha_y}\frac{\partial \bar{\bar{p}}_{D1}(s,0,\omega)}{\partial x_D} - \frac{\alpha_x}{2\alpha_y}(\bar{\bar{p}}_{Df1} - \bar{\bar{p}}_{Df2}) - \alpha_z(\bar{\bar{p}}_{Df1} - \bar{\bar{p}}_{Dfa1}) = 0 \tag{A3.21}$$

$$-A_f{}^2 \bar{\bar{p}}_{Df2}(s,\omega) - \frac{1}{\alpha_y}\frac{\partial \bar{\bar{p}}_{D2}(s,0,\omega)}{\partial x_D} + \frac{\alpha_x}{2\alpha_y}(\bar{\bar{p}}_{Df1} - \bar{\bar{p}}_{Df2}) - \frac{\alpha_z}{L_D^{\,2}}(\bar{\bar{p}}_{Df2} - \bar{\bar{p}}_{Dfa2}) = 0 \tag{A3.22}$$

$$-A_f{}^2 \bar{\bar{p}}_{Dfa1}(s,\omega) - \frac{1}{\alpha_y}\frac{-\partial \bar{\bar{p}}_{Da1}(s,0,\omega)}{\partial x_D} - \frac{\alpha_x}{2\alpha_y}(\bar{\bar{p}}_{Dfa1} - \bar{\bar{p}}_{Dfa2}) + \alpha_z(\bar{\bar{p}}_{Df1} - \bar{\bar{p}}_{Dfa1}) = 0 \tag{A3.23}$$

$$-A_f{}^2 \bar{\bar{p}}_{Dfa2}(s,\omega) - \frac{1}{\alpha_y}\frac{\partial \bar{\bar{p}}_{Da2}(s,0,\omega)}{\partial x_D} + \frac{\alpha_x}{2\alpha_y}(\bar{\bar{p}}_{Dfa1} - \bar{\bar{p}}_{Dfa2}) + \frac{\alpha_z}{L_D^{\,2}}(\bar{\bar{p}}_{Df2} - \bar{\bar{p}}_{Dfa2}) = 0 \tag{A3.24}$$

Boundary conditions in Laplace-Fourier domain:

$$\begin{aligned}&\bar{\bar{p}}_{D1}(x_D \to \infty, y_D, t_D) = \bar{\bar{p}}_{D2}(x_D \to -\infty, y_D, t_D) = \bar{\bar{p}}_{Da1}(x_D \to \infty, y_D, t_D) \\ &= \bar{\bar{p}}_{Da2}(x_D \to -\infty, y_D, t_D) = 0\end{aligned} \tag{A3.25}$$

$$\frac{\partial \bar{\bar{p}}_{D1}(t_D, 0, y_D)}{\partial x_D} = \alpha_x\left(\bar{\bar{p}}_{D1}(s,0,\omega) - \bar{\bar{p}}_{Df1}(s,\omega)\right) \tag{A3.26}$$

$$\frac{\partial \bar{\bar{p}}_{D2}(s,0,\omega)}{\partial x_D} = \alpha_x \frac{h_{D2}}{T_{D2}}\left(\bar{\bar{p}}_{Df2}(s,\omega) - \bar{\bar{p}}_{D2}(s,0,\omega)\right) \tag{A3.27}$$

$$-\frac{\partial \bar{\bar{p}}_{Da1}(s,0,\omega)}{\partial x_D} = \alpha_x \frac{h_{Da1}}{T_{Da1}}\left(\bar{\bar{p}}_{Dfa1}(s,\omega) - \bar{\bar{p}}_{Da1}(s,0,\omega)\right) \tag{A3.28}$$

$$\frac{\partial \bar{\bar{p}}_{Da2}(s,0,\omega)}{\partial x_D} = \alpha_x \frac{h_{Da2}}{T_{Da2}}\left(\bar{\bar{p}}_{Dfa2}(s,\omega) - \bar{\bar{p}}_{Da2}(s,0,\omega)\right) \tag{A3.29}$$

Next, we derive the solution in the Laplace-Fourier domain:

$$\bar{\bar{p}}_{D1} = \frac{1}{2sA}\left(e^{-|x_D-1|A}\right) + C_1 e^{-Ax_D} \tag{A3.30}$$

$$\bar{\bar{p}}_{D2} = C_2 e^{A_2 x_D} \tag{A3.31}$$

$$\bar{\bar{p}}_{Da1} = C_3 e^{-A_{a1} x_D} \tag{A3.32}$$

$$\bar{\bar{p}}_{Da2} = C_4 e^{A_{a2} x_D} \tag{A3.33}$$

Combining Equations (A3.21)-(A3.24) with the boundary conditions (Equations A3.25-A3.29), the coefficients C_1-C_4 are calculated by the system of linear equations shown in Equation (3.53).

REFERENCES

Agosta, F., Prasad, M., & Aydin, A. (2007). Physical properties of carbonate fault rocks, fucino basin (Central Italy): implications for fault seal in platform carbonates. *Geofluids, 7*(1), 19-32.

Ambastha, A. K., McLeroy, P. G., & Grader, A. S. (1989). Effects of a partially communicating fault in a composite reservoir on transient pressure testing. *SPE Formation Evaluation, 4*(02), 210-218. doi:10.2118/16764-PA

Anderson, E. I. (2006). Analytical solutions for flow to a well through a fault. *Advances in Water Resources, 29*(12), 1790-1803. doi:https://doi.org/10.1016/j.advwatres.2005.12.010

Annunziatellis, A., Beaubien, S., Bigi, S., Ciotoli, G., Coltella, M., & Lombardi, S. (2008). Gas migration along fault systems and through the vadose zone in the Latera caldera (central Italy): Implications for CO2 geological storage. *International Journal of Greenhouse Gas Control, 2*(3), 353-372.

Avci, C. B. (1994). Evaluation of flow leakage through abandoned wells and boreholes. *Water Resources Research, 30*(9), 2565-2578.

Bachu, S., & Bennion, D. B. (2009). Experimental assessment of brine and/or CO 2 leakage through well cements at reservoir conditions. *International Journal of Greenhouse Gas Control, 3*(4), 494-501.

Barton, C. A., Zoback, M. D., & Moos, D. (1995). Fluid flow along potentially active faults in crystalline rock. *Geology, 23*(8), 683-686.

Bense, V. F., & Person, M. A. (2006). Faults as conduit-barrier systems to fluid flow in siliciclastic sedimentary aquifers. *Water Resources Research, 42*(5). doi:https://doi.org/10.1029/2005WR004480

Benson, S. M., & Orr, F. M. (2008). Carbon dioxide capture and storage. *Mrs Bulletin, 33*(4), 303-305.

Billi, A., Salvini, F., & Storti, F. (2003). The damage zone-fault core transition in carbonate rocks: implications for fault growth, structure and permeability. *Journal of Structural Geology, 25*(11), 1779-1794. doi:https://doi.org/10.1016/S0191-8141(03)00037-3

Birkholzer, J. T., Zhou, Q., & Tsang, C.-F. (2009a). Large-scale impact of CO2 storage in deep saline aquifers: A sensitivity study on pressure response in stratified systems. *International Journal of Greenhouse Gas Control, 3*(2), 181-194.

Birkholzer, J. T., Zhou, Q., & Tsang, C.-F. (2009b). Large-scale impact of CO 2 storage in deep saline aquifers: a sensitivity study on pressure response in stratified systems. *International Journal of*

Greenhouse Gas Control, *3*(2), 181-194.

Bixel, H. C., Larkin, B. K., & Vanpoollen, H. K. (1963). Effect of Linear Discontinuities on Pressure Build-up and Drawdown Behavior. *Transactions of the Society of Petroleum Engineers of Aime*, *228*(8), 885-895. doi:10.2118/611-PA

Blackford, J., Jones, N., Proctor, R., Holt, J., Widdicombe, S., Lowe, D., & Rees, A. (2009). An initial assessment of the potential environmental impact of CO2 escape from marine carbon capture and storage systems. *Proceedings of the Institution of Mechanical Engineers, Part A: Journal of Power and Energy*, *223*(3), 269-280.

Bruhn, R. L., Parry, W. T., Yonkee, W. A., & Thompson, T. (1994). Fracturing and hydrothermal alteration in normal fault zones. *Pure and applied geophysics*, *142*(3-4), 609-644.

Caine, J. S., Evans, J. P., & Forster, C. B. (1996). Fault zone architecture and permeability structure. *Geology*, *24*(11), 1025-1028. doi:https://doi.org/10.1130/0091-7613(1996)024%3C1025:FZAAPS%3E2.3.CO;2

Caine, J. S., & Forster, C. B. (1999). Fault zone architecture and fluid flow: Insights from field data and numerical modeling. *Faults and subsurface fluid flow in the shallow crust*, 101-127.

Cappa, F., & Rutqvist, J. (2011). Modeling of coupled deformation and permeability evolution during fault reactivation induced by deep underground injection of CO 2. *International Journal of Greenhouse Gas Control*, *5*(2), 336-346.

Chabora, E. R., & Benson, S. M. (2009). Brine displacement and leakage detection using pressure measurements in aquifers overlying CO2 storage reservoirs. *Energy Procedia*, *1*(1), 2405-2412. doi:https://doi.org/10.1016/j.egypro.2009.01.313

Chen, M., Buscheck, T. A., Wagoner, J. L., Sun, Y., White, J. A., Chiaramonte, L., & Aines, R. D. (2013). Analysis of fault leakage from Leroy underground natural gas storage facility, Wyoming, USA. *Hydrogeology Journal*, *21*(7), 1429-1445.

Cheng, A. D., & Morohunfola, O. (1993). Multilayered leaky aquifer systems: 1. Pumping well solutions. *Water Resources Research*, *29*(8), 2787-2800.

Chester, F. M., Evans, J. P., & Biegel, R. L. (1993). Internal structure and weakening mechanisms of the San Andreas fault. *Journal of Geophysical Research: Solid Earth*, *98*(B1), 771-786.

Cihan, A., Zhou, Q., & Birkholzer, J. T. (2011). Analytical solutions for pressure perturbation and fluid leakage through aquitards and wells in multilayered-aquifer systems. *Water Resources Research*,

47(10).

CMG. (2015). Computer Modelling Group. Calgary, Alberta, Canada.

Damen, K., Faaij, A., & Turkenburg, W. (2006). Health, safety and environmental risks of underground CO 2 storage–overview of mechanisms and current knowledge. *Climatic Change, 74*(1), 289-318.

de Orte, M. R., Sarmiento, A. M., Basallote, M. D., Rodríguez-Romero, A., & Riba, I. (2014). Effects on the mobility of metals from acidification caused by possible CO2 leakage from sub-seabed geological formations. *Science of the Total Environment, 470*, 356-363.

Dejam, M., & Hassanzadeh, H. (2018). Diffusive leakage of brine from aquifers during CO 2 geological storage. *Advances in Water Resources, 111*, 36-57.

Ebigbo, A., Class, H., & Helmig, R. (2007). CO2 leakage through an abandoned well: problem-oriented benchmarks. *Computational Geosciences, 11*(2), 103-115.

Ellsworth, W. L. (2013). Injection-induced earthquakes. *Science, 341*(6142), 1225942.

Evans, J. P., Forster, C. B., & Goddard, J. V. (1997). Permeability of fault-related rocks, and implications for hydraulic structure of fault zones. *Journal of Structural Geology, 19*(11), 1393-1404. doi:https://doi.org/10.1016/S0191-8141(97)00057-6

Fokker, P. A., Borello, E. S., Serazio, C., & Verga, F. (2012). Estimating reservoir heterogeneities from pulse testing. *Journal of Petroleum Science and Engineering, 86*, 15-26.

Fokker, P. A., Borello, E. S., Verga, F., & Viberti, D. (2017). *Harmonic Pulse Testing for Well and Reservoir Characterization.* Paper presented at the SPE Europec featured at 79th EAGE Conference and Exhibition.

Fokker, P. A., & Verga, F. (2011). Application of harmonic pulse testing to water–oil displacement. *Journal of Petroleum Science and Engineering, 79*(3), 125-134.

Harvey, O. R., Qafoku, N. P., Cantrell, K. J., Lee, G., Amonette, J. E., & Brown, C. F. (2012). Geochemical implications of gas leakage associated with geologic CO2 storage, A qualitative review. *Environmental science & technology, 47*(1), 23-36. doi:https://doi.org/10.1021/es3029457

Hermanrud, C., & Bols, H. M. N. (2002). Leakage from overpressured hydrocarbon reservoirs at Haltenbanken and in the northern North Sea. In *Norwegian Petroleum Society Special*

Publications (Vol. 11, pp. 221-231): Elsevier.

Hollaender, F., Hammond, P. S., & Gringarten, A. C. (2002). *Harmonic testing for continuous well and reservoir monitoring.* Paper presented at the SPE Annual Technical Conference and Exhibition.

Huntoon, P., & Lundy, D. A. (1979). Fracture-Controlled Ground-Water Circulation and Well Siting in the Vicinity of Laramie. *Ground Water, 17(5)*(5), 463-469. doi:10.1111/j.1745-6584.1979.tb03342.x

IEAGHG. (2016). Fault permeability. Rep. No. 2016/13. Cheltenham, UK: IEA Greenhouse Gas R&D Programme

Ingram, G. M., & Urai, J. L. (1999). Top-seal leakage through faults and fractures: the role of mudrock properties. *Geological Society, London, Special Publications, 158*(1), 125-135.

IPCC. (2005). Special Report on Carbon Dioxide Capture and Storage: Prepared by Working Group III of the Intergovernmental Panel on Climate Change. *Cambridge University Press*.

Javandel, I., Tsang, C. F., Witherspoon, P. A., & Morganwalp, D. (1988). Hydrologic detection of abandoned wells near proposed injection wells for hazardous waste disposal. *Water Resources Research, 24*(2), 261-270.

Jha, B., & Juanes, R. (2014). Coupled modeling of multiphase flow and fault poromechanics during geologic CO2 storage. *Energy Procedia, 63*, 3313-3329. doi:https://doi.org/10.1016/j.egypro.2014.11.360

Johnson, C. R., Greenkorn, R., & Woods, E. (1966). Pulse-testing: a new method for describing reservoir flow properties between wells. *Journal of Petroleum Technology, 18*(12), 1,599-591,604.

Jordan, P., & Carey, J. W. (2016). Steam blowouts in California Oil and Gas District 4: Comparison of the roles of initial defects versus well aging and implications for well blowouts in geologic carbon storage projects. *International Journal of Greenhouse Gas Control, 51*, 36-47.

Keating, E. H., Hakala, J. A., Viswanathan, H., Carey, J. W., Pawar, R., Guthrie, G. D., & Fessenden-Rahn, J. (2013). CO2 leakage impacts on shallow groundwater: Field-scale reactive-transport simulations informed by observations at a natural analog site. *Applied geochemistry, 30*, 136-147.

Keranen, K. M., Savage, H. M., Abers, G. A., & Cochran, E. S. (2013). Potentially induced earthquakes in Oklahoma, USA: Links between wastewater injection and the 2011 Mw 5.7 earthquake sequence. *Geology, 41*(6), 699-702.

Knabe, R., & Wang, Y. (2011). Permeability characterization on tight gas samples using pore pressure oscillation method. *Petrophysics, 52*(06), 437-443.

Kuo, C. (1972). Determination of reservoir properties from sinusoidal and multirate flow tests in one or more wells. *Society of Petroleum Engineers Journal, 12*(06), 499-507.

Lei, G., Cao, N., McPherson, B. J., Liao, Q., & Chen, W. (2019). A novel Analytical Model for pore Volume compressibility of fractal porous Media. *Scientific reports, 9*(1), 1-11.

Leith, T. L., Kaarstad, I., Connan, J., Pierron, J., & Caillet, G. (1993). Recognition of caprock leakage in the Snorre Field, Norwegian North Sea. *Marine and petroleum geology, 10*(1), 29-41. doi:10.1016/0264-8172(93)90097-C

Lindsay, N., Murphy, F., & Walsh, J. Outcrop studies of shale smears on fault surfaces. *The geological modelling of hydrocarbon reservoirs and outcrop analogues, 15*, 113-123.

Little, M. G., & Jackson, R. B. (2010). Potential impacts of leakage from deep CO2 geosequestration on overlying freshwater aquifers. *Environmental science & technology, 44*(23), 9225-9232.

Lu, J., Partin, J. W., Hovorka, S. D., & Wong, C. (2010). Potential risks to freshwater resources as a result of leakage from CO 2 geological storage: a batch-reaction experiment. *Environmental Earth Sciences, 60*(2), 335-348.

Manzocchi, T., Childs, C., & Walsh, J. (2010). Faults and fault properties in hydrocarbon flow models. *Geofluids, 10*(1-2), 94-113. doi:https://doi.org/10.1111/j.1468-8123.2010.00283.x

Maslia, M. L., & Prowell, D. C. (1990). Effect of Faults on Fluid-Flow and Chloride Contamination in a Carbonate Aquifer System. *Journal of Hydrology, 115*(1-4), 1-49. doi:10.1016/0022-1694(90)90196-5

Matlab. (2015). Matlab (Version 8.6). Natick, Massachusetts, United States: The MathWorks, Inc. Software available at www.mathworks.com.

Matthäi, S. K., Aydin, A., Pollard, D. D., & Stephen, G. R. (1998). Simulation of transient well-test signatures for geologically realistic faults in sandstone reservoirs. *SPE Journal, 3*(01), 62-76. doi:https://doi.org/10.2118/38442-PA

Mbia, E. N., Frykman, P., Nielsen, C. M., Fabricius, I. L., Pickup, G. E., & Bernstone, C. (2014). Caprock compressibility and permeability and the consequences for pressure development in CO2 storage sites. *International Journal of Greenhouse Gas Control, 22*, 139-153.

Mosaheb, M., & Zeidouni, M. (2017a). *Above-Zone Pressure Response to Distinguish Between Fault and Caprock Leakage.* Paper presented at the SPE Western Regional Meeting.

Mosaheb, M., & Zeidouni, M. (2017b). *Pressure Transient Analysis for Leaky Well Characterization and its Identification From Leaky Fault.* Paper presented at the SPE Health, Safety, Security, Environment, & Social Responsibility Conference-North America.

Ochoa-González, G. H., Carreón-Freyre, D., Cerca, M., & López-Martínez, M. (2015). Assessment of groundwater flow in volcanic faulted areas. A study case in Queretaro, Mexico. *Geofísica internacional*, *54*(3), 199-220. doi:https://doi.org/10.1016/j.gi.2015.04.016

Pacala, S. W. (2003). -*Global Constraints on Reservoir Leakage.* Paper presented at the Greenhouse Gas Control Technologies-6th International Conference.

Pruess, K. (2005). Numerical studies of fluid leakage from a geologic disposal reservoir for CO2 show self-limiting feedback between fluid flow and heat transfer. *Geophysical Research Letters, 32*(14).

Raghavan, R. (2010). A composite system with a planar interface. *Journal of Petroleum Science and Engineering, 70(3),* 229-234. doi:10.1016/j.petrol.2009.11.015

Rahman, N. M., Miller, M. D., & Mattar, L. (2003). Analytical solution to the transient-flow problems for a well located near a finite-conductivity fault in composite reservoirs. *In SPE Annual Technical Conference and Exhibition*. doi:https://doi.org/10.2118/84295-MS

Rawling, G. C., Goodwin, L. B., & Wilson, J. L. (2001). Internal architecture, permeability structure, and hydrologic significance of contrasting fault-zone types. *Geology, 29*(1), 43-46.

Renner, J., & Messar, M. (2006). Periodic pumping tests. *Geophysical Journal International, 167*(1), 479-493.

Rosa, A., & Horne, R. (1997). Reservoir description by well test analysis using cyclic flow rate variation. *SPE Formation Evaluation, 12*(04), 247-254.

Rutqvist, J., Birkholzer, J., Cappa, F., & Tsang, C.-F. (2007). Estimating maximum sustainable injection pressure during geological sequestration of CO2 using coupled fluid flow and geomechanical fault-slip analysis. *Energy Conversion and management, 48*(6), 1798-1807.

Scherer, G. W., Celia, M. A., Prevost, J.-H., Bachu, S., Bruant, R., Duguid, A., . . . Vichit-Vadakan, W. (2015). Leakage of CO2 through abandoned wells: Role of corrosion of cement. *In CO2 Capture Project Technical Results*, 827-848.

Scherer, G. W., & Huet, B. (2009). Carbonation of wellbore cement by CO2 diffusion from caprock. *International Journal of Greenhouse Gas Control, 3*(6), 731-735.

Selvadurai, A. (2012). Fluid leakage through fractures in an impervious caprock embedded between two geologic aquifers. *Advances in Water Resources, 41*, 76-83.

Shakiba, M., & Hosseini, S. A. (2016). Detection and characterization of CO 2 leakage by multi-well pulse testing and diffusivity tomography maps. *International Journal of Greenhouse Gas Control, 54*, 15-28.

Shakiba, M., Hosseini, S. A., & Sepehrnoori, K. (2017). *Monitoring and Improvement of Waterflooding Sweep Efficiency Using Pressure Pulse Testing.* Paper presented at the SPE Annual Technical Conference and Exhibition.

Shan, C., Javandel, I., & Witherspoon, P. A. (1995). Characterization of leaky faults: Study of water flow in aquifer-fault-aquifer systems. *Water Resources Research, 31(12)*, 2897-2904. doi:https://doi.org/10.1029/95WR02483

Sibson, R. (1977). Fault rocks and fault mechanisms. *Journal of the Geological Society, 133*(3), 191-213 doi:10.1144/gsjgs.133.3.0191

Sibson, R. H. (2003). Brittle-failure controls on maximum sustainable overpressure in different tectonic regimes. *AAPG bulletin, 87*(6), 901-908.

Siirila, E. R., Navarre-Sitchler, A. K., Maxwell, R. M., & McCray, J. E. (2012). A quantitative methodology to assess the risks to human health from CO2 leakage into groundwater. *Advances in Water Resources, 36*, 146-164.

Stehfest, H. (1970). Algorithm 368: Numerical inversion of Laplace transforms [D5]. *Communications of the ACM, 13*(1), 47-49. doi:10.1145/361953.361969

Stewart, G., & Gupta, A. (1984). *The interpretation of interference tests in a reservoir with sealing and partially communicating faults*. Paper presented at the European Petroleum Conference.

Stoessell, R. K., & Prochaska, L. C. (2005). Chemical evidence for migration of deep formation fluids into shallow aquifers in south Louisiana. *Gulf Coast Association of Geological Sciences Transactions*, 794-808.

Sun, A. Y., Lu, J., & Hovorka, S. (2015). A harmonic pulse testing method for leakage detection in deep subsurface storage formations. *Water Resources Research, 51*(6), 4263-4281.

Sun, A. Y., & Nicot, J.-P. (2012). Inversion of pressure anomaly data for detecting leakage at geologic carbon sequestration sites. *Advances in Water Resources, 44*, 20-29. doi:https://doi.org/10.1016/j.advwatres.2012.04.006

Toews, K. L., Shroll, R. M., Wai, C. M., & Smart, N. G. (1995). pH-defining equilibrium between water and supercritical CO2. Influence on SFE of organics and metal chelates. *Analytical Chemistry, 67*(22), 4040-4043.

Vilarrasa, V., Olivella, S., Carrera, J., & Rutqvist, J. (2014). Long term impacts of cold CO 2 injection on the caprock integrity. *International Journal of Greenhouse Gas Control, 24*, 1-13.

Watson, T. L., & Bachu, S. (2009). Evaluation of the potential for gas and CO2 leakage along wellbores. *SPE Drilling & Completion, 24*(01), 115-126.

Wiese, B., Zimmer, M., Nowak, M., Pellizzari, L., & Pilz, P. (2013). Well-based hydraulic and geochemical monitoring of the above zone of the CO 2 reservoir at Ketzin, Germany. *Environmental Earth Sciences, 70*(8), 3709-3726. doi:https://doi.org/10.1007/s12665-013-2744-x

Winestock, A. G., & Colpitts, G. P. (1965). Advances in Estimating Gas Well Deliverability. *Journal of Canadian Petroleum Technology, 4*(03), 111-119. doi:10.2118/65-03-01

Wiprut, D., & Zoback, M. D. (2000). Fault reactivation and fluid flow along a previously dormant normal fault in the northern North Sea. *Geology, 28*(7), 595-598.

Wojtanowicz, A. (2016). Environmental control of well integrity. In *Environmental Technology in the Oil Industry* (pp. 61-100): Springer.

Yaxley, L. M. (1987). Effect of a partially communicating fault on transient pressure behavior. *SPE Formation Evaluation, 2(04)*, 590-598. doi:10.2118/14311-PA

Yielding, G., Freeman, B., & Needham, D. T. (1997). Quantitative fault seal prediction. *AAPG Bulletin, 81*(6), 897-917.

Zeidouni, M. (2012). Analytical model of leakage through fault to overlying formations. *Water Resources Research, 48*. doi:https://doi.org/10.1029/2012wr012582

Zeidouni, M. (2014). Analytical model of well leakage pressure perturbations in a closed aquifer system. *Advances in Water Resources, 69*, 13-22.

Zeidouni, M. (2016). Semi-Analytical Model of Pressure Perturbations Induced by Fault Leakage in

Multilayer System. *Journal of Hydrologic Engineering, 21*(6). doi:https://doi.org/10.1061/(Asce)He.1943-5584.0001359

Zeidouni, M., & Pooladi-Darvish, M. (2012). Leakage characterization through above-zone pressure monitoring: 1—Inversion approach. *Journal of Petroleum Science and Engineering, 98*, 95-106.

Zeidouni, M., & Vilarrasa, V. (2016). Identification of above-zone pressure perturbations caused by leakage from those induced by deformation. *Environmental Earth Sciences, 75*(18), 1271.

VITA

Mojtaba Mosaheb graduated from NODET (National Organization for Development of Exceptional Talents) high school in Iran. He completed both BSc and MSc in petroleum engineering at Sharif University of Technology in 2012 and Azad University in 2014. He joined Louisiana State University in 2015 to pursue his PhD research on carbon sequestration. He applies both analytical and numerical modeling tools for subsurface leakage characterization.